Computational modelling of defects and charge trapping in amorphous and crystalline metal oxides

Oliver A. Dicks

A dissertation submitted in partial fulfillment
of the requirements for the degree of
Doctor of Engineering
of
University College London.

Department of Chemistry
University College London

February 15, 2018

I, Oliver A. Dicks, confirm that the work presented in this thesis is my own. Where information has been derived from other sources, I confirm that this has been indicated in the work.

Abstract

Thin films of metal oxides, like Al_2O_3 and $LaAlO_3$, play a crucial role in emerging nanoelectronic devices. Using density functional theory (DFT) and other computational methods, the properties of defects and intrinsic polaron trapping have been calculated in $LaAlO_3$ and amorphous Al_2O_3.

The spectroscopic properties of neutral (V_O^0) and charged (V_O^+) oxygen vacancies in cubic and rhombohedral $LaAlO_3$ have been investigated using Time Dependent DFT and the embedded cluster method. The peaks of the optical absorption spectra are predicted at 3.5 and 4.2 eV for V_O^0 and 3.6 eV for V_O^+ in rhombohedral $LaAlO_3$. The calculated electron paramagnetic resonance (EPR) parameters of V_O^+ accurately predict the width (3 mT) and position of its EPR spectrum.

Amorphous Al_2O_3 is then investigated, which has applications in non-volatile memory and a-IGZO (amorphous indium-gallium-zinc oxide) thin film transistors. Amorphous Al_2O_3 structures were generated using a molecular dynamics melt-quench approach and found to be in good agreement with experiment. DFT calculations, using a tuned hybrid functional, determined that the a-Al_2O_3 band gap decreases to 5.5 eV, compared to 8.6 eV in α-Al_2O_3, because of the reduction in Al coordination number in the amorphous phase. This causes a shift in the electrostatic potential that lowers the conduction band minimum, adding support to experimental measurements of band offsets.

Then intrinsic polaron and bipolaron trapping in a-Al_2O_3 is modeled. The average trapping energy of hole polarons in a-Al_2O_3 was calculated to be 1.26 eV, much higher than the 0.38 eV calculated for α-Al_2O_3. Electrons were found not to trap in both crystalline and amorphous Al_2O_3.

To explain the negative charging of Al_2O_3 films the properties of oxygen, hydrogen and aluminium defects were calculated. A mechanism is proposed to explain experimental trap spectroscopy measurements, whereby negatively charge defects are compensated by positively charged defects that have unoccupied states in the band gap.

These predictions will facilitate experimental identification of defect states in $LaAlO_3$ and Al_2O_3 and their effect on nanodevices.

Acknowledgements

I am immensely grateful to all the people who have offered their help, support and friendship during my doctoral training and the writing of this thesis, it would not have been possible without you.

Firstly, to my supervisor Alex Shluger, thank you for your counsel, your guidance and all the time you have spent helping me through my research. I will always remember the first rule of being a theoretical scientist, and I hope to bring the same thoroughness and scientific curiousity to my future work as you do every day. I am also very grateful to Peter Sushko for taking me on as an EngD student and for being my supervisor for the first stage of my doctorate. I would not have had this opportunity without his hard work. Lots of credit also goes to the rest of the Shluger group and others in UCL who provided invaluable discussion, help and friendship. Special thanks go to Jack Strand, Jonathon Cottom, Al-Moatasem El-Sayed, Matthew Watkins, Moloud Kaviani, Sanliang Ling, Rasmus Jakobsen, Thomas Durrant, Julian Gaberle, Matthew Halliday and Samuel Murphy.

Next my thanks go to Peter Littlewood for his help and encouragement, and to Argonne National Laboratory for funding my doctorate and for providing me with access to the blues cluster. I must also thank the Doctoral Training Centre, the Thomas Young Centre and the Materials Chemistry Consortium, who gave me access to the computer resources I needed for this work. I would also like to thank Valeri Afanas'ev for providing experimental data on alumina thin films and for his collaboration in this work.

To my friends and family, thank you for being there to support me, for your understanding, and for getting me here in the first place. To Mum and Dad, thank

you for always encouraging me and being there for me, I love you both very much.

Finally, thank you Claire, I could not have done this without you and your love and belief in me.

List of publications

The following publications are derived form work presented in this thesis:

1. O. A. Dicks, A. L. Shluger, P. V. Sushko and P. B. Littlewood, "Spectroscopic properties of oxygen vacancies in $LaAlO_3$," *Physical Review B*, vol. 93, p.134114, 2016, https://doi.org/10.1103/PhysRevB.93.134114
2. J. Strand, O. A. Dicks, M. Kaviani and A. L. Shluger, "Hole trapping in amorphous HfO_2 and Al_2O_3 as a source of positive charging," *Microelectronic Engineering*, vol. 178, pp. 235-239, 2017, https://doi.org/10.1016/j.mee.2017.05.012
3. O. A. Dicks and A. L. Shluger, "Theoretical modeling of charge trapping in crystalline and amorphous Al_2O_3," *Journal of Physics: Condensed Matter*, vol. 29, p. 314005, 2017, https://doi.org/10.1088/1361-648X/aa7767

Contents

List of Figures

List of Tables

Chapter 1

Introduction

1.1 Background and motivation

Controlling the properties of defects in materials is crucial to developing devices on the nanoscale. In this thesis, defects in $LaAlO_3$ and amorphous Al_2O_3 (a-Al_2O_3) are investigated using atomistic modeling techniques in order to understand their properties and enable experimentalists to positively identify defects in lab grown thin films. Both $LaAlO_3$ and amorphous Al_2O_3 are high k dielectric metal oxides with interesting applications in electronic devices [1]. Their use as dielectrics means that charge trapping in both materials affects device performance, stimulating the interest in their defect properties.

In crystals, a defect is a deviation from the infinite crystal lattice which is not periodically repeated. It is generally created by the removal or addition of an ion into the structure, or the translation of an ion away from its equilibrium lattice position. This traditional definition of a point defect would not seem to apply to amorphous materials, which by their nature are not infinitely repeating in any direction. However, as will be demonstrated in this thesis, local ion relaxations after the removal or addition of atoms into amorphous structures and the resulting effect on electronic structure show that defects can also be created in amorphous metal oxides, analogous to those in crystals.

Defects in materials have been studied since the early part of the 20th century, when it was suggested that point defects caused by the removal of an anion from an alkali halide crystal lattice were responsible for the strongly coloured absorption bands observed from spectroscopy. The study of these ‘colour centres’ led to the understanding that many material properties are determined by defects, the control of which can allow careful tuning of material characteristics for technological applications. For example, the doping of semiconductors with defect impurities was patented in the 1940s [2], allowing control over the majority charge carrier in materials. This enabled the development of p-n junctions and formed the basis of modern computer processors. Now, careful control over defects is necessary when creating materials for use in a variety of fields [3], including photovoltaics [4,5], solid oxide fuel cells [6], and modern nanoelectronics [7].

The origin of this thesis was work done by Littlewood et al. [8,9] and Sushko et al. [10, 11] on $LaAlO_3/SrTiO_3$ heterostructures. With funding from Argonne National Laboratory, and working with Prof. Littlewood, the aim of this project was to investigate controlling the electronic properties of thin films and interfaces using defects. This also meant understanding the properties of defects in the bulk materials, specifically $LaAlO_3$.

$LaAlO_3$ is a polar material, a property which is used to generate a 2-dimensional electron gas (2DEG) at its interface with $SrTiO_3$ [12], despite both being band insulators. Various mechanisms have been proposed for the formation of the 2DEG at the $LaAlO_3/SrTiO_3$ interface, including the polar discontinuity [8,9,13–15], La/Sr intermixing [10,11,16] and defects in both the LAO [17–20] and STO [21] layers. To better understand their role in the formation of the 2DEG, the spectroscopic properties of oxygen vacancies in $LaAlO_3$ were calculated, with the hope that these theoretical predictions would allow experimentalists greater insights into the properties of $LaAlO_3$.

After a change in priorities at Argonne National Laboratory, it was not possible to obtain any experimental data on $LaAlO_3/SrTiO_3$ heterostructures. Instead it was decided to change direction and investigate amorphous Al_2O_3, another high k dielectric metal oxide where control over its electronic properties using defects was of interest to the experimental community. Also, an opportunity to collaborate with Prof. V. Afanas'ev's group at the University of Leuven meant that experimental data on amorphous alumina thin films was kindly made available, offering a point of comparison for the results of the computational modeling performed in this thesis.

Amorphous Al_2O_3 is an important material in the development of a large number of nanoelectronic devices, including non-volatile charge trap flash memory [22, 23], amorphous indium gallium zinc oxide (a-IGZO) thin film transistors [24], and perovskite solar cells [25–27]. It is one of a growing list of metal oxides whose amorphous phase is being studied for use in technological applications, including HfO_2 [28,29], TiO_2 [30,31] and ZrO_2 [29,32].

These metal oxides are not natural glass formers, but when deposited as thin films, using techniques like atomic layer deposition (ALD) [33,34], they often stabilize in their amorphous phase. Amorphous materials differ from crystals in that they are not periodic and show no long range order. Their non-periodicity is accompanied by a wide distribution of bond lengths, bond angles and coordination numbers of ions. This change in structure can affect the electronic properties of the metal oxides. Amorphous oxides can exhibit higher trapping energies of intrinsic polarons [28], band shifting [35] and changes in surface morphology [36]. Adjustments in growth conditions, such as deposition temperature and oxygen partial pressure, allows experimental control over these properties [36].

Whilst amorphous materials open up new opportunities when it comes to the properties of metal oxide thin films, they also create new challenges in modeling the electronic structure of defects. The use of density functional theory (DFT) to calculate the properties of defects in crystals has been well established for decades [37], but the lack of periodicity of amorphous materials, the large variation in local structure, and the uncertainty in experimental data, means modeling defects in amorphous materials brings its own complexities. However, through the use of molecular dynamics and DFT these complexities can be overcome and the properties of amorphous Al_2O_3 calculated.

1.2 Scope of this thesis

In this thesis atomistic modeling methods are used to predict the spectroscopic properties of oxygen vacancies in $LaAlO_3$, and the structural, electronic and charge trapping properties of amorphous Al_2O_3. Through developing our theoretical understanding of defects in these materials, experimentalists are able to identify them, and thus control their properties.

First, the theoretical background of the methods used to model $LaAlO_3$ and amorphous Al_2O_3 are presented. This starts with an explanation of molecular dynamics and the equations that describe classical particle motion. Then, density functional theory (DFT) is discussed, including details of the Gaussian and Plane Wave (GPW) method, hybrid functionals, and the auxiliary density matrix method (ADMM). Following is an explanation of formation energy calculations and the nudged elastic band method (NEB). NEB is used to calculate the energy barriers and lowest energy pathways of ionic displacements. Finally a description of time dependent density functional theory (TDDFT) is given, which allows the calculation of the energies of optical transitions into excited states, and their oscillator strengths.

In chapter 3 the optical absorption spectra and ESR parameters of oxygen vacancies in $LaAlO_3$ are predicted, using DFT, TDDFT and both periodic and embedded cluster methods. The structure, formation energies and Kohn-Sham energy levels of neutral (V_O^0) and charged (V_O^+ and V_O^{2+}) oxygen vacancies in cubic and rhombohedral $LaAlO_3$ are calculated. TDDFT is then used to calculate the optical absorption spectra of V_O^0 and V_O^+. Analysis of the defect's point symmetry explains the shape of the absorption spectra, and the splitting observed in the rhombohedral $LaAlO_3$ peaks. Calculations of the g-tensor and isotropic hyperfine constants of the V_O^+ defect are also reported, which accurately predict the position and width of the ESR signature. When these results are combined, they are shown to explain experimental measurements of oxygen vacancies in $LaAlO_3$ crystals, and help to establish their role at the $LaAlO_3$/$SrTiO_3$ interface.

The next chapter turns to the study of amorphous Al_2O_3. To accurately describe the electronic structure and defect properties of a-Al_2O_3, first a representative sample of structures must be created. To generate these structures, a molecular dynamics melt and quench method is used. Analysis of the structural geometries showed they were in good agreement with experimental x-ray diffraction [38], NMR [39] and density measurements [33]. Careful attention was then paid to tuning the PBE0-TC-LRC [40] functional so as to make it Koopman compliant. DFT calculations of the bulk structure of crystalline α-Al_2O_3 were then used to benchmark the functional. After calculations of a-Al_2O_3, analysis suggests that the observed decrease in its band gap is due to a shifting of the conduction band downwards, as a result of the change in Al coordination number and electrostatic potential profile. This provides support to one competing interpretation of the experimental measurements of the band gap shift [35].

The intrinsic trapping of hole and electron polarons in a-Al_2O_3 is then discussed. The DFT setup described in the previous chapter is first used to calculate the structural and electronic properties of Mg at an Al site (Mg_{Al}) in α-Al_2O_3. The Mg_{Al} defect, in the neutral state, donates a hole into alumina making it a suitable test system. The tuned functional is able to predict the structural properties of defects in Al_2O_3 and to accurately model the localization of holes and electrons in defects and the optical transition properties. Calculation of the Mg_{Al} defect's hyperfine constants are also shown to be in excellent agreement with experiment. Intrinsic hole trapping was then observed in both α-Al_2O_3 and a-Al_2O_3, though trapping energies were much higher in the amorphous structures. Electron polarons are shown not to trap in α-Al_2O_3 or a-Al_2O_3

Having demonstrated that electrons do not self-trap in alumina, the final results chapter discusses the role of defects in the negative charging of a-Al_2O_3 thin films which is observed experimentally [22,23,41,42]. The properties of interstitial hydrogen (H_i), oxygen vacancies (V_O), oxygen interstitials (O_i), aluminium vacancies (V_{Al}) and aluminium interstitials (Al_i) are calculated using DFT. In order to explain the experimental charge trap spectroscopy data [22], a mechanism is proposed whereby negatively charged O_i and V_{Al} defects are compensated by H_i, V_O

and Al_i defects, which are positively charged. The negative charging is then a result of filling the unoccupied states of H_i, V_O and Al_i that lie in the band gap.

The last chapter summarizes the main conclusions of the thesis and suggests future work that would build upon its results.

1.3 Main results

Here is a short summary of the main findings presented in this thesis:

- V_O^+ in rhombohedral $LaAlO_3$ exhibits an optical absorption peak which extends from 3.2-4.0 eV, with a maximum at 3.6 eV. Its isotropic g-value is calculated to be 2.004026, and due to the nearest neighbour Al ions there is a calculated hyperfine splitting which leads to a 3.0 mT broadening of the EPR signal. These results are in good agreement with experimental EPR and absorption spectra measurements of oxygen deficient $LaAlO_3$ [43].

- DFT calculations predict that a-Al_2O_3 has an average HOMO-LUMO gap of 5.48 eV, a significant reduction from the 8.6 eV band gap of crystalline α-Al_2O_3. Analysis shows that the change in Al coordination shifts the Al electrostatic potential downwards by 1.6 V, causing the conduction band to lower. This provides theoretical evidence for the conduction band lowering observed experimentally [35].

- Hole polarons are shown to spontaneously trap in a-Al_2O_3 with an average trapping energy of 1.26 eV, higher than the 0.38 eV trapping energy calculated for holes in α-Al_2O_3. The edge of the valence band is shown to be highly localized as a result of 2 coordinated oxygen σ_{2p}^* states. These localized states results in a trap site density of 2.6×10^{20} cm^{-3}. Electron polarons are shown not trap in a-Al_2O_3 or α-Al_2O_3, due to the delocalized nature of the conduction band minimum.

- From DFT calculations of the H_i, V_O, O_i, V_{Al} and Al_i defects, a theory is proposed to explain experimental trap spectroscopy measurements [22]. O_i

has a (0/-2) charge transfer level that lies on average 3.4 eV below the a-Al_2O_3 conduction band minimum, and V_{Al} has a (-2/-3) charge transfer level lying 3.5 eV below the conduction band minimum. Though they act as deep acceptors, they have no Kohn-Sham levels in the gap and so must be compensated by Al_i, V_O or H_i, which have unoccupied states in the band gap in their positive charge states. After electron injection, these states become occupied and transitions in the energy range 2.7-4.0 eV can be observed, in accordance with experiment [22].

Chapter 2

Methodology

In order to accurately describe the electronic and structural properties of crystalline and amorphous systems and their defects a variety of modelling techniques are required. Here the theoretical background of the methods common to later chapters is covered. Specific techniques and methods pertinent to individual chapters are addressed at the beginning of those chapters, along with the specific details of any calculations. Within this methodology chapter a brief overview of molecular dynamics (MD) is first given. This is followed by a description of density functional theory (DFT) and aspects of its implementation in the CP2K code [44], specifically the use of the Gaussian and Plane Wave (GPW) method, details of the PBE0-TC-LRC functional and the auxiliary density matrix method (ADMM). After DFT, formation energy calculations are described and the theory behind the nudged elastic band (NEB) method is explained. The chapter is concluded by a description of time dependent density functional theory (TDDFT).

2.1 Molecular Dynamics

Molecular dynamics (MD) allows the trajectories of a large number of ions to be determined using classical Newtonian mechanics. It is widely used to model large interacting systems of atoms in solids and liquids. Modelling atomic trajectories requires the force on each atom in the interacting system to be calculated, from which the trajectories can then be determined using the classical equations of motion. These forces are in turn derived from the total potential energy of the system, $U(\{\mathbf{R}\})$, where $\{\mathbf{R}\}$ is the complete set of atomic coordinates of the system $(\mathbf{R}_1, \mathbf{R}_2, \mathbf{R}_3 \ldots)$. The total potential energy is dependent on the interactions between atoms, and can be determined using either classical potentials, or from quantum mechanical calculations. Classical potentials use relatively simple functions to model the complex interaction between nuclei and electrons. In the case of quantum mechanical calculations (such as density functional theory, see section 2.2.1), the Born-Oppenheimer approximation is assumed, with the electronic contribution to the energy dependent on fixed nuclei positions, and the nuclear trajectory then determined using MD. In this thesis molecular dynamics has been principally used to generate amorphous structures of Al_2O_3 with the melt and quench method, described in chapter 4.2.1, using classical inter-atomic potentials.

2.1.1 Classical potentials

Classical potentials are analytic functions that model the complex interactions between nuclei and electrons in order to allow the calculation of a system's total potential energy, without the need to explicitly solve the Schrodinger equation. This means the total energy can be given as a sum of the intra- and inter-atomic potentials of the atoms:

$$U(\{\mathbf{R}\}) = \sum_i V_{\text{ext}}(\mathbf{R}_i) + \sum_i \sum_{j>i} V_{\text{pair}}(\mathbf{R}_i, \mathbf{R}_j) + \sum_i \sum_{j>i} \sum_{k>j} V_{\text{3-body}}(\mathbf{R}_i, \mathbf{R}_j, \mathbf{R}_k) + \ldots \tag{2.1}$$

where $U(\{\mathbf{R}\})$ is the total energy of a system in configuration $\{\mathbf{R}\}$. In the first term, $V_{\text{ext}}(\mathbf{R}_i)$ is the 'one-body' potential, which in a periodic system is the result of an externally applied field. $V_{\text{pair}}(\mathbf{R}_i, \mathbf{R}_j)$ is the 2 body potential and tends to be the largest contributor to the total energy. It describes the interactions between pairs of atoms. $V_{\text{3-body}}(\mathbf{R}_i, \mathbf{R}_j, \mathbf{R}_k)$ is the 3-body potential term, which allows the inclusion of angle-dependent terms often included for covalently bonded systems. Higher order terms, such as 4-body potentials, can also be included.

In chapter 4, a pair-wise (2-body) potential is sufficient to generate accurate structures of amorphous Al_2O_3. Here the specific treatment of electrons is neglected and atoms are treated as charged ions, with repulsive terms included to model the effects of electron exchange, a result of the Pauli exclusion principle. It takes the form [45,46]

$$V(R_{ij}) = \frac{q_i q_j}{R_{ij}} - \frac{C_i C_j}{R_{ij}^6} + D(B_i + B_j)\exp\left(\frac{A_i + A_j - R_{ij}}{B_i + B_j}\right), \tag{2.2}$$

where R_{ij} is the distance between pairs of atoms, q_i is the charge of atom i, and A, B and C are constants dependent on the atomic species of the pair of atoms. The first term of the potential is the Coulomb interaction between pairs of ions, and in a system with periodic boundary conditions it is calculated using the Ewald summation method [47]. The second term, C_iC_j/R_{ij}^6, represents a van der Waals interaction. The third term models the short range repulsion which prevents ions from approaching too close, as electron orbitals overlap and Pauli exclusion comes into play.

Although the form of various classical potentials differ, they often contain similar long range Coulomb interactions and short range repulsive and attractive terms that mimic ionic and covalent bonding. The terms of the potentials can then be parameterized empirically using structural data (from diffraction experiments), elastic constants and other physical properties, or fitted using quantum mechanical calculations. These potentials can then be used to calculate the total potential energy of a system.

2.1.2 The equations of motion and the Verlet integration scheme

After calculating the total energy of the system in configuration $\{\mathbf{R}\}$ through the use of potentials or ab initio methods, the evolution of the atom trajectories can be considered. The force, $\mathbf{F}_I$, acting on ion I, is given by the expression

$$\mathbf{F}_I = -\frac{\partial U(\{\mathbf{R}\})}{\partial \mathbf{R}_I}, \tag{2.3}$$

where U is the total energy of the system and $\mathbf{R}_I$ is the position vector of ion I. The time evolution of the ions is then Newton's equation of motion;

$$\mathbf{F}_I = M_I \frac{d^2\mathbf{R}_I}{dt^2} \ , \tag{2.4}$$

where M_I is the ion mass.

Solving the trajectories from equation 2.4 is an N body problem, where N can be in the 10s of thousands (or larger) for MD calculations. This means the time evolution of the ion positions cannot be solved analytically but instead has to be obtained through an iterative method. The integration of the equation of motion of the ions is carried out numerically using small fixed time steps, δt.

A commonly employed method is the Verlet [48] algorithm, which Taylor expands the ion coordinates forwards and backwards a time step, around the point in time, t, so that

$$\mathbf{R}_I(t+\delta t) = \mathbf{R}_I(t) + \frac{d\mathbf{R}_I(t)}{dt}\delta t + \frac{\mathbf{F}_I(t)}{2M_I}\delta t^2 + \frac{\mathbf{b}_I(t)}{6}\delta t^3 + O(\delta t^4) \tag{2.5}$$

$$\mathbf{R}_I(t-\delta t) = \mathbf{R}_I(t) - \frac{d\mathbf{R}_I(t)}{dt}\delta t + \frac{\mathbf{F}_I(t)}{2M_I}\delta t^2 - \frac{\mathbf{b}_I(t)}{6}\delta t^3 + O(\delta t^4) \tag{2.6}$$

By adding both equations 2.5 and 2.6 an expression for the ion position after one time step is obtained;

$$\mathbf{R}_I(t+\delta t) = 2\mathbf{R}_I(t) - \mathbf{R}_I(t-\delta t) + \frac{\mathbf{F}_I(t)}{M_I}\delta t^2 + O(\delta t^4) \tag{2.7}$$

which cancels out the velocity and the cubic terms, meaning the equation is accurate to the fourth order. The algorithm only requires the current and previous ion positions, and the calculation of the force from the potential energy, to calculate the next position. The velocities can also be calculated from the subtraction of equation 2.6 from 2.5, so that after rearranging

$$\mathbf{v}_I(t) = \frac{1}{2\delta t}[\mathbf{R}_I(t+\delta t) - \mathbf{R}_I(t-\delta t)] + O(\delta t^3) \ . \tag{2.8}$$

2 initial time step positions are needed to apply the Verlet algorithm. These are obtained from the input coordinates of the ions, with the position after the first time step calculated using a random velocity that fits a pre-defined velocity distribution profile. Thus by applying the Verlet algorithm and using classical or quantum mechanical models of the potential energy the trajectories of all ions in the system can be obtained.

2.2 Density Functional Theory

2.2.1 General theory of DFT

DFT is a well established technique for modelling the electronic structure of molecules and solids and has been used extensively in this work. Although it is well understood, a brief outline of it will be given here to allow further discussion of its implementation.

In order to understand the properties of a material the Schrodinger equation has to be solved for N interacting electrons experiencing an external field $v(\mathbf{r})$, predominantly due to the nuclei present. The Hamiltonian of the material system is

$$H = T + U + V = H_0 + V \tag{2.9}$$

where T is the sum of the kinetic energy of the electrons, U is the sum of the Coulomb interactions of the electrons with each other and V is the sum of the electron-nuclei Coulomb interactions. The Born-Oppenheimer approximation has been applied to this Hamiltonian, which does not include the nuclear kinetic energy term, and thus assumes that the nuclei remain in fixed positions. This allows the electronic and nuclear parts of the wavefunction to be treated separately and the total wavefunction becomes

$$\Psi_{\text{Total}} = \Psi_{\text{nuclear}}(\{\mathbf{R}\}) \times \Psi_{\text{electronic}}(\{\mathbf{R}\}, \{\mathbf{r}\}) \tag{2.10}$$

where $\{\mathbf{r}\}$ are the set of electronic coordinates and $\{\mathbf{R}\}$ is the set of nuclear coordinates, which enter the electronic wavefunction as a parameter.

The expectation value of the Hamiltonian (in equation 2.9) is the ground state energy of the system,

$$E_{\mathrm{g}} = \langle \Psi | H_0 + V | \Psi \rangle \tag{2.11}$$

where Ψ is the many-electron wavefunction of the system ($\Psi_{\mathrm{electronic}}(\{\mathbf{R}\}, \{\mathbf{r}\})$ in equation 2.10). However, calculating the many-electron wavefunction Ψ is practically impossible with modern techniques and computational power, except for the simplest of systems (i.e. Hydrogen). Instead, the ground state energy can be calculated as a functional of the electron density $\rho(\mathbf{r})$, which is a function of merely the 3 spatial coordinates.

Using the density rather than the many-electron wavefunction to determine the ground state properties of the system is justified by the 2 Hohenberg-Kohn theorems [49]. The first theorem states that 2 potentials $v(\mathbf{r})$ and $v'(\mathbf{r})$ that differ by more than an additive constant do not have the same ground state density $\rho(\mathbf{r})$. It also implies that the ground state energy E_{g} can be calculated from the equation

$$E_{\mathrm{g}} = \left[\int d\mathbf{r}\; v(\mathbf{r})\rho(\mathbf{r}) \right] + F[\rho(\mathbf{r})] \tag{2.12}$$

where the first part of the equation determines the energy of the electrons interacting with the external potential $v(\mathbf{r})$ and $F[\rho(\mathbf{r})]$ is a universal functional of the density which determines the kinetic energy of the electrons and the energy of the electron-electron interactions. The second Hohenberg-Kohn theorem states that given the external potential $v(\mathbf{r})$, the ground state energy can be obtained by minimizing equation 2.12 with respect to $\rho(\mathbf{r})$. The expression for the total ground state energy of the electronic system (in a fixed nuclear environment) is normally expressed as a functional of the density in the form

$$E_{\mathrm{g}}[\rho(\mathbf{r})] = E_{\mathrm{kin}}[\rho(\mathbf{r})] + E_{\mathrm{ext}}[\rho(\mathbf{r})] + E_{\mathrm{Har}}[\rho(\mathbf{r})] + E_{\mathrm{xc}}[\rho(\mathbf{r})] \tag{2.13}$$

where E_{kin} is the kinetic energy of the electrons, E_{ext} is the energy due to the external potential, E_{Har} is the Hartree energy and E_{xc} is the exchange-correlation energy. Unfortunately, the exact form of the exchange-correlation functional is currently unknown and so it has to be approximated in order to calculate its contribution to the energy, these approximations are discussed in section 2.2.4. Aside from the fact that the exchange-correlation functional is unkown, it has also proven difficult to calculate the $E_{\text{kin}}[\rho(\mathbf{r})]$ term in equation 2.13, as there is currently no acceptably accurate functional to determine the kinetic energy term directly from the density, $\rho(\mathbf{r})$. This is addressed by the Kohn-Sham [50] (KS) approach to DFT where the density

$$\rho(\mathbf{r}) = \sum_{i=1}^{N} |\psi_i|^2 \tag{2.14}$$

where ψ_i are the single particle wave functions of non-interacting electrons that produce the same density as the physical system (the same as the probability density of the many-electron wavefunction). The single particle wave functions can be computed by way of the self consistent field (SCF) method using the Kohn-Sham equation [50],

$$\left[-\frac{1}{2}\nabla^2 + (V_{\text{ext}}(\mathbf{r}) + V_{\text{Har}}(\mathbf{r}) + V_{\text{xc}}(\mathbf{r}))\right] \psi_i(\mathbf{r}) = \varepsilon_i \psi_i(\mathbf{r}), \tag{2.15}$$

where V_{ext} is the external potential (which is pre-determined and normally due to the nuclei), V_{Har} is the Hartree potential (electron-electron Coulomb interaction) given by

$$V_{\text{Har}}(\mathbf{r}) = \int d\mathbf{r}' \frac{\rho(\mathbf{r}')}{|\mathbf{r} - \mathbf{r}'|} \tag{2.16}$$

and V_{xc} is the exchange-correlation potential. All of these terms can be exactly calculated using the electron density except for V_{xc}, whose true form is unknown. Improvements in calculating the electronic structure of crystals comes from finding better approximations to V_{xc} which is the functional derivative of the unkown energy functional $E_{\text{xc}}[\rho(\mathbf{r})]$;

$$V_{\text{xc}}(\mathbf{r}) = \frac{\delta E_{\text{xc}}[\rho(\mathbf{r})]}{\delta \rho(\mathbf{r})} . \tag{2.17}$$

Common approximations are the local density approximation (LDA), the generalized gradient approximation (GGA), and hybrid functionals which include a portion of exact exchange [51,52].

2.2.2 Periodic boundary conditions and k-point sampling

Physical samples of crystals or solid materials tend to contain on the order of 10^{23} atoms, far to many to model explicitly using DFT. Instead, by using periodic boundary conditions infinite bulk solids can be modelled. This is especially useful for crystals, which by their nature are periodic, but can also be used to simulate pseudo-amorphous materials through the use of large simulation cells.

A crystal will have a potential with periodic boundary conditions (due to a repeated motif of atoms) which takes the form:

$$V(\mathbf{r}) = V(\mathbf{r}+\mathbf{R}), \tag{2.18}$$

where $\mathbf{R}$ is a Bravais lattice vector. A Bravais lattice describes a system where any position translated by a lattice vector is equivalent. The lattice vector is defined as,

$$\mathbf{R} = n_1\mathbf{a}_1 + n_2\mathbf{a}_2 + n_3\mathbf{a}_3, \tag{2.19}$$

where $\mathbf{a}_\mathrm{i}$ are the primitive lattice vectors, and n_i are integers.

Having defined the real space lattice, the reciprocal lattice can be defined. This is the Bravais lattice of all allowed $\mathbf{k}$ vectors of a plane wave, $e^{i\mathbf{k}\cdot\mathbf{r}}$, that has the same periodicity as the real space Bravais lattice described by $\mathbf{R}$. The reciprocal lattice vector, $\mathbf{G}$, must satisfy the condition that:

$$e^{i\mathbf{G}\cdot(\mathbf{r}+\mathbf{R})} = e^{i\mathbf{G}\cdot\mathbf{r}}, \tag{2.20}$$

where the plane wave has the same periodicity as the real space lattice. From equation 2.20 it can be clearly seen that

$$e^{i\mathbf{G}\cdot\mathbf{R}} = 1, \tag{2.21}$$

and from here $\mathbf{G}$ can be calculated. The reciprocal lattice vectors, $\mathbf{G}$, can be formed from primitive vectors of the reciprocal lattice, $\mathbf{b}_i$, where

$$\mathbf{G} = g_1\mathbf{b}_1 + g_2\mathbf{b}_2 + g_3\mathbf{b}_3, \tag{2.22}$$

as long as

$$\mathbf{b}_i \cdot \mathbf{a}_j = 2\pi\delta_{ij} \tag{2.23}$$

and g_i are integers, otherwise equation 2.21 won't be satisfied. It is useful to note that all the points in reciprocal space closest to a single lattice point are defined as the first Brillouin zone, the Wigner-Seitz cell (or unit cell) of the reciprocal lattice.

Next the wavefunctions of electrons in periodic potentials can be considered, which allows the construction of Kohn-Sham orbitals for DFT calculations. From Bloch's theorem, the one electron wavefunction (which can be used to describe the Kohn-Sham non-interacting electron wavefunctions used in equation 2.15) of a system with a periodic potential can be written as a Bloch function:

$$\psi_{n\mathbf{k}}(\mathbf{r}) = e^{i\mathbf{k}\cdot\mathbf{r}}u_{n\mathbf{k}}(\mathbf{r}) \tag{2.24}$$

where

$$u_{n\mathbf{k}}(\mathbf{r}) = u_{n\mathbf{k}}(\mathbf{r}+\mathbf{R}) \tag{2.25}$$

is a function with the same periodicity as the lattice, where n and $\mathbf{k}$ specify all possible electronic states. Bloch functions have the property that:

$$\psi_{n\mathbf{k}}(\mathbf{r}+\mathbf{R}) = e^{i\mathbf{k}\cdot(\mathbf{r}+\mathbf{R})}u_{n\mathbf{k}}(\mathbf{r}+\mathbf{R}) = e^{i\mathbf{k}\cdot\mathbf{R}}\psi_{n\mathbf{k}}(\mathbf{r}), \tag{2.26}$$

demonstrating that a translation of the Bloch function by a lattice vector results in the same function with an additional phase factor.

Bloch functions are used to solve equation 2.15 (the Kohn-Sham equation) for systems with periodic boundary conditions, often involving Fourier transforms. The main advantage being that the periodicity of the reciprocal lattice and the properties of Bloch functions allows integrals over k-space to be re-formed as integrals over just the 1st Brillouin zone, where all unique *k*-points are described. This is because any wavevector $\mathbf{k}'$ can be rewritten as

$$\mathbf{k}' = \mathbf{k} + \mathbf{G}, \tag{2.27}$$

where $\mathbf{k}$ belongs to the first Brillouin zone. Bands extending outside the first Brillouin zone are therefore ‘folded’ into the first Brillouin zone, with multiple energies described at each unique *k*-point, as a sum over the reciprocal lattice vectors.

In an infinite lattice with an infinite number of electrons, there are also an infinite number of *k*-points in the first Brillouin zone. If it is assumed that the energy as a function of $\mathbf{k}$ is smoothly varying then the integral over all k-points can be replaced with a sum over a finite mesh of k-points, the most common scheme of which is that proposed by Monkhorst and Pack [53].

The Monkhorst-Pack [53] scheme for sampling the Brillouin zone involves evenly spacing the *k*-points to be calculated within the first Brillouin zone, and ignoring any symmetrically equivalent *k*-points. The *k*-points are determined by the expression

$$\mathbf{k} = u_1\mathbf{b}_1 + u_2\mathbf{b}_2 + u_3\mathbf{b}_3, \tag{2.28}$$

where the fractions

$$u_i = \frac{2r - q - 1}{2q} \qquad r = \{1, 2, 3, ..., q\}, \tag{2.29}$$

and the integer q determines the number of *k*-points sampled. However, in this thesis, periodic calculations have been undertaken using the Γ point code CP2K [44], which means all calculations are performed at $\mathbf{k} = 0$. In order to accurately calculate energy dispersion at the Γ point, larger supercells have to be used. This is because as the lattice parameters are increased, the size of the Brillouin zone decreases and more effective *k*-points are sampled as the bands are folded in. This can be seen in equation 2.23, where $|\mathbf{b}_i|$ decreases as $|\mathbf{a}_i|$ increases, meaning doubling the size of the supercell halves the size of the first Brillouin zone. This is utilized to calculate the electronic structure of amorphous solids, where real systems are not periodic.

In this instance it is more advantageous to use cells with as large a number of atoms as possible, as opposed to having a dense k-grid.

2.2.3 Gaussian and Plane Wave (GPW) method

In order to perform KS DFT a suitable basis set has to be defined with which to construct the KS wavefunction and electron density. The periodic DFT code CP2K [44], which has been used extensively in this work, makes use of the Gaussian and plane wave (GPW) method [54] in order to reduce the computational cost of calculating various terms of the energy functional by using the most efficient basis set. This allows the calculation of large systems, which is essential for understanding the properties of amorphous systems and allows greater structural relaxations when studying defects.

Gaussian type basis sets are atom centred and in the GPW representation are used to construct the KS orbitals. They are composed of atomic orbitals

$$\phi_{\alpha}(\mathbf{r}) = \sum_{i} C_{i\alpha} g_i(\mathbf{r}), \tag{2.30}$$

where $C_{i\alpha}$ are constant coefficients and g_i are primitive Gaussian functions of the form

$$g_i(\mathbf{r}) = e^{-a_i r^2}. \tag{2.31}$$

The density is then defined using the Kohn-Sham (molecular) orbitals, ψ_{β} which are a linear combination of atomic orbitals

$$\psi_{\beta}(\mathbf{r}) = \sum_{j} D_{j\beta} \phi_j(\mathbf{r}), \tag{2.32}$$

where $D_{j\beta}$ are coefficients that are varied with each calculation step. This means the density can be written

$$\rho(\mathbf{r}) = \sum_{\beta} f_{\beta} |\psi_{\beta}|^2, \tag{2.33}$$

where f_{β} is the occupation of the KS orbitals. The density can also be written in terms of the atomic orbitals and the density matrix elements P_{ij}

$$\rho(\mathbf{r}) = \sum_{ij} P_{ij}\phi_i(\mathbf{r})\phi_j(\mathbf{r}) \,. \tag{2.34}$$

The density can also be represented using plane waves in the form

$$\rho(\mathbf{r}) = \frac{1}{\Omega}\sum_{\mathbf{G}} \tilde{\rho}(\mathbf{G})\exp(i\mathbf{G}.\mathbf{r}) \tag{2.35}$$

where Ω is the volume of the unit cell, $\mathbf{G}$ are the reciprocal lattice vectors and $\tilde{\rho}(\mathbf{G})$ are the expansion coefficients. As the real space basis is expressed in terms of Gaussians, $\tilde{\rho}(\mathbf{G})$ can be determined using Fast Fourier Transforms (FFT) by noting that the product of 2 Gaussians is a Gaussian, and its Fourier transform is also a Gaussian. In theory the expression shown in equation 2.35 is an exact representation of the density, in practice an energy cutoff is applied which limits the sum over lattice vectors to plane waves with a kinetic energy less than the cutoff.

The GPW method allows efficient calculation of the energy functional using the most suitable basis set for each energy term. The energy functional is then given by the expression

$$E[\rho(\mathbf{r})] = \sum_{ij} P_{ij}\left\langle\phi_i(\mathbf{r})\right| -\frac{1}{2}\nabla^2 \left|\phi_j(\mathbf{r})\right\rangle \tag{2.36}$$

$$+\sum_{ij} P_{ij}\left\langle\phi_i(\mathbf{r})\right| V_{\mathrm{loc}}^{\mathrm{PP}}(r) \left|\phi_j(\mathbf{r})\right\rangle + \sum_{ij} P_{ij}\left\langle\phi_i(\mathbf{r})\right| V_{\mathrm{nl}}^{\mathrm{PP}}(\mathbf{r},\mathbf{r}') \left|\phi_j(\mathbf{r}')\right\rangle \tag{2.37}$$

$$+2\pi\Omega\sum_{\mathbf{G}}\frac{\tilde{\rho}(\mathbf{G})\tilde{\rho}(\mathbf{G})}{\mathbf{G}^2} \tag{2.38}$$

$$+\int \varepsilon_{\mathrm{xc}}(\mathbf{r})d\mathbf{r} + \frac{1}{2}\sum_{I\neq J}\frac{Z_I Z_J}{|\mathbf{R}_I - \mathbf{R}_J|} \,. \tag{2.39}$$

where part 2.36 is the kinetic energy of the electrons, part 2.37 describes the energy of the electron interaction with the local and non-local part of the pseudo-potential describing the ion potential and the core electrons, part 2.38 is the Hartree energy and part 2.39 is the exchange-correlation energy and the interaction energy of the ionic cores. The use of the Gaussian basis set for the majority of terms allows for efficient calculation, as its integrals can be determined analytically. The Hartree energy (part 2.39) is calculated in reciprocal space and uses the plane wave representation of the density, allowing a large speed up of the calculation. The pseudopotential term is introduced to reduce the number of electrons in the calculation, as often only the valence electrons are of interest. In the CP2K [44] code the Goedecker-Teter-Hutter (GTH) pseudopotentials [55,56] are used.

2.2.4 The exchange-correlation functional

Unfortunately there is no default choice for the exchange-correlation (XC) functional in DFT, instead the level of approximation has to be chosen based on the properties being investigated, the system size and the computational resources available. The most simple choice of XC functional is the local density approximation (LDA) which was proposed in the original Kohn-Sham DFT paper [50]. It is given by the expression

$$E_{\mathrm{xc}}[\rho(\mathbf{r})] = \int d\mathbf{r}\varepsilon_{\mathrm{xc}}^{\mathrm{LDA}}(\rho(\mathbf{r}))\,, \tag{2.40}$$

where $\varepsilon_{\mathrm{xc}}$ is the energy density, a function dependent only on $\rho(\mathbf{r})$. Although inexpensive computationally and reasonably accurate when calculating lattice parameters it tends to overestimate binding energies by about 1 eV/bond.

The next level of approximation to the XC functional are the general gradient approximation (GGA) functionals, such as PBE [57,58]. Here the energy density is dependent on both the local density and the gradient of the density at the point $\mathbf{r}$ and is given by

$$E_{\mathrm{xc}}[\rho(\mathbf{r})] = \int d\mathbf{r}\varepsilon_{\mathrm{xc}}^{\mathrm{GGA}}(\rho(\mathbf{r}), |\nabla\rho(\mathbf{r})|)\,. \tag{2.41}$$

GGA functionals require differentiation of the density leading to more computationally expensive calculations than LDA functionals. Both types of functional are unable to correctly predict the electronic structure of most materials, with the KS band gap usually severely underestimated,often by a factor of 2 in the case of wide gap insulators. They also tend to increase delocalization of holes and electrons in defects and so cannot accurately predict charge trapping or charge transfer energy level positions. In order to address these issues hybrid functionals can be introduced which separate the exchange and correlation parts of the functional and include a portion of the exact exchange.

2.2.5 PBE0-TC-LRC functional

The hybrid functional PBE0-TC-LRC [40] is used extensively throughout this work. This functional has been introduced to allow efficient and accurate calculation of exact exchange in Γ point codes, such as CP2K, and provides large speedup of the calculations without loss of accuracy. The exchange-correlation part of the PBE0-TC-LRC functional has the form

$$E_{\mathrm{xc}} = aE_{\mathrm{x}}^{\mathrm{HF,TC}} + aE_{\mathrm{x}}^{\mathrm{PBE,LRC}} + (1-a)E_{\mathrm{x}}^{\mathrm{PBE}} + E_{\mathrm{c}}^{\mathrm{PBE}} \; . \tag{2.42}$$

PBE0 is the standard PBE hybrid functional [57, 58], with the proportion of exact exchange, a = 0.25. $E_{\mathrm{x}}^{\mathrm{HF,TC}}$ is the truncated Hartree-Fock exchange, $E_{\mathrm{x}}^{\mathrm{PBE,LRC}}$ is the long range PBE exchange with a truncated Coulomb potential, $E_{\mathrm{x}}^{\mathrm{PBE}}$ is the PBE exchange and $E_{\mathrm{c}}^{\mathrm{PBE}}$ is the PBE correlation. The truncated Coulomb (TC) version of the Hartree-Fock exchange takes the form

$$E_{\mathrm{x}}^{\mathrm{HF,TC}} = -\frac{1}{2}\sum_{i,j}\iint \psi_i(r_1)\psi_j(r_1)g_{\mathrm{tc}}(r_{12})\psi_i(r_2)\psi_j(r_2)d^3r_1d^3r_2 \tag{2.43}$$

where the operator

$$g_{\mathrm{tc}}(r_{12}) = \begin{cases} \frac{1}{r_{12}} & \text{for } r_{12} < R \\ 0 & \text{for } r_{12} > R \end{cases} \tag{2.44}$$

and R is the cutoff parameter. The introduction of the cutoff is necessary in order to converge the expression for the exchange energy when calculated at the Γ point [59]. The cutoff radius is constrained so that its maximum should be less than the radius of the smallest sphere that fits inside the cell. This is imposed in order to prevent pairwise exchange between distinguishable electrons in different cells. In practice the constraint is imposed is that $R < L/2$ where L is the smallest lattice parameter in an orthorhombic cell, though more care has to be taken in cells with different symmetries. The long-range correction (LRC) is based on the spherically averaged

PBE exchange hole [40]. This functional is similar to HSE06 [60–62] in that, unlike many other range-separated hybrid functionals, it uses short-range exact exchange and a long-range semi-local functional.

2.2.6 Auxiliary Density Matrix Method (ADMM)

The use of hybrid functionals, such as those described above, requires the calculation of the Hartree-Fock (exact) exchange, as given in equation 2.43. Equation 2.43 can be rewritten in terms of the density matrix, P (see equation 2.34), and the 2 electron integrals so that

$$E_{\mathrm{x}}^{\mathrm{HF}}[P] = -\frac{1}{2}\sum_{ijkl} P_{ij}P_{kl}(ik|lj) \ . \tag{2.45}$$

Calculation of the exact exchange scales to the fourth order with size of basis set and thus significantly increases the computational cost. The auxiliary density matrix method (ADMM) speeds up the calculation by replacing the orginal density matrix P, with one that is smaller in size, $\widetilde{P}$, known as the auxiliary density matrix. The exchange energy can then be written in terms of $\widetilde{P}$ so that

$$E_{\mathrm{x}}^{\mathrm{HF}}[P] = E_{\mathrm{x}}^{\mathrm{HF}}[\widetilde{P}] + \left[E_{\mathrm{x}}^{\mathrm{HF}}[P] - E_{\mathrm{x}}^{\mathrm{HF}}[\widetilde{P}]\right] \tag{2.46}$$

and then an approximation to the second term on the RHS of the expression can be made so that

$$E_{\mathrm{x}}^{\mathrm{HF}}[P] \approx E_{\mathrm{x}}^{\mathrm{HF}}[\widetilde{P}] + \left[E_{\mathrm{x}}^{\mathrm{GGA}}[P] - E_{\mathrm{x}}^{\mathrm{GGA}}[\widetilde{P}]\right] \ . \tag{2.47}$$

The precise difference in the exchange energy between the original and auxiliary densities is approximated by the difference calculated using the exchange part of the GGA functional. Even though the absolute total value of the exchange energy does significantly differ between the GGA and Hartree-Fock method, the change in the exact exchange energy, as the density varies with each SCF step, is well approximated by the GGA functional.

The primary density matrix is reconstructed using an auxiliary basis set which is smaller than the primary basis set. The KS orbitals, ψ_i are re-written using the auxiliary basis set as

$$\widetilde{\psi}_i(\mathbf{r}) = \sum_j \widetilde{D}_{ij}\widetilde{\phi}_j(\mathbf{r}) \tag{2.48}$$

where $\widetilde{\phi}_j(\mathbf{r})$ are the atomic orbitals of the contracted basis set. This means the reduced density matrix

$$\widetilde{P}_{ij} = \sum_k \widetilde{D}_{ik}\widetilde{D}_{jk}\ . \tag{2.49}$$

The new KS orbital coefficients, $\widetilde{D}_{ij}$, are chosen so as to minimize the absolute difference with the KS orbitals described using the primary basis set. Through the use of ADMM and PBE0-TC-LRC [40] large systems of 100s of atoms can be calculated in CP2K using hybrid functionals.

2.3 Calculating defect formation energies

In order to determine the thermodynamic stability of various defects and their charge transition levels, the formation energies of neutral and charged defects in periodic systems are calculated using the method outlined by Lany and Zunger [63]. The formation energy [63] is given by the formula

$$\Delta H_{\mathrm{D},q} = [E_{\mathrm{D,q}} - E_{\mathrm{bulk}}] + \sum_\alpha n_\alpha \mu_\alpha + q(E_{\mathrm{V}} + \Delta E_{\mathrm{F}}) + E_{\mathrm{corr}}\,, \tag{2.50}$$

where $\Delta H_{\mathrm{D},q}$ is the formation energy of a defect D with charge q, $E_{\mathrm{D,q}}$ and E_{bulk} are the total energy of the system with and without the defect, respectively, n_α are the numbers of species of each type removed ($n_\alpha \geq 0$) or added ($n_\alpha \leq 0$) to the bulk cell, and μ_α are their respective chemical potentials. E_{V} is the difference between the energies of the bulk neutral system and the bulk system with a $+|e|$ charge and ΔE_{F} is the difference between the Fermi level (electron chemical potential) and the valence band maximum (VBM).

The term E_{corr} is the correction to the formation energy that accounts for the electrostatic interaction between periodic images of the charged defect, embedded in a screening background charge (making the overall charge of the cell neutral). This correction only applies to defects that are calculated in a system with periodic boundary conditions. In this thesis, the Lany and Zunger method is used to calculate the charge correction term [64,65]. The charged defect is treated as a series of point charges within a periodic lattice that has a uniform background screening charge, with the correction given by the expression [64,65];

$$E_{\mathrm{corr}} = \left[1 - c_{\mathrm{sh}}\left(1 - \frac{1}{\varepsilon}\right)\right]\frac{q^2\alpha_{\mathrm{Mad}}}{2\varepsilon L}\,, \tag{2.51}$$

where q is the charge of the defect, ε is the macroscopic dielectric constant of the material, α_{Mad} is the Madelung constant for a charge in a periodic system with the system cell geometry, L is the linear supercell dimension ($L = \Omega^{-1/3}$ where Ω is the cell volume), and c_{sh} is a constant that depends on the shape of the supercell [65]. For cubic cells $c_{\mathrm{sh}} = \pi/3\alpha_{\mathrm{Mad}}$, and it is trivial to compute for tetragonal cells [65].

Calculations of defects in embedded clusters are also presented in this thesis. The expression for the formation energy of these systems differs from that in the periodic case as there are no periodic image charges, or background screening charge, to correct for. Instead a correction has to be applied as a result of the polarization of the fixed charges in the cluster that are not allowed to relax when a charge is introduced into the centre of the system. The formation energy of a defect in an embedded cluster is given by the expression

$$\Delta H^{\mathrm{cluster}}_{\mathrm{D},q} = [E^{\mathrm{cluster}}_{\mathrm{D},q} - E^{\mathrm{cluster}}_{\mathrm{bulk}}] + \sum_{\alpha} n_\alpha \mu_\alpha + q(E_{\mathrm{V}} + \Delta E_{\mathrm{F}}) + E_{\mathrm{pol}}\,, \tag{2.52}$$

similar to that for the periodic system except with a correction term, E_{pol}, as a result of the polarization of the embedding charges. The correction [66] is based on the Mott-Littleton [67] method and is defined as

$$E_{\mathrm{pol}} = \frac{q^2}{2R}(1 - \frac{1}{\varepsilon}) \tag{2.53}$$

where q is the defect charge, ε is the dielectric constant and R is the radius of the region allowed to fully relax. This energy is due to the interaction of the dipoles induced on the rigid lattice of ions outside the ‘cavity’ of radius R when a charge is introduced to the centre of the cluster. Inside the cavity both ions and electrons are able to respond to the polarization and therefore correctly contribute to the energy. In the case of neutral defects the relaxation effects are much shorter ranged and relate mainly to the displacement of nearest neighbours.

2.4 Nudged elastic band calculations

The nudged elastic band (NEB) method [68] allows the minimum energy path (MEP) of a transition between an initial and a final state of a system to be calculated. This has important applications in calculating the activation energy for certain reactions in materials and can be used to calculate reaction and diffusion rates. Here it is used to calculate the activation energy for hole polaron transitions between precursor sites.

First the initial ($\mathbf{R}_0$) and final ($\mathbf{R}_N$) states of a system are determined and a series of $N+1$ images are constructed, where the coordinates $[\mathbf{R}_0, \mathbf{R}_1, \ldots \mathbf{R}_{N-1}, \mathbf{R}_N]$ define the images that form the elastic band. Often, an initial guess is to linearly interpolate between the initial and final images which are then connected by elastic bands that have a pre-set spring constant. In this implementation of NEB [68] the tangent, τ_i, to the path at each image, i, is then defined

$$\tau_i = \begin{cases} \tau_i^+ = \mathbf{R}_{i+1} - \mathbf{R}_i & \text{if } V_{i+1} > V_i > V_{i-1} \\ \tau_i^- = \mathbf{R}_i - \mathbf{R}_{i-1} & \text{if } V_{i+1} < V_i < V_{i-1} \end{cases} \tag{2.54}$$

i.e. the estimate of the tangent is only taken between the image, i, and the adjacent image with the highest energy, where V_i is the energy of image i. This is designed to prevent kinks occurring in the MEP. An exception occurs at the minima and maxima of the MEP, as otherwise drastic changes in the tangent happen as the neighbouring images change energies, leading to convergence problems. Instead, in this situation, the tangent is given by a weighted average so that

$$\tau_i = \begin{cases} \tau_i^+ \Delta V_i^{\max} + \tau_i^- \Delta V_i^{\min} & \text{if } V_{i+1} > V_{i-1} \\ \tau_i^+ \Delta V_i^{\min} + \tau_i^- \Delta V_i^{\max} & \text{if } V_{i+1} < V_{i-1} \end{cases} \tag{2.55}$$

where $\Delta V_i^{\max}$ is the maximum and $\Delta V_i^{\min}$ is the minimum of the two expressions $|V_{i+1} - V_i|$ and $|V_{i-1} - V_i|$.

In order to find the MEP the images have to be relaxed. The total force acting on an image is the combination of the spring force acting along the tangent of the MEP ($\mathbf{F}_i^{\text{spring}}|_{||}$), and the actual force of the system acting perpendicular to the tangent ($\mathbf{F}_i^{\text{system}}|_{\perp}$). Thus, the force acting on image i is

$$\mathbf{F}_i = \mathbf{F}_i^{\text{spring}}|_{||} + \mathbf{F}_i^{\text{system}}|_{\perp} \tag{2.56}$$

where

$$\mathbf{F}_i^{\text{spring}}|_{||} = k(|\mathbf{R}_{i+1} - \mathbf{R}_i| - |\mathbf{R}_i - \mathbf{R}_{i-1}|) \cdot \hat{\tau}_i \ , \tag{2.57}$$

and k is the spring constant and $\hat{\tau}_i = \tau_i/|\tau_i|$ is the normalized tangent to the MEP. Trivially, the actual force due to the system environment perpendicular to $\hat{\tau}_i$ is

$$\mathbf{F}_i^{\text{system}}|_{\perp} = \nabla V(\mathbf{R}_i) - [\nabla V(\mathbf{R}_i) \cdot \hat{\tau}_i]\hat{\tau}_i \ . \tag{2.58}$$

The MEP is then found by minimizing the force, $\mathbf{F}_i$, using a standard minimization algorithm for each image. NEB works well, though it does have limitations. It will only find the closest MEP to the initial guess and therefore can over estimate activation energies. It can also under estimate barriers if corners are cut along the MEP. As long as these limitations are considered it is powerful tool for calculating energy barriers for transitions.

2.5 Time Dependent Density Functional Theory

Whilst DFT performs well in determining the ground state properties of a material, in order to model phenomena such as photoabsorption, or other interactions with electromagnetic fields, excited states have to be considered. Time dependent density functional theory (TDDFT) allows calculation of the time dependent Schrodinger equation from an initial known state where the external potential varies with respect to time.

2.5.1 Runge-Gross theorem

TDDFT is justified by the Runge-Gross theorems [69], similar to how the Hohenberg-Kohn theorems [49] underpin DFT. The first theorem states that two external time dependent potentials, $v(\mathbf{r},t)$ and $v'(\mathbf{r},t)$, that differ by more than an additive time dependent function, $c(t)$, so that

$$v(\mathbf{r},t) - v'(\mathbf{r},t) \neq c(t), \tag{2.59}$$

uniquely map to different time dependent densities, $\rho(\mathbf{r},t)$ and $\rho'(\mathbf{r},t)$, that have evolved from the same initial state, $\Psi_0(t=t_0)$. As they both evolve from the same initial state, the potentials must necessarily be equal when $t=t_0$.

The first step of the proof demonstrates that the current densities, $j(\mathbf{r},t)$ and $j'(\mathbf{r},t)$ are uniquely determined by the potentials in equation 2.59. Using the Heisenberg equation of motion

$$i\frac{d}{dt}\langle\Psi(t)|\,\hat{O(t)}\,|\Psi(t)\rangle = \langle\Psi(t)|\,i\frac{d}{dt}\hat{O(t)} + [\hat{O(t)},\hat{H(t)}]\,|\Psi(t)\rangle \tag{2.60}$$

and the definition of the current density

$$j(\mathbf{r},t) = \langle\Psi(t)|\,\hat{j}(\mathbf{r})\,|\Psi(t)\rangle \tag{2.61}$$

$$\hat{j}(\mathbf{r}) = \frac{1}{2i}[\nabla\,|\mathbf{r}\rangle\,\delta(\mathbf{r}-\mathbf{r}')\,\langle\mathbf{r}'| - |\mathbf{r}\rangle\,\delta(\mathbf{r}-\mathbf{r}')\,\langle\mathbf{r}'|\,\nabla] \tag{2.62}$$

and then combining them, it can then be stated that

$$i\frac{\partial}{\partial t}j(\mathbf{r},t) = \langle\Psi(t)|\,[\hat{j}(\mathbf{r}),\hat{H}(t)]\,|\Psi(t)\rangle\ . \tag{2.63}$$

Then, using the condition that both current densities evolve from the same initial state Ψ_0, the evolution of the difference in current densities can be evaluated using equation 2.63 where

$$i\frac{\partial}{\partial t}[j(\mathbf{r},t)-j'(\mathbf{r},t)]|_{t=t_0} = \langle\Psi_0|\,[\hat{j}(\mathbf{r}),\hat{H}(t_0)-\hat{H}'(t_0)]\,|\Psi_0\rangle \tag{2.64}$$

$$= i\rho(\mathbf{r},t_0)\nabla[v(\mathbf{r},t_0)-v'(\mathbf{r},t_0)]\ . \tag{2.65}$$

At this point a further condition is imposed by Runge-Gross, that the external potential can be expanded as a Taylor series about t_0, meaning that, because of equation 2.59, there exists an integer value k whereby

$$\frac{\partial^k}{\partial t^k}[v(\mathbf{r},t)-v'(\mathbf{r},t)]|_{t=t_0} \neq constant, \tag{2.66}$$

and when combined with equation 2.65 it becomes

$$i\frac{\partial^{k+1}}{\partial t^{k+1}}[j(\mathbf{r},t)-j'(\mathbf{r},t)]_{t=t_0} = i\rho(\mathbf{r},t_0)\nabla[\frac{\partial^k}{\partial t^k}[v(\mathbf{r},t_0)-v'(\mathbf{r},t_0)]_{t=t_0}] \neq 0\ . \tag{2.67}$$

This completes the initial proof by showing that the 2 current densities differ immediately as time evolves from t_0. Now all that remains to be shown is that the different densities also digress immediately after the intitial time.

The final step of the proof uses the continuity equation

$$\frac{\partial}{\partial t}\rho(\mathbf{r},t) = -\nabla\cdot j(\mathbf{r},t) \tag{2.68}$$

which when differentiated $k+1$ times with respect to t, and combined with equation 2.67 gives

$$\frac{\partial^{k+2}}{\partial t^{k+2}}[\rho(\mathbf{r},t)-\rho'(\mathbf{r},t)]_{t=t_0} = -\nabla\cdot(\rho(\mathbf{r},t_0)\nabla u_k(\mathbf{r}))\ , \tag{2.69}$$

evaluated at the time $t=t_0$. It can be demonstrated that the densities will differ if the RHS of the equation can be shown to be non-zero. If instead it is asserted that

$$-\nabla\cdot(\rho(\mathbf{r},t_0)\nabla u_k(\mathbf{r})) = 0\ , \tag{2.70}$$

the proof can be completed via reductio ad absurdum. Using equation 2.70 and applying the divergence theorem, specifically one of the Green's identities, generates the expression

$$\iiint_V d\mathbf{r} u_k(\mathbf{r}) \nabla \cdot (\rho(\mathbf{r},t_0) \nabla u_k(\mathbf{r})) = \oint d\mathbf{S} \cdot \rho(\mathbf{r},t_0) u_k(\mathbf{r}) \nabla u_k(\mathbf{r}) \tag{2.71}$$

$$- \iiint_V d\mathbf{r} \rho(\mathbf{r},t_0) |\nabla u_k(\mathbf{r})|^2 \tag{2.72}$$

The surface integral over an infinite surface on the RHS of this equation must be zero as both $u_k(\mathbf{r})$ and $\rho(\mathbf{r},t_0)$ will decay to 0. If the LHS is also zero as asserted in equation 2.70, this would then require $|\nabla u_k(\mathbf{r})|^2 = 0$, which directly contradicts that $u_k(\mathbf{r}) \neq constant$ from equation 2.67. This completes the proof and demonstrates that the densities are uniquely determined by the potential.

2.5.2 Time dependent Kohn-Sham equation

Analagous to the Kohn-Sham equation, a time dependent Kohn-Sham equation can be derived from the action integral as shown in Runge-Gross's original paper [69]. The action integral is given by the expression

$$A[\Psi] = \int_{t_0}^{t_1} dt \, \langle \Psi | \, i \frac{\partial}{\partial t} - \hat{H}(t) \, | \Psi \rangle \ , \tag{2.73}$$

which is stationary when the wavefunction, Ψ, is the solution to the time dependent Schrodinger equation. It can be shown that the action integral is an exact functional of the time dependent density, $A[\rho]$, and so the exact density can be calculated when $\delta A[\rho]/\delta\rho(\mathbf{r},t) = 0$. The functional derivative takes the form of the Euler equation for a set of indepedent particles experiencing an effective potential and so we can calculate the single particle orbitals, $\psi_i(\mathbf{r},t)$, from the time dependent Kohn-Sham equation

$$i\frac{\delta}{\delta t}\psi_i(\mathbf{r},t) = \left(-\frac{1}{2}\nabla^2 + v_{\text{eff}}(\mathbf{r},t,\rho(\mathbf{r},t))\right)\psi_i(\mathbf{r},t) \tag{2.74}$$

where $v_{\text{eff}}(\mathbf{r},t,\rho(\mathbf{r},t))$ is the effective potential given by

$$v_{\text{eff}}(\mathbf{r},t,\rho(\mathbf{r},t)) = v_{\text{ext}}(\mathbf{r},t) + v_{\text{Har}}(\mathbf{r},t) + v_{\text{xc}}(\rho(\mathbf{r},t)) \tag{2.75}$$

where $v_{\text{ext}}(\mathbf{r},t)$ is the external potential which includes the contributions from the ions and the time depednent perturbing field, $v_{\text{Har}}(\mathbf{r},t)$ is the time dependent Hartree potential and $v_{\text{xc}}(\rho(\mathbf{r},t))$ is the time dependent exchange-correlation potential. The time dependent density can then be calculated from the single particle orbitals

$$\rho(\mathbf{r},t) = \sum_{i=1}^{N} |\psi_i(\mathbf{r},t)|^2 \tag{2.76}$$

which can be solved self-consistently.

2.5.3 Linear response TDDFT

Having demonstrated that TDDFT is founded on a solid theoretical base, it is important to extract from it measurable, observable values. Linear response TDDFT (LR-TDDFT) allows the calculation of excitation energies and oscillator strengths for optical transitions in a system, thus allowing comparison with experimentally measured photoabsorption spectra, a common tool for examining defects in solids. The full treatment has been treated in many reviews [70,71], but a brief overview is given here.

The starting point for LR-TDDFT is examining the linear response of the density experiencing a small time dependent perturbation, $\delta v(\mathbf{r},t)$,

$$\rho(\mathbf{r},t) = \rho_0(\mathbf{r}) + \delta\rho(\mathbf{r},t)\ . \tag{2.77}$$

This can then be used to define the density response function

$$\chi(\mathbf{r},t,\mathbf{r}',t') = \frac{\delta\rho(\mathbf{r},t)}{\delta v_{\text{ext}}(\mathbf{r},t)}\bigg|_{t_0} \tag{2.78}$$

which is related to the dynamic polarizability. This is significant as finding the excitation energies of the system experiencing an external field maps onto the problem of finding the poles of the Fourier transform of the density response function, $\chi(\mathbf{r},\mathbf{r}',\omega)$. In the Casida formulation of LR-TDDFT the excitation energies, ω, are the solution to the matrix eigenvalue problem,

$$\begin{bmatrix} \mathbf{A} & \mathbf{B} \\ \mathbf{B}^* & \mathbf{A}^* \end{bmatrix} \begin{bmatrix} \vec{X} \\ \vec{Y} \end{bmatrix} = \omega \begin{bmatrix} 1 & 0 \\ 0 & -1 \end{bmatrix} \begin{bmatrix} \vec{X} \\ \vec{Y} \end{bmatrix} \tag{2.79}$$

where

$$A_{ia\sigma,jb\tau} = \delta_{ij}\delta_{ab}\delta_{\sigma\tau}(\varepsilon_{a\sigma} - \varepsilon_{i\sigma}) + \langle ia|\, f_{\mathrm{Har}} + f_{\mathrm{xc}}^{\sigma\tau}\, |jb\rangle \tag{2.80}$$

$$B_{ia\sigma,jb\tau} = \langle ia|\, f_{\mathrm{Har}} + f_{\mathrm{xc}}^{\sigma\tau}\, |jb\rangle \ . \tag{2.81}$$

Here, $f_{\mathrm{Har}} = 1/|\mathbf{r} - \mathbf{r}'|$ and in the adiabatic approximation

$$f_{\mathrm{xc}}^{\sigma\tau}(\mathbf{r}, \mathbf{r}') = \frac{\delta^2 E_{\mathrm{xc}}[\rho]}{\delta\rho_\sigma(\mathbf{r})\delta\rho_\sigma(\mathbf{r}')} \tag{2.82}$$

where E_{xc} is the exchange correlation functional used in the ground state DFT calculation. This is a common approximation for calculating one-electron transitions of semi-localized states. It is interesting to note that the RHS of equation 2.80 consists of the Kohn-Sham energy eigenvalue differences and a correction due to the electron repulsion and exchange-correlation 2 body terms. Equation 2.79 can be further simplified by implementing the Tamm-Dancoff approximation [72] which sets $\mathbf{B} = 0$, which has the effect of neglecting the contribution of the relaxation of the unnoccupied ground state, which in many systems can be neglected with little loss of accuracy. This means that equation 2.79 becomes

$$\mathbf{A}\vec{X} = \omega\vec{X} \ . \tag{2.83}$$

Not only can the excitation energies, ω be extracted, but the oscillator strengths can also be determined from the eigenvectors $\vec{X}$. This method has been used to calculate the optical absorption spectra of oxygen vacancies in $LaAlO_3$.

Chapter 3

Spectroscopic properties of oxygen vacancies in $LaAlO_3$

3.1 Introduction

Understanding the structural and electronic and properties of point defects in complex oxides, and the mechanisms for controlling their properties, facilitates the development of new functional materials with tuneable performance characteristics. Not surprisingly, this is an area of active experimental, theoretical and computational research [9, 73].

$LaAlO_3$ (LAO) is of interest because its relatively large band gap, reported to be between 5.6 and 6.3 eV [74, 75], may allow oxygen vacancies in several charge states resulting in a range of optical absorption energies. LAO is also used as a substrate for other metal oxide thin films and has potential application as a gate dielectric in complementary metal-oxide-semiconductor (CMOS) devices [76, 77]. Defects in the gate oxide can act as carrier traps and scattering centres and understanding their properties is key to controlling the quality and functionality of these oxides.

The bulk of cubic LAO can be represented as a sequence of positively and negatively charged atomic planes $[LaO]^+$ and $[AlO_2]^-$, respectively, oriented perpendicularly to the [001] direction. Such polar structure makes LAO thin films a functional building block which, for example, can be used as source of electric field in perovskite hetero-structures. A well-known example utilizing this principle is the $LaAlO_3/SrTiO_3$ (LAO/STO) interface, in which mismatch of the $SrTiO_3$ and $LaAlO_3$ polarities results in the formation of two-dimensional electron gas (2DEG) [12]. This phenomenon was originally attributed to the polar catastrophe [8, 9, 13–15] and defects in the STO [21]. Recent studies highlighted the importance of the cation intermixing [10, 11, 16], the LAO stoichiometry [17, 18] and oxygen vacancies (V_O) in LAO on the electronic properties [78] of the LAO/STO interfaces. Zunger et al. [19] suggest that the conductivity is a result of an interplay between surface oxygen vacancies in LAO and cation antisite defects at the interface, whilst Huijben et al. [20] have shown that a layer of $SrCuO_2$ at the LAO/STO interface suppresses oxygen defects and increases mobility, allowing control over the electronic properties through defect engineering.

LAO has a perovskite lattice structure. It has a rhombohedral ($R\bar{3}c$) structure at room temperature and undergoes a phase transition to a cubic ($Pm\bar{3}m$) structure at ~839 K [79, 80]. When grown as a thin supported film, rhombohedral LAO is considered to be pseudocubic [81], with oxygen octahedra rotations in an antiphase order. However, in order to achieve a crystalline, as opposed to amorphous, thin film of LAO, annealing at or above 650°C is required [80, 82, 83], which is above the rhombohedral to cubic phase transition temperature. It is understood that details of the LAO structure in thin films and multi-layered hetero-structures depend on the lattice and polarity mismatch with the substrate and over-layers.

Experimentally, defects in LAO have been probed using photoluminescence (PL) spectroscopy [84, 85] and electron spin resonance (ESR) [43, 86]. Kawabe et al. [84] excited LAO using a 266 nm pulsed laser and observed slow emission at 2.5 eV (490 nm), which they attributed to oxygen vacancies, due to its sensitivity to the oxygen content. In order to more directly probe defect states in the band gap, Chen et al. [85] used sub-bandgap excitation (400 nm) PL spectroscopy. They observed sharp emissions at 1.7 and 1.8 eV and a broad emission band at 1.9-2.2 eV. They suggested that the excitations occur from the O 2p valence band to states within the gap, and therefore PL is a result of decay from these levels. In the ESR experiments [43, 86] a broad signal is attributed to an F^+ like centre, which was cautiously associated with a charged oxygen vacancy ($\mathrm{V_O^{1+}}$). Accurate modeling of the neutral and charged oxygen vacancies in LAO will allow more confident assignment of these transitions and will help to predict their behavior in the presence of external stimuli.

Previous computational studies of defects in LAO include calculations of oxygen vacancies in cubic LAO using density functional theory (DFT) and generalized gradient approximation (GGA) functionals [87, 88] and well as more recent studies [89–91] performed using the hybrid density functional HSE06 [60]. Due to well-known deficiencies of GGA density functionals, the band gap obtained in these studies (3.1-3.8 eV) was underestimated, while the hybrid density functional predicted the band gaps in the interval of 5.0-5.9 eV, which is in a good agreement with experiment, though the higher value of 5.9 eV was only achieved through increasing the percentage of exact exchange to 32% [91].

Predicted positions of the occupied vacancy levels vary significantly, depending on the types of the density functional and the size of the simulation supercell. Choi et al. [91] found the $\mathrm{V_O^0}$ one-electron energy level to lie 3.27 eV above the valence band maximum (VBM), with the occupied $\mathrm{V_O^{1+}}$ level lying lower in energy at 2.96 eV, whereas El-Mellouhi et al. [90] predicted the neutral level to be at 2.8 eV with the $\mathrm{V_O^{1+}}$ level lying higher at 3.56 eV above the VBM. Thus, there is lack of consensus not only on the positions of the energy levels of the neutral and charged oxygen vacancies with respect to the valence band maximum (VBM) and conduction band minimum (CBM) but also on the ordering of these levels.

In this chapter, the electronic and geometric structure of the neutral and charged oxygen vacancies in the band gap of LAO are calculated using DFT with hybrid functionals and periodic and embedded cluster methods. Time dependent density functional theory [69, 70] (TDDFT) and an embedded cluster approach are used to calculate the excitation energies of both neutral and charged oxygen vacancies, improving on the one electron energy levels previously calculated. The ESR parameters are also calculated and compared to the available experimental data. To compare the results presented in this chapter to the previous computational studies, and evaluate the difference between bulk and supported thin-film LAO, calculations were performed for both rhombohedral and cubic lattice structures.

3.2 Methodology

In order to predict experimentally measurable properties of oxygen vacancies, such as the EPR and optical absorption spectra, it is necessary to use more advanced electronic structure methods than DFT which are capable of dealing with excited states. Due to the implementation of TDDFT in the Gaussian09 package [92], an embedded cluster approach was adopted. The embedded cluster calculations were benchmarked against periodic calculations, carried out using CP2K [44]. This section starts with the theoretical background of embedded cluster calculations and its relative advantages and disadvantages when compared to periodic calculations. This is followed by the specifics of the calculation setups.

3.2.1 Embedded cluster method theoretical background

In the embedded cluster method, a ‘region of interest’ treated quantum mechanically (the QM region in Fig. 3.1) is embedded into an electrostatic potential produced by the rest of a lattice, which is composed of pseudopotentials and point charges [93]. The embedded cluster method allows DFT calculations of defects in crystals, including local relaxations, without the issue of image charges that are present in periodic calculations. Also of interest is the well established implementation of TDDFT in finite system quantum chemistry codes, such as Gaussian09 [92], allowing more accurate treatment of electron transitions to excited states. However, in order to accurately model the crystal system, the electrostatic potential of the infinite crystal has to be reproduced at the centre of the finite cluster, the details of which are given in [94, 95] and are breifly outlined here.

First a unit cell has to be selected (which can be a supercell of primitive cells), equivalent to the repeated cell in a periodic system. In order to recreate the crystal potential at the centre of the cluster, which is composed of the unit cells, point charges are positioned at lattice positions, defined by the lattice vectors of the crys-

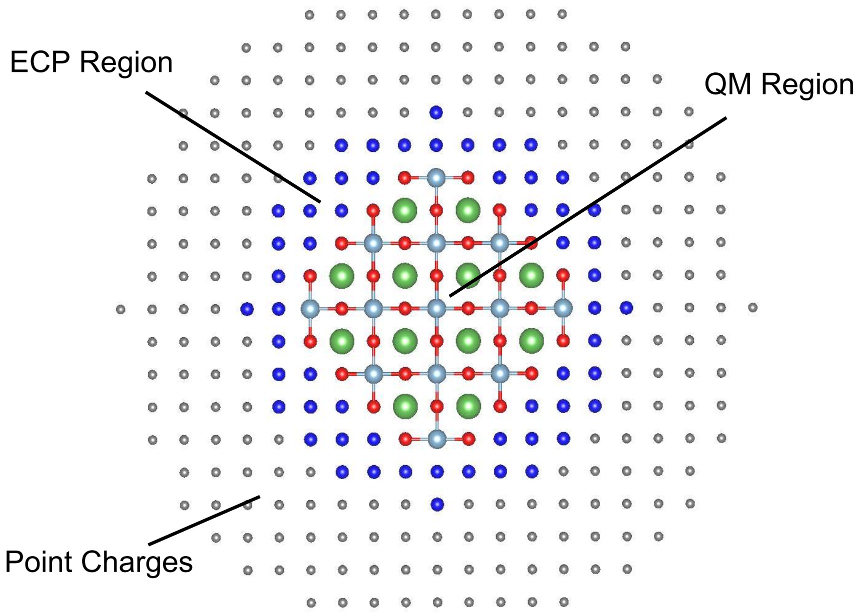

Figure 3.1: Schematic setup for the embedded cluster calculations. The central region is treated quantum mechanically (QM region shown is a cross section of that used in the calculations). It is embedded into the long-range electrostatic potential of the infinite lattice, represented by a finite number of point charges, and the short-range potential modeled using large radius effective core pseudopotentials (ECPs) at the interface between the QM region and the point charges.

tal, so as to minimize the multipole moments of the system. By eliminating multipole moments, up to some multipole M, the Ewald potential at the centre of the cluster converges to the Ewald potential of the infinite lattice, as the system size increases.

Although the ability to perform TDDFT calculations was the primary reason for using an embedded cluster approach, it also has some advantages over periodic codes when calculating defects. The embedded cluster method eliminates interactions between charged defects and prevents ion relaxations being confined by symmetry, which occurs in calculations with periodic boundary conditions. However, the number of ions able to be relaxed is still limited by considerations of computational time and the size of the quantum region, and the formation energy of charged defects still requires a correction due to lattice polarization (see section 2.3).

Here a rigid ion model has been adopted, where ions outside of the quantum mechanical region and pseudopotential region are not allowed to relax, and are treated as point particles in order to produce the embedding potential. QM/MM embedding models define a second region surrounding the quantum region where ions are treated using classical potentials, which goes some way to correcting for the polarization energy of the surrounding lattice when a charged defect is introduced. Use of a rigid ion model for all ions has been shown to affect the calculated optical absorption energies when compared to treating the polarization via relaxation of the ions [96], though in [96] a smaller quantum region was used, and optical transition energies were approximated by one electron energy levels. In this work use of the rigid ion model outside the quantum region was seen as sufficient, as predicting the optical absorption spectra relies more on calculating accurate electronic structure, with less interest in the formation energies of oxygen vacancies. Instead it was found that the use of larger quantum regions was required to prevent confinement of the wavefunction widening the Kohn-Sham energy levels and leading to spurious energies for the optical transitions, though it also allows a greater region of polarization response. The stability of the calculated band gap energies (the difference in energies between the valence and conduction band Kohn-Sham energy levels) between systems of differently charged oxygen vacancies, which deviate by less than 0.05 eV, suggests that the use of a rigid ion model will not greatly affect the optical absorption energies. The comparison with the relative Kohn-Sham levels of the neutral and charged oxygen vacancies calculated using a periodic model also demonstrates good agreement with the embedded cluster model, showing the approximation is reasonable.

3.2.2 Embedded cluster method calculation setup

Here, the bulk LAO was represented using a spherical nano-scale cluster constructed of the crystal unit cells. Each unit cell was modified so that their multipole moments, M, were zero up to M=4 (hexadecapole), as described above [94, 95]. This approach guarantees that the electrostatic potential inside a finite nano-scale cluster converges absolutely to the Ewald potential in the infinite crystalline lattice as the size of the cluster increases. In this work, the nano-cluster radius was chosen to be 30 Å, which provides the convergence of the electrostatic potential to within

0.02 V of the Ewald potential inside the sphere of 11 Å in the central part of the nano-cluster.

The QM region at the center of the nano-cluster contains 197 atoms and has the chemical composition $La_{32}Al_{33}O_{132}$. The QM region is chosen so that it is symmetrical, as close to stoichiometry as possible whilst still fully coordinating all lattice atoms in the 1st and 2nd atomic shells near the vacancy site and large enough to minimize wavefunction confinement, which noticeably affects the value of the band gap for small QM regions. In order to confine the electron density to the QM region all cations also have to be capped with oxygens. Although it is desirable to build as small a quantum region as possible in order to reduce calculation time, when smaller cells were tested confinement of the wavefunction increased the size of the band gap by approximately 2 eV above the experimental band gap. Smaller quantum regions also decreased the number of atoms able to relax after the addition of defects to the system, leading to unrealistic relaxation energies and polarization of the system.

The QM region is surrounded by the shell of the interface atoms represented by large core effective pseudo-potentials (ECP) in order to confine the electron density within the QM region (see Fig. 3.1). The width of this shell is $\sim$10 Å, which allows one to use diffuse basis set functions for the atoms of the QM cluster and, yet, avoid spurious effects associated with electron transfer outside the QM region. All other atoms of the nano-cluster are represented by point charges.

All oxygens species in the QM region are treated using the full electron 6-311G basis set [97] as are the Al [98]. The La inside the QM region were described by a contracted version of the LANL08 basis set [99] and the LANL2DZ ECP [100] from the EMSL basis set exchange [101].

Outside the QM region, the La and Al ions were described by ECPs, as they both have a formal charge of +3 $|e|$ and, thus, require ECPs in order to prevent the artificial polarisation of the QM region electron density. The Al ions are modeled using the LANL2 ECP [100], and the La ions are modeled using the LANL2DZ ECP [100] from the ESML basis set exchange [101].

The geometrical structure of the material in the electronic ground state was determined by minimizing the total energy of the system with respect to the coordinates of atoms out to 5.72 $\AA$ from the central Al in the cluster. This allows all nearest neighbour La, Al and O to the vacancy site to relax. TDDFT calculations and the Frank-Condon approximation were used to calculated the excitation energies and relative intensities. All calculations were carried out using the Gaussian09 package [92].

For all calculations using the embedded cluster method the HSE06 [102] functional was used, which was shown to accurately predict the band gap and, as such, allow comparison with previous results. The self-consistent field (SCF) convergence criterion is set to an energy difference of 10^{-7} Hartree. For the geometrical relaxations the convergence criterion is set to a force of 1.7×10^{-3} Hartree/Bohr on the atoms being relaxed.

3.2.3 Periodic calculations

The bulk properties of the cubic and rhombohedral LAO were calculated in the Γ-point using the 135 and 270 atoms super cells, respectively, and the CP2K [44] package. The PBE0-TC-LRC [40] functional (see section 2.2.5) was used, with a cutoff radius of 5.5 Å, due to the computational expense of running calculations using HSE06 [102] on the larger rhombohedral system. The form of truncation used means that the calculations ran faster in CP2K using PBE0-TC-LRC than HSE06. However, the energy level ordering and molecular orbitals agreed well with calculations performed using the HSE06 functional for the cubic system, and the 2 functionals are similar in form. The DZVP-MOLOPT-SR-GTH [103] basis sets were used for both O and Al, along with the Goedecker-Teter-Hutter (GTH) pseudopotentials [55,56]. The converged plane wave energy cutoff was set to 400 Ry and the SCF convergence criteria was set to a maximum energy difference of 10^{-6} Hartree between steps. All calculations were performed at the Γ-point. All geometry relaxations were performed using the conjugate gradient optimizer with a maximum force convergence criterion of 0.001 Hartree/Bohr for each atom.

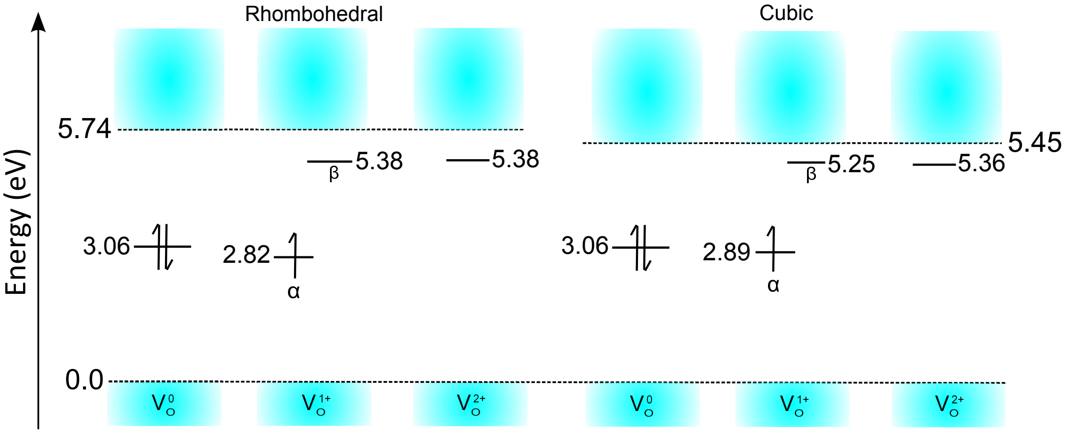

Figure 3.2: The one electron energy levels for the neutral and charged oxygen vacancies from the periodic calculations of the rhombohedral and cubic phases. The numbers show the positions of the Kohn-Sham energy levels calculated with respect to the top of the valence band for each system, which have been aligned at 0.0 eV. The band gaps shown in larger font are from the defect free calculations. The α and β symbols refer to the electron spin state of the V_O^{1+}, in this diagram the α state in the gap is occupied while the β is unoccupied.

3.3 Results and discussion

3.3.1 Ground state calculations

3.3.1.1 The perfect lattice

Cell optimizations of the perfect lattice for the cubic phase were performed using PBE0-TC-LRC. The calculated lattice parameter of $a = 3.79$ $\AA$ agrees well with the experimental lattice parameter of $a = 3.8108$ $\AA$ [79], measured at 830 K after its transition from the rhombohedral phase. Due to the computational expense of performing cell optimizations on larger systems using hybrid functionals, the experimental lattice parameters were used for the larger rhombohedral supercell.

The one electron band gaps calculated using both the periodic and embedded cluster methods are shown in Fig. 3.2 and Fig. 3.3. The optical band gap of rhombohedral LAO is 5.6 eV, as measured by Lim et al. [74] using UV spectroscopic ellipsometry. The reported absorption spectra show a sharp absorption edge, as expected for a direct band gap material and no sharp peaks associated with d-state to d-state transitions were observed, suggesting that the VBM is composed of O $2p$ orbitals. The band gaps of amorphous thin films of LAO grown by molecular beam

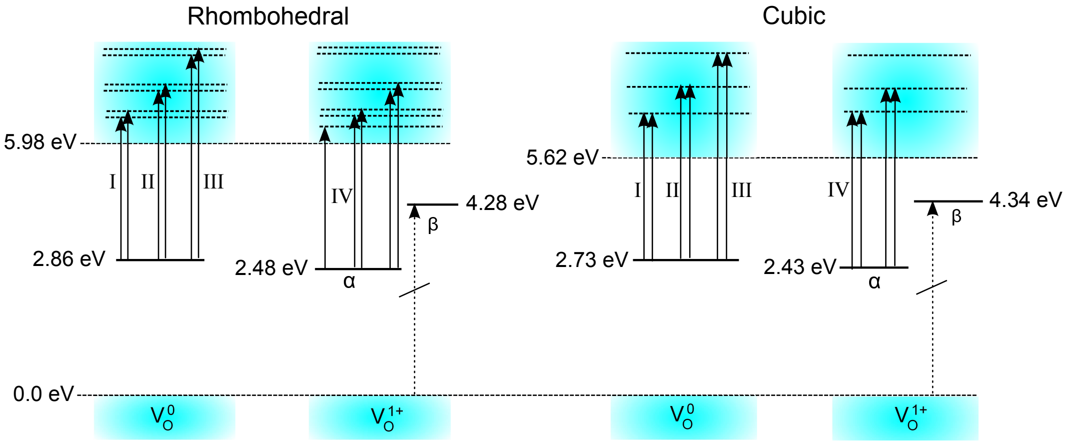

Figure 3.3: The one electron energy levels and band gaps from the embedded cluster calculations for the cubic and rhombohedral LAO phases (energies not to scale). Arrows show the optical transitions, labeled using Roman numerals and further described in the text. The α and β symbols refer to the electron spin state, in this diagram the α state in the gap is occupied while the β is unoccupied.

deposition (MBD) have been measured by Cicerella et al. [75] to be 5.84–6.33 eV depending on film thickness. It is possible that these films have a pseudo-cubic crystalline structure as they were annealed at 900°C, i.e., well above the 650°C, which other groups have determined is necessary for amorphous films to become crystalline [80, 82, 83].

The calculated one electron band gaps of rhombohedral LAO (5.74 and 5.98 eV for the periodic and embedded cluster calculations, respectively) are both within the range set by the experimental measurements, and only differ by ∼0.2 eV showing good agreement between these methodologies. As can be seen in Fig. 3.4, the main orbital contributions to the VBM and CBM are consistent with experiment [74] with the VBM being constructed from O $2p$ orbitals and the CBM being made of La d orbitals. This was found to be the case for both the periodic and embedded cluster calculations.

The band gap of the cubic LAO (5.45 and 5.62 eV for the periodic and embedded cluster calculations, respectively) is smaller than that of the rhombohedral LAO by ∼0.3 eV, consistent across both the periodic and embedded cluster calculations. The band gap values are close to those of Choi et al. [91], who predict 5.92 eV for the rhombohedral and 5.30 eV for the cubic phases. Choi et al. also show a similar

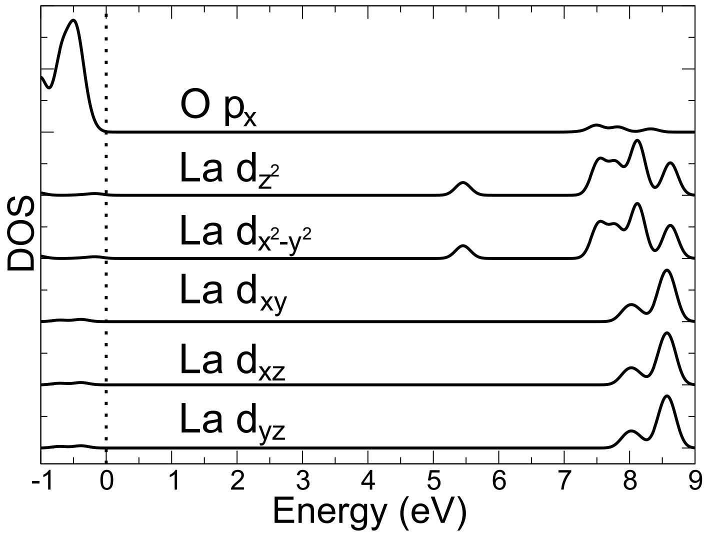

Figure 3.4: The projected densities of states (PDOS) for the defect free bulk system of cubic LAO calculated using the periodic method. The character of the VBM is dominated by the O p and the CBM by the La d orbitals. The energies are with respect to the top of the valence band. The black dashed line indicates the Fermi energy position at the top of the valence band.

band gap shift relationship between cubic and rhombohedral structures to the results given in this paper.

3.3.1.2 The oxygen vacancy

According to these calculations the two electrons associated with a neutral oxygen vacancy in LAO, both cubic and rhombohedral, localize on the vacancy site (see Fig. 3.5a). The corresponding doubly occupied energy level lies approximately in the middle of the band gap. This localization character suggests that the vacancy can be classified as an F-center. Similar charge localization is seen in other non-reduceable metal oxides including Al_2O_3 and other perovskites [104]. The largest atomic orbital contributions to the vacancy state are from the nearest neighbor Al p orbitals, the lobes of which point towards the vacancy, with the second largest contribution being from the nearest neighbor La d orbitals.

The formation energies of the neutral and charged oxygen vacancies were calculated using the method outlined in section 2.3, using both periodic and embedded

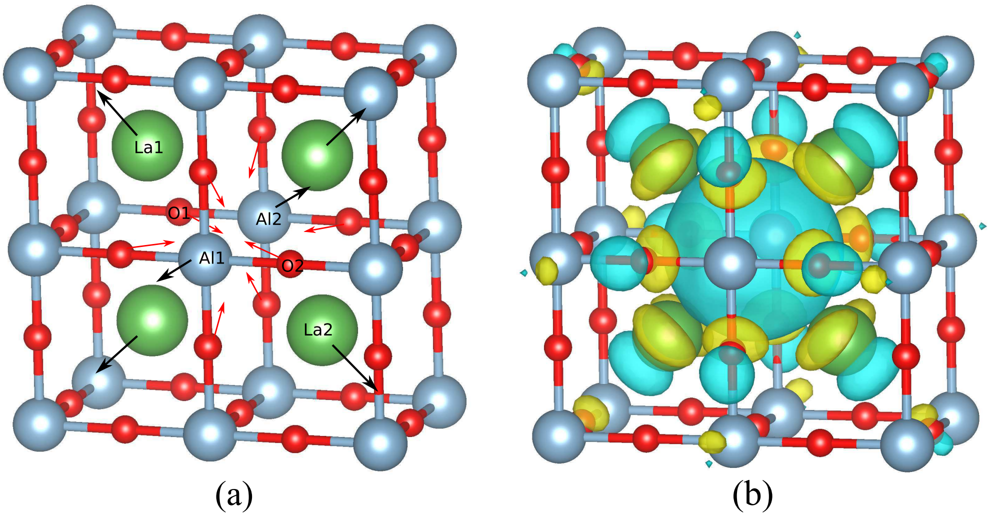

Figure 3.5: (a) The directions of the ion displacements induced by a positively charged vacancy are shown by the arrows. The La1–La2, Al1–Al2, and O1–O2 distances are given as La–La, Al–Al, and O–O distances, respectively, in Table 3.1. (b) The one-electron state of the neutral oxygen vacancy calculated using the periodic method in cubic LAO. Characteristically of a F-center vacancy type, electrons are trapped on the vacancy site.

cluster methods, though the charge correction term does not apply to the embedded cluster calculations. The chemical potential of oxygen was taken as half of the total energy of the O_2 molecule in the triplet state. For the embedded cluster calculations, the total energy of an isolated O_2 molecule was calculated using Gaussian09 and the same oxygen basis sets, functional, and convergence criteria as for the LAO cluster. In the periodic method calculations, the energy of the molecule was calculated using an orthorhombic $20 \times 22 \times 25$ Å^3 cell, with the same calculations parameters as those used for the bulk LAO. Due to the large size of the cell and the high dielectric constant of LAO the energy correction due to the interaction between periodically translated charged defects is negligible (<0.1 eV).

For rhombohedral LAO, the V_O^0 formation energy was calculated to be 6.5 eV from the periodic calculations and 7.2 eV from the cluster calculations. The difference of 0.7 eV between the formation energies calculated by the two methods is largely due to the difference in the oxygen chemical potential reference energy. As stated earlier, the oxygen chemical potential is taken as half the energy of an O_2 molecule, which is used to model the typical oxygen environment of LAO during growth. However, the binding energy of the molecule is different in the two methods. If instead, the energy of a single atomic oxygen is taken as the chemical potential, the difference in formation energies between the 2 methods drops to 0.3 eV. In the end, the oxygen chemical potential of half an O_2 molecule is chosen so as to make comparisons with previous studies.

The values for the V_O^0 formation energies in rhombohedral LAO presented here are lower than the formation energy of 8.3 eV reported by Mitra et al. [89]. The referenced calculations were performed using the HSE06 functional, however, only an 80 atom supercell was used, which would limit the relaxation around the defect site compared to the larger cell of 270 atoms used in this work. In the same paper, using the PBE functional, it is shown that supercell size has a large impact on formation energies, even for neutral vacancies. This suggests the formation energies calculated for the larger cells are more reliable. The formation energies of the oxygen vacancies as a function of Fermi energy are shown in Fig. 3.6. (It must be clarified that this picture is only valid when the LAO bulk is attached to an idealized Fermi sea of electrons, generally provided by a metal or semiconductor electrode.) Even so, it can be seen that thermodynamically either V_O^0 or V_O^{2+} are the most stable defects at various Fermi energies within the band gap, with V_O^{2+} having the lowest formation energy if the Fermi level is near the top of the valence band. If the Fermi level exceeds 3.6 eV above the VBM, V_O^0 has the lowest formation energy.

This is relevant to the LAO/Si transistor devices, where valence band offsets of 2.86 eV have been measured using x-ray photoelectron spectroscopy [77], suggesting that charged oxygen vacancies will form upon contact with undoped silicon. In turn, if the Si channel is n-doped, i.e., the Fermi level is 3.8 eV or more above the LAO VBM, the vacancies can trap electrons, which would affect device operation.

The direction of vacancy-induced atomic displacements (see Fig. 3.5) are as expected for the ionic system, and the magnitudes of these displacements are in good agreement between the cluster and periodic calculations. The small displacements of ions around the neutral vacancy are consistent with those reported earlier for LAO [91] and is consistent with calculations of similar perovskites such as

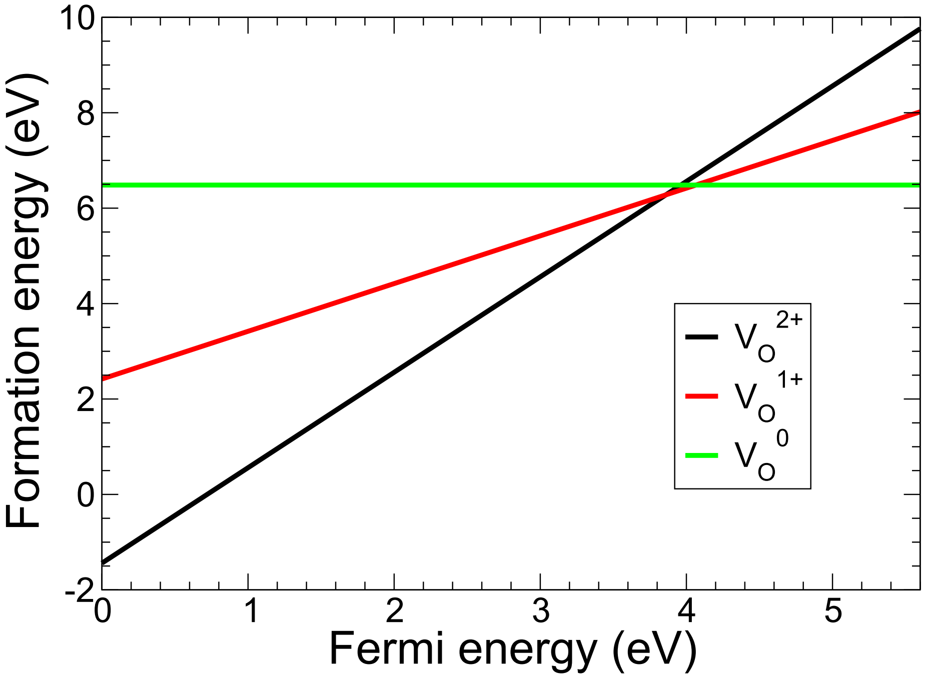

Figure 3.6: Formation energies of V_O^0, V_O^{1+}, V_O^{2+} as a functions of Fermi energy above the VBM for the periodic method calculations of rhombohedral LAO.

SrTiO$_3$ [105]. The larger displacements, especially those of the Al species, induced by the positively charged vacancies, are consistent with other DFT studies of oxygen vacancies in LAO [91]. This also explains the higher formation energies reported by Mitra et al. [89]: in a smaller supercell lattice relaxation is constrained by the periodic boundary conditions and the final energy of the system is correspondingly higher.

Both the periodic and cluster methods (see Fig.3.2 and Fig.3.3) agree on the ordering of the one electron energy levels, with the V_O^{1+} level lying below the V_O^0 level and the unoccupied V_O^{2+} level lying the closest to the CBM. These results are consistent with those reported by Choi et al. [91], but disagree with those published by Mitra et al. [89] who calculate the V_O^{1+} level to lie 1.34 eV above that of the V_O^0. This difference could be attributed to a smaller super cell used in Ref. [89] (an 80 atom supercell) meaning stronger defect-defect interactions for the charged vacancies. In all calculations reported in this chapter, the one-electron band gap

Table 3.1: Interatomic distances (in Å) and magnitude of vacancy-induced displacements (as % change in interatomic distance from bulk) in LAO. Negative and positive values of the displacements indicate relaxation towards and away from the vacancy site, respectively. A diagram defining the nearest neighbor distances is shown in Fig.3.5a.

			Embedded cluster		Periodic	
			$Pm\bar{3}m$	$R\bar{3}c$	$Pm\bar{3}m$	$R\bar{3}c$
Inter-atomic nearest neighbor distances (Å)		Al-Al	3.82	3.79	3.79	3.79
		La-La	5.42	5.38	5.36	5.36
		O-O	5.40	5.35-5.37	5.36	5.36
Maximum displacements from perfect lattice (%)	V_O^0	Al-Al	-2.5	-2.0	0.2	-0.0
		La-La	0.7	0.2	-0.2	-0.8
		O-O	-0.8	-0.7	-0.2	-0.9
	V_O^{1+}	Al-Al	2.7	2.8	4.5	5.4
		La-La	2.8	2.4	1.9	1.7
		O-O	-2.7	-2.3	-2.6	-2.8
	V_O^{2+}	Al-Al	7.9	7.4	8.0	9.5
		La-La	4.3	4.5	4.2	4.2
		O-O	-6.0	-6.5	-6.1	-6.2

does not change with respect to the charge of the defect by more than 0.05 eV as a result of large enough cluster and cell sizes to mitigate confinement and defect-defect interactions.

The possibility of a stable V_O^{1-} state existing in LAO was also investigated. The extra electron was not found to localize at the vacancy site but, instead, occupied delocalized states at the bottom of the conduction band. For comparison, V_O^{1-} and V_O^{2-} were shown to exist in HfO_2, which has band gap and dielectric constant similar to those of LAO [106]. These vacancy charge states are stabilized by displacements of Hf ions near the vacancy site by 4% and 8% of bulk separation distance, for V_O^{1-} and V_O^{2-}, respectively. The polarization of the lattice creates a potential well for the electrons, i.e., these localized states are polaronic in nature.

In order to rationalise this difference between HfO_2 and $LaAlO_3$, the following can be considered. In HfO_2, the oxygen vacancy is surrounded by four Hf^{4+} ions. The electrons in the negatively charged vacancy can be attributed to the Hf atomic *d*-orbitals, which contribute to the bottom of the conduction band but, due to the vacancy-induced atom displacements, form localized gap states. Similarly, in $LaAlO_3$, the La *d* orbitals form the bottom of the conduction band. However, their displacements pattern near an oxygen vacancy is very different from that of Hf in HfO_2. In particular, each Hf^{4+} in HfO_2 is coordinated by eight O^{2-} ions, which can be considered as vertices of a distorted cube; in fact, HfO_2 adopts a monoclinic structure at low temperatures. Once an oxygen vacancy is formed, the Hf coordination number reduces to seven and an already low-symmetry potential energy surface becomes even more distorted, which makes large displacements of Hf atoms possible. This effect is assisted by the fact that formation of an oxygen vacancy in HfO_2, as well as in ZrO_2, induces a significant charge redistribution at the vacancy site [107, 108].

In contrast, the La^{3+} ion in LAO is confined by 12 O^{2-} ions and eight Al^{3+} ions, which create a symmetric, compact and rigid coordination shell. Formation of a neutral vacancy does not change the character of the charge distribution and, while it affects the symmetry and rigidity of the La environment, the effect is not strong enough to promote significant displacements of La^{3+} from its ideal lattice site. Hence, the perturbation exerted on the electronic states at the bottom of the conduction band is not significant enough to induce localization of these states at the vacancy site and subsequent formation of V_O^{1-}.

3.3.2 Defect properties

3.3.2.1 Optical absorption spectra

Optical absorption spectra for V_O^0 and V_O^{1+} have been calculated using the embedded cluster method and TDDFT, as implemented in Gaussian 09 [92]. The natures of the transition states and the orbitals have also been identified. The relative intensities of the peaks are determined by the oscillator strengths of the transitions, the lines are then broadened using a Gaussian function with a full width at half maxima of 0.2 eV. TDDFT calculations of transitions in the V_O^{2+} case did not demonstrate any sub-band-gap excitations with non-zero oscillator strengths, and as such absorption spectra are not shown.

The vacancies do not perturb the valence band states as strongly as they do the conduction band states. Hence, the VBM states remain delocalized and the

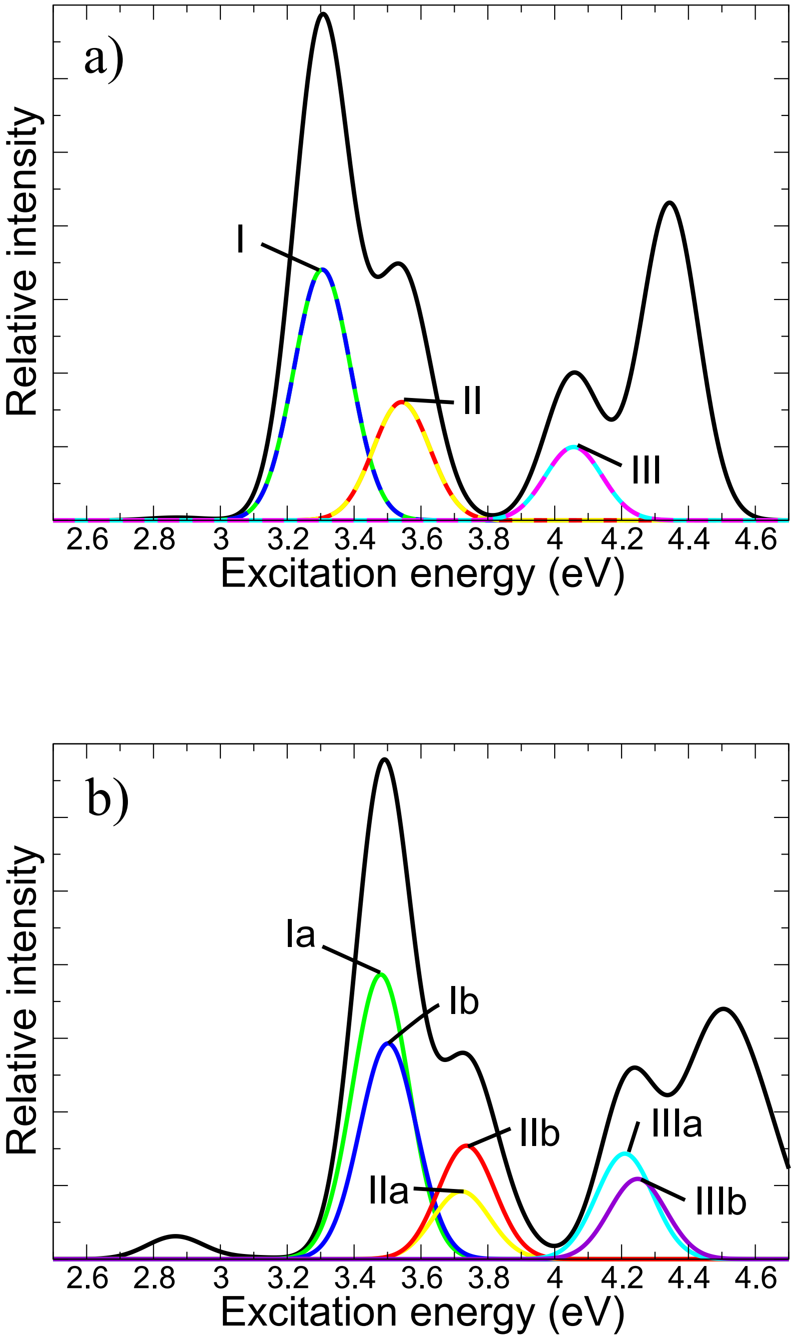

Figure 3.7: The calculated absorption spectra for V_O^0 in the cubic (a) and rhombohedral (b) phases. The transitions have been broadened using Gaussian functions with a FWHM of 0.2 eV. The black lines show the total spectra, while the colored lines show the contributions due to the individual transition types. Dashed lines are used for visibility of degenerate transitions. All labels are defined in Fig. 3.3. The label I refers to the first, or lowest energy transition in the cubic system, Ia and Ib refer to the 2 lowest energy transitions of the rhombohedral system, which unlike the cubic system are non-degenerate. This is repeated for the 2nd (II) and 3rd (III) transitions.

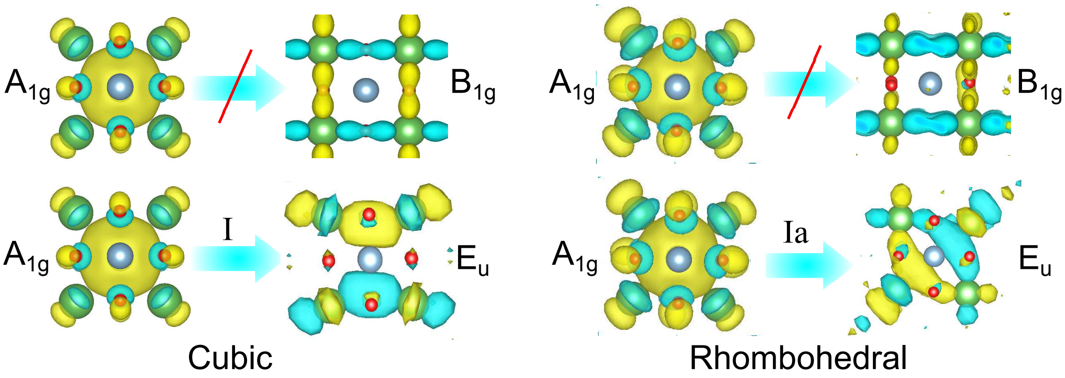

Figure 3.8: The molecular orbitals involved in optical transitions from the vacancy state to states in the conduction band of cubic (left) and rhombohedral (right) LAO. The same molecular orbital of the vacancy can be seen in Fig. 3.5b, here the vacancy lies behind the Al as viewed along the 001 crystal axis. The D_{4h} point symmetry of the defect can clearly be seen. The symmetry forbidden transitions (top) are to unperturbed e_g states at the bottom of the conduction band. The highest intensity transitions (bottom), I for cubic and Ia for rhombohedral, are allowed dipole transitions from an A_{1g} to an E_u state.

transitions between them and the localized vacancy states have low intensities. It is also evident that the transitions from the O p-orbitals at the top of the valence band to the vacancy state are prohibited by symmetry considerations.

The optical absorption spectra calculated for the neutral oxygen vacancies in the cubic and rhombohedral phases are shown in Fig. 3.7. Each spectrum is composed of several absorption peaks corresponding to transitions from the doubly occupied vacancy state (shown in Fig. 3.5b) to semi-localized states in the conduction band consisting primarily of La d orbitals. The spectrum for the rhombohedral lattice has a larger number of non-degenerate excited states, as expected for the lower-symmetry system. This spectrum is also shifted to the higher absorption energies by $\sim$0.2 eV. This shift can be attributed to the increased splitting of the e_g and t_{2g} manifold of the La d-states caused by the lattice distortions, which shifts the e_g states, forming the bottom of the conduction band, up and increases the band gap (see Figs. 3.3 and 3.4). In order to ensure that the composition of the molecular orbitals obtained in the cluster calculations is not affected by the finite size of the quantum region, they were compared to the molecular orbitals obtained in the periodic method calculations and were found to be in good agreement.

As discussed above, the projected density of states (PDOS) of bulk LAO, calculated using the periodic method, shows that the bottom of the conduction band of cubic LAO is composed of e_g states, with equal contributions from the d_{z^2} and $d_{x^2-y^2}$ atomic orbitals, which are degenerate (see Fig. 3.4). The t_{2g} states are $\sim$2.5 eV higher in energy than the e_g states. This is consistent with the crystal field splitting for a 12-coordinated La site, where the 12 nearest neighbor O^{2-} ions are located along the t_{2g} lobes. The bottom of the conduction band of rhombohedral LAO is also composed of e_g-like states, though in this case the e_g-like states lie 0.2 eV higher in energy and there is a small splitting between the d_{z^2} and $d_{x^2-y^2}$ atomic orbitals. This is due to the difference in crystal field: the rhombohedral system can be produced by a slight distortion of the cubic lattice along with rotations of the oxygen octahedra. There is still a significant splitting between the e_g and t_{2g} states as the local environment of the La ions is similar between the cubic and rhombohedral cases. The rotation of the oxygen octahedra has a larger effect on the energies of the t_{2g} states, as the lobes of these orbitals no longer point directly towards the O sites, which causes the energies of the d_{xy}, d_{xz} and d_{yz} orbitals to split.

The inclusion of the neutral vacancy perturbs certain states within the conduction band and, though the e_g-t_{2g} splitting remains dominant, there is some mixing of the states. In the cubic system, a contribution from the d_{xy} orbital to some states at the bottom of the conduction band ($\sim$7.2 eV) is observed. These states are localised in the vicinity of the vacancy, as shown in Fig. 3.8. The point symmetry of the defect is D_{4h}, with the irreducible symmetry of the vacancy state orbital being A_{1g} in character. This means the only symmetry allowed dipole transitions are to states with an irreducible representation of E_u or A_{2u}. Where the perturbation of the states in the conduction band are small, the molecular orbitals display gerade symmetry (see Fig. 3.8) and transitions are forbidden to these levels, resulting in the gaps in the absorption spectra.

The lowest energy absorption peak at 3.3 eV (transition I) in the cubic phase consists of two transitions to states where the majority of the wavefunction is composed of the d orbitals of the nearest neighbor La ions to the vacancy (see Fig. 3.8).

These orbitals display E_u symmetry and are therefore dipole operator allowed transitions. The second peak (transition II) with excitation energies of 3.5 eV involves states with a significantly smaller contribution from the d_{xy} orbital and are subsequently lower in intensity. The third set of peaks (transition III) with the onset at 4.06 eV involve more delocalized states with stronger contributions from the next nearest neighbor La ions.

In rhombohedral LAO, due to the lower symmetry of the defect site, the transition of type I splits into types Ia and Ib, as the unoccupied one-electron states involved in these transitions are no longer degenerate. However, as the perturbation to the local environment of the vacancy is small, the overall character of the absorption spectra remains the same, with the addition of some low intensity transitions to states that are no longer strictly symmetry forbidden. The same applies to the transitions of types II and III. The increased splitting of the individual t_{2g} states (d_{xy}, d_{xz} and d_{yz}) can be seen by the increased splitting of the transitions II and III compared to I.

The main absorption peak of the rhombohedral LAO at 3.5 eV (the peak extends from 3.2-4.0 eV) agrees well with the results of Kawabe et al. [84] who observe an absorption peak at 3.5-4.1 eV that is suppressed after oxidation of the sample, which they suggest is due to oxygen deficiency.

The absorption spectra for $\mathrm{V_O^{1+}}$ differ from those of the neutral vacancy. In particular, they exhibit a single large peak and no significant second peak at higher energy (see Fig. 3.9). Similarly to the case of the neutral vacancy, the energy of the maximum of the absorption peak obtained for the rhombohedral lattice is ~0.2 eV higher than that for the cubic lattice. The transitions from the valence band to the unoccupied $\mathrm{V_O^{1+}}$ level in the band gap are calculated to have a negligible oscillator strength, as such only transitions from the occupied vacancy level to the conduction band can be seen in the absorption spectra. This is most likely because, like in the $\mathrm{V_O^{2+}}$ case, the O p states that compose the valence band are not significantly perturbed by the defect to create resonant states with appropriate symmetry. The states involved in transition IV (see Fig. 3.9) are similar to those involved in transition I

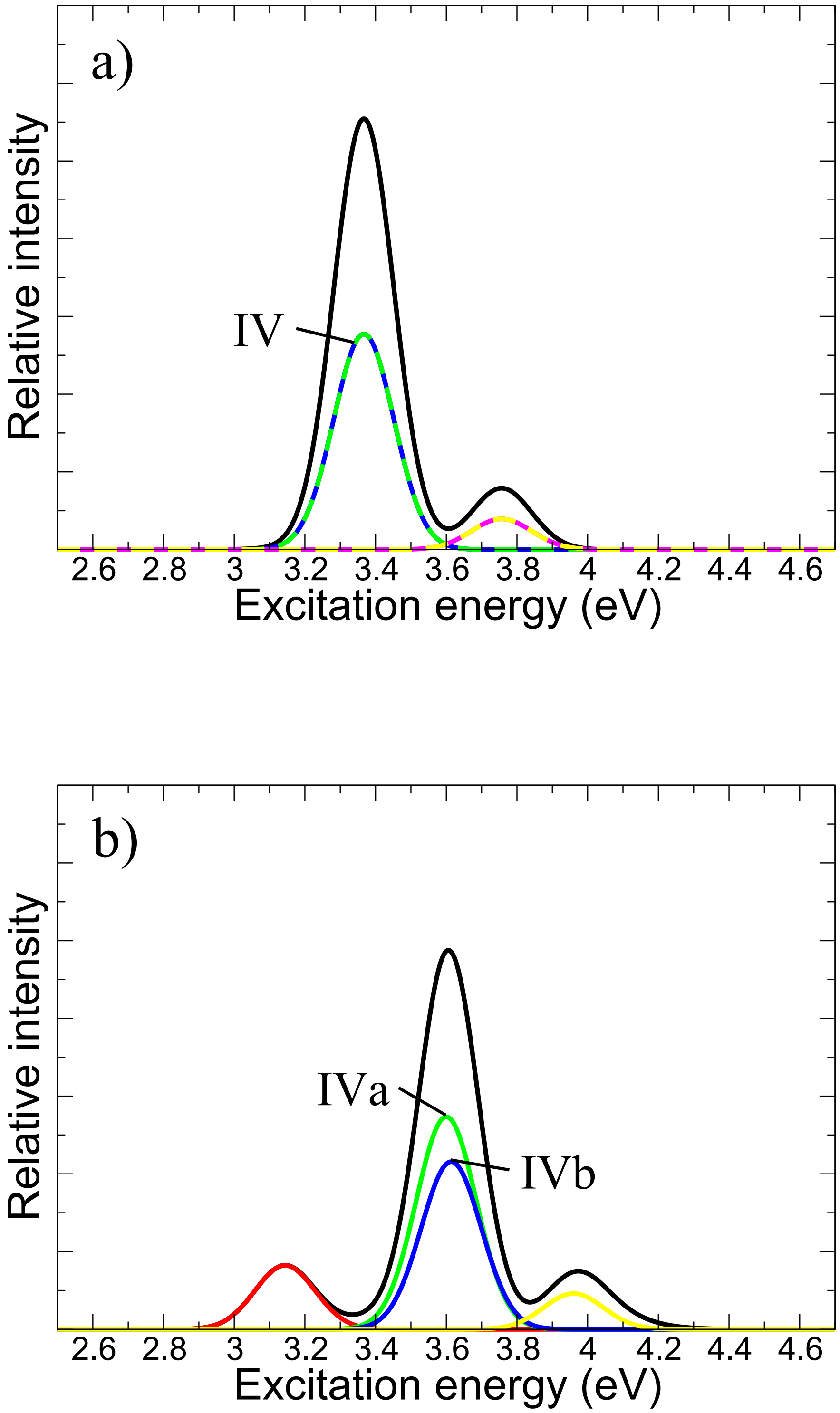

Figure 3.9: The TDDFT calculated absorption spectra for V_O^{1+} in both the (a) cubic and (b) rhombohedral phases. The transitions have been widened using Gaussian functions with a FWHM of 0.2 eV.

Table 3.2: The calculated g-tensor values of V_O^{1+} for both the cubic and rhombohedral LAO structures. The Al^{3+}–V_O^{1+}–Al^{3+} complex is oriented along the x axis of the cubic cell.

Calculated g-tensor			
	g_{xx}	g_{yy}	g_{zz}
$Pm\bar{3}m$	1.999338	2.005083	2.005083
$R\bar{3}c$	2.004025	2.000608	2.003056

in the neutral case. This is expected as the V_O^{1+} defect shares the same point symmetry as V_O^0. The rhombohedral system demonstrates a non-zero transition below transition IV not seen in the cubic case. In the rhombohedral case there is weak localization of the molecular orbital composed of a mixing of the t_{2g} states with the predominantly e_g states at the bottom of the conduction band. In the cubic case both of these orbitals are delocalized pure e_g states and so there are no transitions to these states.

3.3.2.2 The g-tensor and hyperfine splittings of V_O^{1+}

Electron spin resonance (ESR) studies can allow measurements of the V_O^{1+} defect in LAO. Indeed, ESR studies of LAO [43,86] have attributed certain signals in their measured spectra to this defect. In order to confirm the prediction that these signals are due to the V_O^{1+} defect the g-tensor and hyperfine values of the defect can be calculated and compared to the experimental values.

The g-tensor components for the +1 charged oxygen vacancy, calculated using Gaussian 09 [92] and the embedded cluster method, are shown in Table 3.2. The calculated hyperfine splittings show the main contribution to the ESR signal comes from the nearest neighbor Al ions. This is most likely because the defect orbital is mainly composed of the p orbitals of these Al ions. The calculated value of the splitting is small at 0.53-0.69 mT, dependent on the local structure. The contributions of the nearest-neighbor O ions are smaller at approximately 0.1 mT and only apply if grown in ^{18}O as naturally abundant ^{16}O has zero nuclear spin. The contributions of even the nearest neighbor La are negligible.

The calculated g values agree closely with the ESR results of Yamasaka et al. [43] and Singh et al. [86]. The former work assigns a broad ESR signal at approximately 328 mT to the +1 charged oxygen vacancy in LAO. Using their reported X-band frequency of 9.2 GHz, the corresponding g value can be calculated to be 2.004022, which is in good agreement with the calculated values. The width of the signal reported by Yamasaka et al. [43] is approximately 4.0 mT, which can be explained by the calculated hyperfine splittings. Al has a nuclear spin of $5/3$, which means the hyperfine interaction leads to 6 peaks split by approximately 0.6 mT, this would lead to a total broadening of at least 3.0 mT, assuming that the broadening of each line was large enough that the individual lines could not be resolved. This also agrees well with the results of Singh et al. [86] who measured the line width of the $\mathrm{V}_{\mathrm{O}}^{1+}$ signal to be 2.9 mT. They also suggest hyperfine interaction with the nearest neighbor cations are the main contribution to the linewidth, in agreement with the calculations presented here.

Also of interest are the absorption spectra measured by Yamasaka et al. [43]. The ESR signal for the charged vacancy only appears as the number of incident photons (with photon energy peak at 5.03 eV) increases on the LAO sample while it is under UV irradiation. This corresponds to an increase in the absorption coefficient at approximately 3.3 eV and 4.0 eV. These energies lie close to the transition energies for the neutral and charged oxygen vacancies calculated using TDDFT and could well explain the increase in both these signals.

3.4 Conclusion

The calculations presented in this chapter provide the absorption spectra and ESR signatures for oxygen vacancies in $\mathrm{LaAlO_3}$ that can be used to identify these defects experimentally. The electronic and geometric structure of the neutral and charged oxygen vacancies in the band gap of LAO were calculated using periodic and embedded cluster methods and hybrid density functionals. The optical absorption spectra of $\mathrm{V}_{\mathrm{O}}^{0}$ and $\mathrm{V}_{\mathrm{O}}^{1+}$ were calculated using TDDFT. The optical absorption spectra of $\mathrm{V}_{\mathrm{O}}^{1+}$ in rhombohedral LAO, which has an intensity maximum at 3.5 eV and a peak that extends from 3.2 eV to 4.0 eV, agrees well with the experimental results of Kawabe et al. [84] who see an absorption tail at 3.5-4.1 eV that they attribute to oxygen deficiency. The optical absorption spectrum for the neutral vacancy in cubic LAO, which shows an intensity maximum at 3.3 eV, has also been calculated. Both the cubic and rhombohedral absorption spectra exhibit a second absorption peak at 4.0 eV and 4.2 eV, respectively. The V_O^{1+} only exhibits one peak at 3.4 eV (cubic) and 3.6 eV (rhombohedral) which potentially allows identification of the two different charge states of the defect.

Also presented are the calculated ESR parameters of V_O^{1+} in LAO. The isotropic g-value was calculated to be 2.004026, and, due to hyperfine splitting of the nearest neighbour Al ions to the vacancy, a signal broadening of 3.0 mT is predicted. These calculations agree well with reported ESR experimental results. [43, 86]. The calculated absorption spectra of the V_O^{1+} can also be used to explain the absorption peaks observed by Yamasaka et al. [43] that appear with increased ESR signal assigned to V_O^{1+}.

This chapter is adapted from O. A. Dicks, A. L. Shluger, P. V. Sushko and P. B. Littlewood, "Spectroscopic properties of oxygen vacancies in $LaAlO_3$," *Physical Review B*, vol. 93, p.134114, 2016.

Chapter 4

The bulk properties of amorphous Al_2O_3

4.1 Introduction

4.1.1 The importance of amorphous films

In the previous chapter, the experimentally measurable spectral properties of different charge states of oxygen vacancies in crystalline $LaAlO_3$ were calculated in order to give an insight into the role of defects in the formation of the 2 dimensional electron gas in LAO/STO heterostructures, by identifying whether their energy levels will allow donation of electrons at the interface. However, in the case of LAO/STO devices [12] and its use as a gate dielectric [76,77], it is thin films of LAO that are of interest. This means that the surface morphology, interface and bulk structure of the nanometre thin films have a significant impact on device operation. Many models of heterojunctions assume that the deposited materials are crystalline and have abrupt interfaces, or that there is some limited surface reconstruction. In fact, many thin films are not even crystalline, but are instead amorphous. This means their structures display only short and medium range order, rather than being periodic, and generally have reduced ion coordination and a larger distribution of bond lengths and angles. It is therefore of vital importance to consider amorphous structures when modelling thin films.

Unlike natural glass formers, such as SiO_2, many metal oxides (e.g.

$LaAlO_3$ [83], HfO_2 [28] and Al_2O_3 [109]) can only form amorphous phases when deposited as thin films. It has been shown that amorphous metal oxide thin films can be more thermodynamically stable than crystalline films [110] when grown on a substrate. As described in [110], although the Gibbs free energy per mol of an amorphous material is higher than that of a crystalline, this is compensated by the large reduction in interface and surface energies. Crystalline interface energies are generally higher due to strain effects if there is a lattice mismatch, or because of dislocations within the material. This means that amorphous films are stable up to a critical thickness, at which point the energy difference of the bulk material begins to dominate and crystallization occurs.

Films of amorphous LAO (a-LAO) have been grown by pulsed laser deposition (PLD) [82], with the structure conformed via X-ray reflectivity measurements. PLD is a common growth technique and was even used to deposit the original LAO/STO conducting interface [12]. Other deposition techniques such as molecular beam epitaxy (MBE) [75], and spray pyrolysis [83] also produce a-LAO films, with the latter showing they are stable even when grown at temperatures above 920 K [83]. These studies demonstrate that the amorphous phase of LAO is common, and stable up to high temperatures. In order to control the properties of LAO devices, an understanding of the amorphous phase is crucial. For instance, the change in LAO structure increases the measured optical band gap from 5.6 eV [74] when crystalline, to 6.33 eV [75] in the amorphous phase.

However, $LaAlO_3$ proves difficult to model as an amorphous material. Little is known of its geometric structure and as a ternary oxide its configurational space is very large. That, coupled with a lack of experimental results to compare to, suggested that investigation of a simpler binary metal oxide would prove more initially fruitful. Like LAO, Al_2O_3 is another wide band gap, high k dielectric metal oxide, but it has been more widely studied in the amorphous phase and is being investigated for use in a variety of technological devices [22–24]. The next 3 chapters cover amorphous Al_2O_3 (a-Al_2O_3), specifically its bulk geometric and electronic structure, intrinsic charge trapping and the defects responsible for electron trapping.

4.1.2 Amorphous Al_2O_3

Thin films of amorphous alumina (a-Al_2O_3) play a key role in the development of a wide range of applications, notably non-volatile memory [22, 23] and amorphous indium gallium zinc oxide (a-IGZO) thin film transistors [24]. With its wide band gap and dielectric constant double that of SiO_2, Al_2O_3 is a suitable replacement as the blocking dielectric in these devices. It has also been investigated as both a gate dielectric and a charge trapping layer [23] in charge trap (CT) flash memory, making device fabrication easier. There are still, however, some properties of a-Al_2O_3 that must be better understood if it is to replace SiO_2 as a gate dielectric material, including charge trapping and band gap reduction. Trapped charges can act as scattering centres in the conducting channel of transistor semiconductor layers, impeding mobility, but can also act as sources of charge in CT flash memory [23]. Though recently studied [111] it is still not well understood what the exact nature of the charge traps in a-Al_2O_3 are. Intrinsic charge trapping, and, the role of defects in explaining the negative charging of a-Al_2O_3 films [22], are addressed in later chapters.

Before coming to the mechanisms for charge trapping, first the electronic structure of a-Al_2O_3 must be understood. Just as in LAO [75], there is a change in the band gap between the crystalline and amorphous phases of alumina, though in this case there is a significant decrease in the size of the gap. Whilst α-Al_2O_3 has an optical band gap of 8.8 eV [112], measurements of the amorphous band gap vary between 6.0-7.1 eV [35, 113–117]. The reduction in band gap has been attributed to the decrease in Al coordination, with theoretical work suggesting this causes a change in the electrostatic potential profile around the ions [118], shifting the bands. However, there is no consensus on whether the reduction in band gap is predominantly due to a shift of the valence [119] or conduction band [35], or whether in-gap defect states are responsible for the reduction in the optical gap [111].

Contrary experimental data and lack of a agreement on the electronic properties of a-Al_2O_3 pose significant problems for theoretical predictions of the behaviour of the band gap, band edge states and trapping of excess electrons and holes in this system. Whilst predicting electron or hole localization is a well-recognized challenge for DFT (see e.g. [120–123]), there are currently no complete models for a-Al_2O_3 structures.

In order to overcome the first problem, a range separated hybrid functional PBE0-TC-LRC [40] was tuned to satisfy the Koopmans' condition and then tested against the experimental properties of crystalline alumina. An ensemble of ten amorphous structures was generated using classical molecular dynamics and a melt and quench method and their structural characteristics compared with the experimental data. Analysis of the electronic structure of crystalline and amorphous alumina then demonstrates that the band gap reduction is due to a shift in both the valence and conduction bands. This is explained by the change in Al and O coordination leading to shifts in the electrostatic potentials and different bonding characteristics.

4.2 Methodology

The first challenge in accurately modelling the electronic properties of a-Al_2O_3 using DFT is generating representative geometric structures of the material. Here a molecular dynamics melt and quench approach is adopted. This is a computationally inexpensive way of producing the large number of structures necessary to provide an accurate sample of potential amorphous configurations, provided a suitable potential is used. The theoretical background of molecular dynamics (MD) is covered in section 2.1 and its application to the melt and quench method is covered in this chapter in section 4.2.1.

Due to the uncertain nature of the band gap and band edge states, choosing the correct DFT setup and functional is also important. The functional must be able to accurately predict the behaviour of the amorphous electronic structure, which often involve localized states, and be suitable for modelling intrinsic charge trapping and defects.

It is also important to consider the size of the system. Amorphous materials are non-periodic, and so larger cells are preferred. Unlike in the bulk crystalline phase where localization of a small radius polaron may take place at all equivalent lattice sites with equal probability, in amorphous structures all sites are different and charge trapping takes place at intrinsic structural precursor sites. The concentration of such sites is system specific and is difficult to predict *a priori*. At some of these sites carriers can trap spontaneously, whereas at others trapping requires overcoming an energy barrier. For example, the number of trapping sites where electrons can localize spontaneously in a-SiO_2 has been shown to be around $4\text{x}10^{19}$ cm^{-3} [124]. Therefore finding one such site in a periodic cell of SiO_2 requires a cell size of around 1000 atoms. Using periodic cells is required in order to avoid border effects which may affect the characteristics of trapped charges in finite systems. However, this makes the amorphous structures quasi-periodic and induces constraints on the structural relaxation accompanying charge trapping. Taken together these factors imply that simulations should be performed in the largest periodic cells feasible for DFT calculations. However, variations in density and atomic coordination can affect the bulk electronic properties [35], and for localized charges different site configurations will change the profile and spectroscopic properties of traps and defects [111]. To credibly predict distributions of properties, calculations in many models are required.

4.2.1 Generation of the amorphous structure

In order to create sufficient statistics, 10 sample structures of amorphous Al_2O_3 have been generated using an MD melt and quench approach run using the LAMMPS code [125] and then fully relaxed using a DFT calculation described later in section 4.2.2.

The MD simulation uses a 360 atom supercell of α-Al_2O_3 as the initial structure. This cell size represents a compromise between the size of the cell and computer time required to achieve representative distributions of densities, ion coordination numbers and charge trap properties. The NPT (constant particle number, pressure and temperature) ensemble is used with a time-step of 0.1 fs. There are 2 approaches to this method, regarding whether to hold the pressure or the volume constant. Holding the volume constant allows experimentally measured densities to

Atom	$q(e)$	A(Å)	B(Å)	C(Å^{3}eV$^{1/2}$)	D(Å^{-1}eV)
Al	1.4175	0.7852	0.034	0.3816	0.04336
O	-0.9450	1.8215	0.138	0.9391	0.04336

Table 4.1: Parameters for the potential [45] used to generate the amorphous Al_2O_3 structures.

be achieved, but may artificially confine the system to some symmetry or configuration. Allowing the volume to vary and fixing the pressure at 1 atmosphere was deemed to produce a more representative distribution of densities, within experimental ranges, and coordination profiles.

The MD melt and quench process itself is carried out as follows. The initial structure is first equilibrated at 300 K for 10 ps. The temperature is then increased to 5000 K over 20 ps. This is then followed by an equilibration at 5000 K for 20 ps. The structure is then cooled to 1 K to generate the final structure, with cooling rates of 1 Kps^{-1}, 10 Kps^{-1} and 100 Kps^{-1} being investigated. Different structures are generated by using a different random number seed for the initial velocity distribution.

The structural properties of the amorphous samples produced are mainly dependent on the potential used and the cooling rate of the MD simulation. The potential selected for this study has been previously used to model a-Al_2O_3 [45, 46]. It is a Born-Mayer potential with an added van der Waals term:

$$V(r_{ij}) = \frac{q_i q_j}{r_{ij}} - \frac{C_i C_j}{r_{ij}^6} + D(B_i + B_j)\exp\left(\frac{A_i + A_j - r_{ij}}{B_i + B_j}\right), \tag{4.1}$$

where the parameters for the potential are given in Table 4.1. The selection of the cooling rate and analysis of the structures is covered in section 4.3.2.

4.2.2 DFT calculations

The electronic structure of crystalline and amorphous Al_2O_3 was calculated using the CP2K package [44]. CP2K makes use of hybrid Gaussian and plane wave type basis sets. All calculations are run at the Γ point of the Brillouin zone. The

DZVP-MOLOPT-SR-GTH [103] basis sets were used for both O and Al, along with the Goedecker-Teter-Hutter (GTH) pseudopotentials [55, 56]. The converged plane wave energy cutoff was set to 500 Ry and the SCF convergence criterion was set to a maximum energy difference of 10^{-6} a.u. between steps. All final geometry relaxations were performed using the PBE0-TC-LRC [40] hybrid functional described below and used the conjugate gradient optimizer with a maximum force convergence criterion of 0.05 eV/Å for each atom. The auxiliary density matrix method [126] (ADMM) was used to reduce the computational cost associated with using the range separated hybrid functional, allowing the calculation of relatively large 360 atom systems.

4.2.2.1 Tuning the functional

Self-trapped polarons in crystals usually have small trapping energies of the order of 0.1-0.3 eV. This means that even qualitative predictions of their stability are greatly affected by the choice of the Hamiltonian. The early many-electron calculations of polarons and excitons in insulators were carried out using the Hartree-Fock method (e.g. [127, 128]) and semi-empirical quantum chemistry techniques (e.g. [129, 130]), which tend to over-localize electronic states. This is not a big problem for e.g. calculating the spectroscopic properties of well localized polarons. However, predicting the formation and stability of polaronic states remains a challenge. It was realized early on that in DFT the LDA and GGA approximations tend to delocalize electrons and fail to predict exciton [121] and hole polaron [120] localization in well-established cases. This has been attributed to the self-interaction error [120, 121] and a quick fix of adjusting the amount of Hartree-Fock exchange in hybrid density functionals has been widely implemented to provide the electron localization in known cases (e.g. [120, 131, 132]). A cheaper and more targeted approach is to adjust the U parameter in LDA+U or GGA+U calculations of polaron states. Several flavours of this approach have been suggested over the years, as discussed in refs. [133–136], and it is still very widely used. The predictive power of these two approaches is again limited but they can be used very effectively in 'test and predict' mode where the parameters (e.g. the amount of HF exchange or the U value) are first fitted to reproduce the established data and then the same parameters are used for predictive calculations. However, the transferability of these parameters between materials is quite limited.

It has been noted more generally [123, 137] that failures of DFT to correctly predict localization of electronic states and charge transfer spectra are associated with a wrong asymptotic behaviour of approximate exchange-correlation (XC) potentials for isolated molecules, 'nearsightedness' of XC response kernels, and lack of the integer discontinuity [137]. Therefore significant recent efforts have focused on creating so called Koopman's-compliant exchange-correlation functionals with piecewise linearity with respect to fractional particle occupations and developing range-separated hybrid functionals for molecular systems [135, 138–140]. A commonly used method is to correct the non-piecewise linearity of the total energy (E) with respect to (the continuous) electron particle number (N) in DFT systems [135, 138]. The linearity condition, where $d^2E/dN^2 = 0$, is shown to be a property of the exact exchange-correlation functional by Perdew et al. [141]. Local and semi local functionals deviate from the straight line behaviour, instead showing curvature where $d^2E/dN^2 > 0$, while in HF theory the opposite behaviour is observed and $d^2E/dN^2 < 0$. Lany and Zunger [135] proposed that, by enforcing the linearity condition, the energy of the self-interaction of the electron or hole after addition is canceled by the energy of the wavefunction relaxation, allowing a more accurate description of localized states. Thus by either applying DFT+U [135] or the use of hybrid functionals [138], the linearity condition can be enforced. It has not been demonstrated that satisfying this condition is necessary for a correct description of electron localization. However, it has been observed that localization can indeed be achieved by tuning the parameters of the effective localizing potential [135] to satisfy the linearity condition.

In an alternative approach [139, 142], range separated hybrid functionals are investigated, with parameters optimally tuned so that the generalized Koopmans' condition is enforced, equivalent to ensuring the linearity condition as in the methods mentioned above. This enables quantitative predictions of band gaps and energy levels in molecules to be made without the need for empirical matching. This approach, however, cannot be easily generalized for infinite solids [143].

In this work a similar approach is tested where the range separated hybrid functional PBE0-TC-LRC [40] is used with a tuned cutoff radius. This functional has been introduced to allow efficient calculation of exact exchange in Γ point codes, such as CP2K, and provides large speedup of the calculations without loss of accuracy. The exchange-correlation part of the PBE0-TC-LRC functional has the form

$$E_{\mathrm{xc}} = aE_{\mathrm{x}}^{\mathrm{HF,TC}} + aE_{\mathrm{x}}^{\mathrm{PBE,LRC}} + (1-a)E_{\mathrm{x}}^{\mathrm{PBE}} + E_{\mathrm{c}}^{\mathrm{PBE}} \; . \tag{4.2}$$

PBE0 is the standard PBE hybrid functional [57, 58] with a = 0.25. $E_{\mathrm{x}}^{\mathrm{HF,TC}}$ is the truncated Hartree-Fock exchange, $E_{\mathrm{x}}^{\mathrm{PBE,LRC}}$ is the long range PBE exchange with a truncated Coulomb potential, $E_{\mathrm{x}}^{\mathrm{PBE}}$ is the PBE exchange and $E_{\mathrm{c}}^{\mathrm{PBE}}$ is the PBE correlation. The truncated Coulomb (TC) version of the Hartree-Fock exchange takes the form

$$E_{\mathrm{x}}^{\mathrm{HF,TC}} = -\frac{1}{2}\sum_{i,j}\iint \psi_i(r_1)\psi_j(r_1)g_{tc}(r_{12}) \times \psi_i(r_2)\psi_j(r_2)d^3r_1d^3r_2 \tag{4.3}$$

where the operator

$$g_{tc}(r_{12}) = \begin{cases} \frac{1}{r_{12}} & \text{for } r_{12} < R \\ 0 & \text{for } r_{12} > R \end{cases} \tag{4.4}$$

where R is the cutoff parameter. The long-range correction (LRC) is based on the PBE exchange hole [40]. This functional is similar to HSE06 [60–62] in that, unlike many other range-separated hybrid functionals, it uses short-range exact exchange and a long-range semi-local functional.

Here the cutoff radius R is used as a variational parameter which is tuned to minimize a deviation of the functional from straight line behaviour, unlike e.g. in previous work [138], where the proportion of exact exchange, a was varied, though both change the contribution of the exact exchange to the energy (see also [140]).

To find the cutoff parameter, R, the same method as in refs. [139, 140] is used.

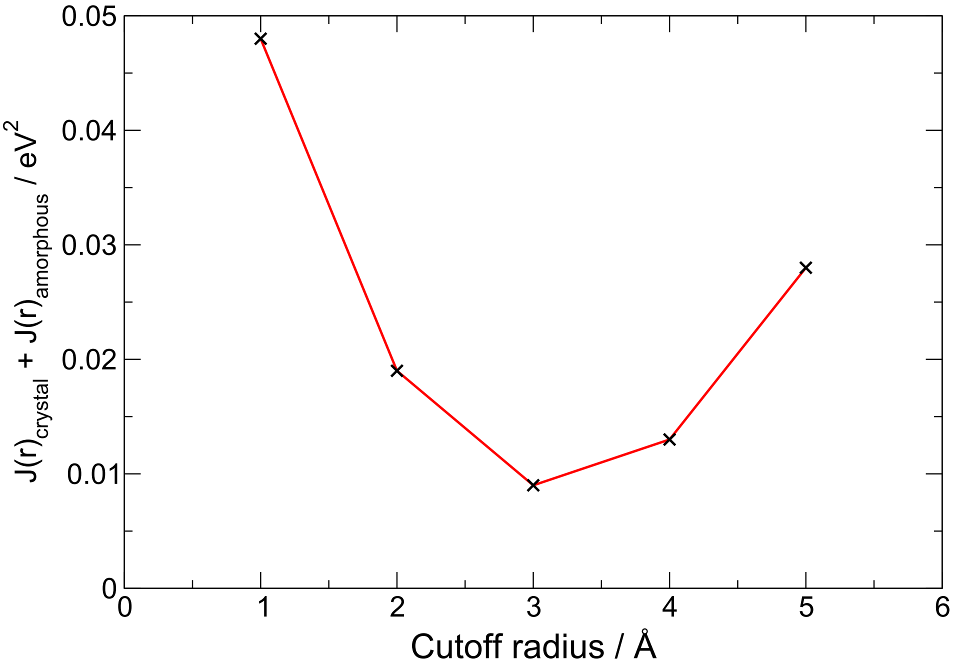

Figure 4.1: The total of the $J(R)$ functions of both the amorphous and crystalline structures plotted against the PBE0-TC-LRC cutoff radius. It can be seen that the error is at a minimum when R=3.0 Å.

The exact form of Koopmans' Theorem in Kohn-Sham theory is given by the expression:

$$\varepsilon_{\mathrm{HOMO}}(N) = -I(N), \tag{4.5}$$

where $\varepsilon_{\mathrm{HOMO}}(N)$ is the energy of the K-S highest occupied molecular orbital (HOMO) and $I(N)$ is the ionization potential of the N electron system. The ionization potential of the N electron system can also be defined;

$$I(N) \equiv E_{\mathrm{gs}}(N-1) - E_{\mathrm{gs}}(N), \tag{4.6}$$

the difference between the energy of the ground state of the $N-1$ electron, $E_{\mathrm{gs}}(N-1)$, and N electron, $E_{\mathrm{gs}}(N)$ system, or the energy to remove an electron from the system. A similar condition can be imposed for the addition of an electron to the system, where the lowest unoccupied molecular orbital (LUMO) energy is equated

Lattice parameter	Theory (Å)	Experiment (Å)	Error
a	4.7555	4.7605	-0.1%
b	8.2370	8.2454	-0.1%
c	12.9730	12.9956	-0.2%

Table 4.2: Comparison of the calculated lattice parameters for corundum α-Al_2O_3 with the experimental data [144].

with the electron affinity. From these equations R can then be tuned so that the function [142]

$$\begin{aligned} J(R) = {} & [\varepsilon^{R}_{\mathrm{HOMO}}(N) + I^{R}(N)]^2 \\ & + [\varepsilon^{R}_{\mathrm{HOMO}}(N+1) + I^{R}(N+1)]^2 \end{aligned} \tag{4.7}$$

is minimized. This equation also accounts for the error in the LUMO level, or the $N+1$ system, important when investigating the possible localization of electrons. This functional is applied in a 'test and predict' manner, the functional is first tested using the data available for crystalline alumina and then used to make predictions for the amorphous structure.

As one can see in Fig. 4.1, the deviation of straight line error (DSLE) is minimized when R=3.0 Å. At this cutoff the largest absolute error in fulfilling the Koopman's condition is 0.04 eV. It is significantly smaller than the trapping energies and therefore may allow qualitatively accurate predictions of the properties of trapped holes and electrons in both crystalline and amorphous alumina.

4.3 Results and Discussion

4.3.1 Properties of α-Al_2O_3

In order to test the tuned PBE0-TC-LRC [40] functional, it was benchmarked against known structural and electronic properties of the crystalline system. The calculated lattice parameters of the 360 atom α-Al_2O_3 cell were in good agreement with x-ray crystallography data [144] (see Table 4.2), with the lengths of all lattice vectors within 0.2% of the experimental values after a full cell relaxation, and no change to the angles of orthorhombic cell.

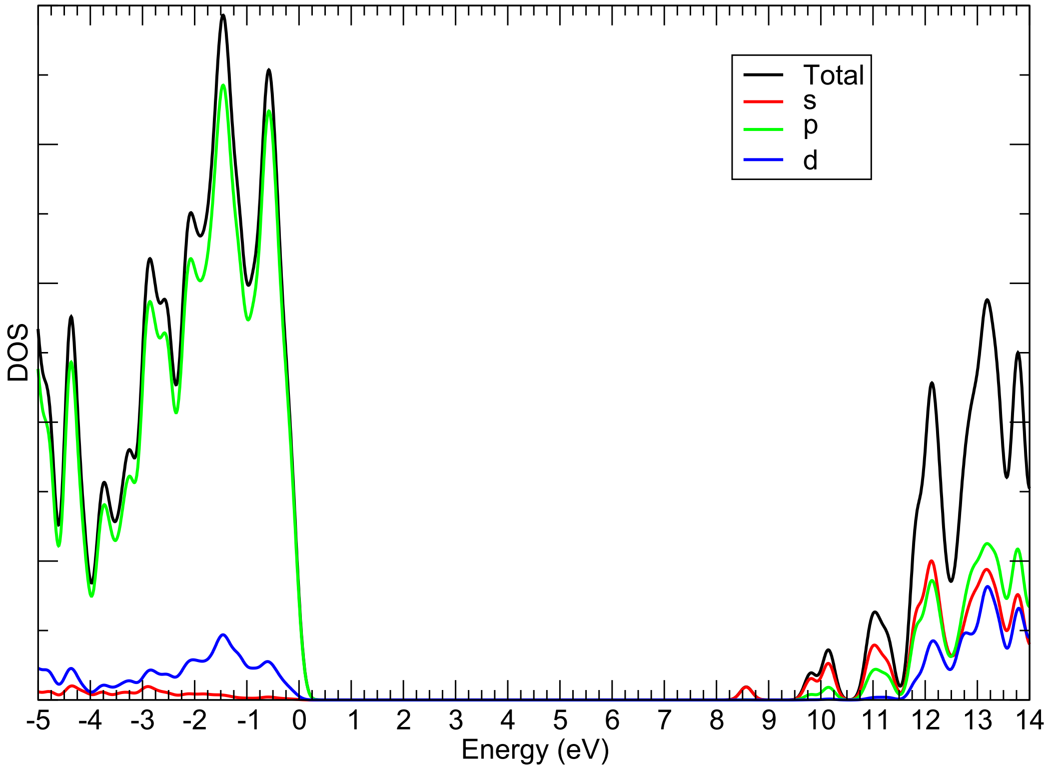

Figure 4.2: The projected density of states (PDOS) of α-Al_2O_3.

The functional also accurately reproduces the bulk electronic as well as geometric structure. The K-S band gap was calculated to be 8.6 eV (see Table 4.3), which is close to the experimental optical band gap of 8.8 eV [112]. It should be noted that the functional was tuned to obey the Koopmans' condition, rather than fit to empirically match the experimental optical band gap. For comparison, the electronic structure was also calculated using the HSE06 [60, 61] functional and the PBE0-TC-LRC functional with a larger cutoff of 5.0 $\AA$ (see Table 4.3). It can be seen that HSE06, whilst having a similar DSLE, underestimates the band gap by approximately 0.8 eV, and a larger cutoff radius increases the DSLE with only a small change in band gap of 0.1 eV.

Structurally, α-Al_2O_3 is composed of edge and corner sharing Al centred octahedra, meaning all Al are 6 coordinated with O, denoted $^{[6]}$Al (see Fig. 4.3a). Conversely all O are 4 coordinated with Al ($^{[4]}$O), forming O centred distorted tetrahedra as can be seen in Fig 4.3b. The wide band gap and overall electronic structure

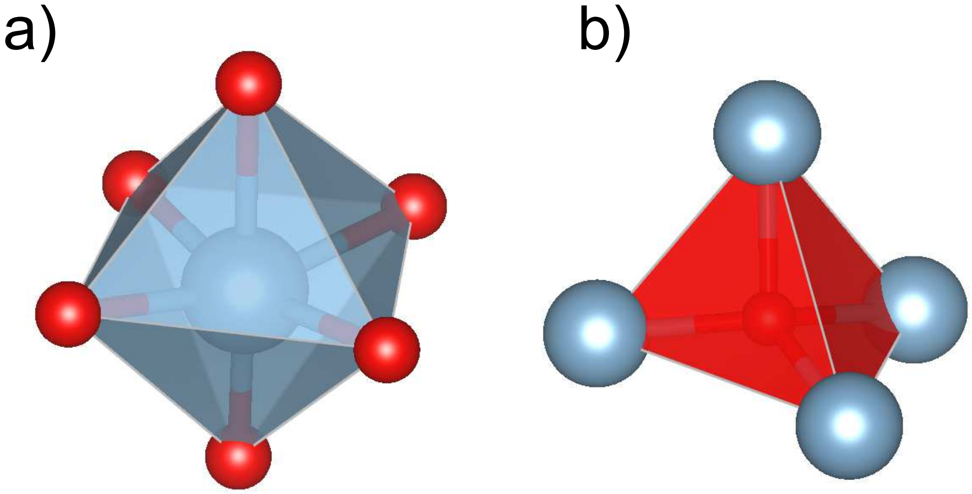

Figure 4.3: The building blocks of α-Al_2O_3 a) Al centred octahedra and b) O centred tetrahedra.

of α-Al_2O_3 can be understood by considering the geometric structure of the material and the atomic orbitals responsible for the bands. From the projected density of states (PDOS) (see Fig.4.2), it can be seen that the valence band edge is predominantly composed of O $2p$ orbitals. The valence band maximum is very flat, which can be understood by considering the tetrahedral configuration of O, which allows hybridization of the more covalent *sp* type orbitals [145]. There is a small contribution to the valence band from Al *d* orbitals which could be as a result of distortion of the O tetrahedra towards a square planar formation which allows *spd* hybridization. The conduction band minimum (CBM) on the other hand is almost entirely composed of Al $3s$ states, and has a very high dispersion as a result. Even though the Al octahedra are distorted, they are less distorted than the O centred tetrahedra and the inversion centre symmetry prevents significant *sp* mixing, resulting in the CBM being 99% pure *s* character.

Other crystalline phases, such as θ and γ-Al_2O_3, have lower band gaps than α-Al_2O_3, 6.2-6.5 eV [146] and 7.6 eV [35] respectively. The decrease in band gap of these phases is correlated with an increase in the number of 4 coordinated Al. This has been explained in theoretical work by an increase of *sp* mixing in the conduction band edge due to the tetrahedral units [147], though also observed is an increase in the width of the valence band in γ-Al_2O_3. That aluminium in Al_2O_3 can form

Functional	Maximum DSLE (eV)	Kohn-Sham Bandgap (eV)	Hole E_{trap}(eV)
HSE06 [60,61]	0.04	8.1	0.13
PBE0-TC-LRC R = 3.0	0.04	8.6	0.38
PBE0-TC-LRC R = 5.0	0.10	8.7	0.42

Table 4.3: Comparison of the properties of the crystalline, α-Al_2O_3, system calculated using the HSE06 [60,61] functional and PBE0-TC-LRC [40] functionals with a varied cutoff.

2 different structural units has been attributed to its definition as an 'intermediate glass former'. Merely by consideration of ion size and Pauling's packing rules Al has the possibility of forming both octahedral and tetrahedral units. These phases of mixed coordination could help explain the shift in band gap and band offsets in a-Al_2O_3.

4.3.2 The geometric structure of a-Al_2O_3

To study the band structure and the trapping of polarons in amorphous alumina, the geometric structures used for calculations have to accurately reproduce the overall topology and local features of the material. The geometric properties of the 10 a-Al_2O_3 structures generated in this study through MD melt-quench show excellent agreement with experimentally measured densities, coordination numbers and x-ray diffraction data of lab grown thin films. After the structures were generated using MD melt-quench procedure, a full cell optimization was performed using the PBE functional. A final geometry optimization was then performed using the tuned PBE0-TC-LRC [40] functional.

The density of α-Al_2O_3 (a crystalline phase) is 3.95 gcm^{-3}, but when thin films of amorphous alumina are grown, large changes in the density of the material are detected (see Table 4.5). Groner et al. [33] deposited thin films of alumina at varying low temperatures using ALD on n-type silicon wafers and Quartz Crystal Microbalance (QCM) substrates. The QCM was used to measure the mass of a film whilst various other measurement techniques were used to determine the thickness including AFM and spectroscopic ellipsometry. X-ray Reflectivity (XRR)

Cooling rate	Average density (gcm^3)	Coordination number (%) $^{[4]}$Al	$^{[5]}$Al	$^{[6]}$Al
Experimental	2.46-3.25	55	42	3
100 Kps^{-1}	3.09	58	35	7
10 Kps^{-1}	3.14	53	37	10
1 Kps^{-1}	3.31	45	25	30

Table 4.4: Average densities and coordination numbers of a-Al_2O_3 produced by the 3 different cooling rates during the MD melt and quench compared to experimental densities [33, 148] and coordination numbers [39].

was also used independently to determine the density. These different measurement techniques gave a range of values for the density but most methods were within $0.1\,g\mathrm{cm}^{-3}$ of each other. The average reported densities were 3.0 gcm^{-3} for films grown at 177°C and $2.5\,\mathrm{gcm}^{-3}$ for those grown at 33°C. Measurements of alumina film density performed by Ilic et al. [148] on ALD ultrathin films using nano-mechanical oscillators give a value of 3.2 ± 0.1 gcm^{-3}. The densities of the melt-quench generated structures of a-Al_2O_3 that were cooled at 10 Kps^{-1} agree very well with the experimental values, with the densities lying within the range of 3.06-3.25 gcm^{-3} (see Table 4.5), with an average density of 3.14 gcm^3.

Lee et al. [39] use 2D 3QMAS NMR to measure coordination numbers of ions in thin films of Al_2O_3 deposited on Si(100) wafers by RF magnetron sputtering at low temperatures. They measured the distribution of coordination numbers of Al with O to be $^{[4]}$Al $55\% \pm 3\%$; $^{[5]}$Al $42\% \pm 3\%$; $^{[6]}$Al $3\% \pm 2\%$ (see Table 4.4). This is a large change in coordination number from α-Al_2O_3 where all Al are 6 coordinated. Instead, the amorphous phase is primarily composed of $^{[4]}$Al tetrahedra with some $^{[5]}$Al, and a very small percentage of $^{[6]}$Al octahedra. As can be seen from Table 4.4 slower cooling rates resulted in higher densities and a increase in proportion of $^{[6]}$Al. After annealing at high temperatures alumina thin films undergo a phase change from a- to γ-Al_2O_3 [149], corresponding to an increase in density, and an upward shift of the conduction band which has been associated with an increase in the number of Al octahedra. Other work sees an increase of density after

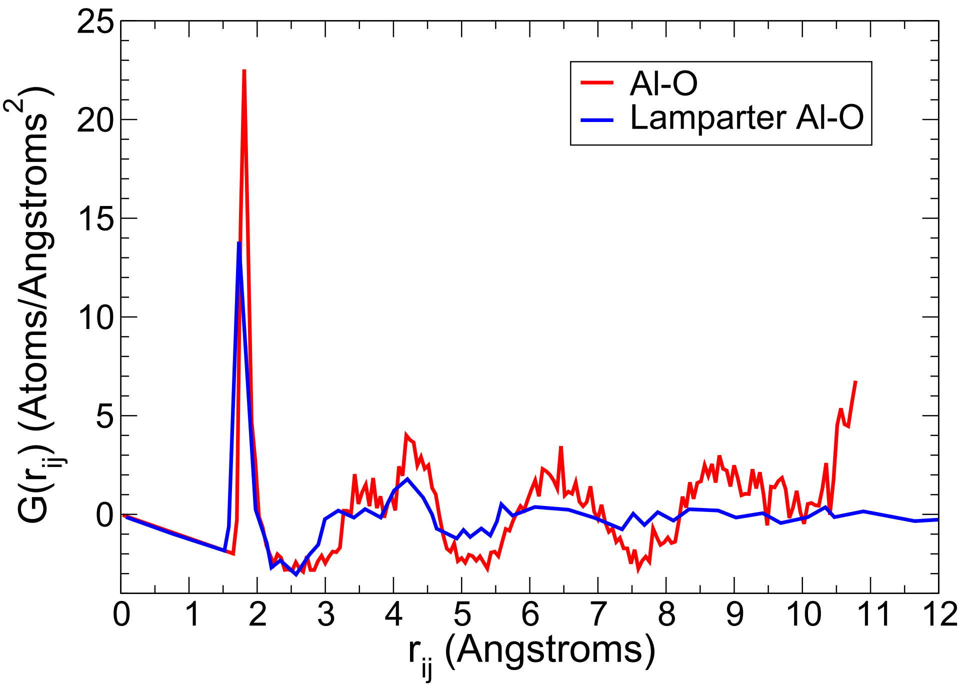

Figure 4.4: Comparison of the calculated and experimental [38] radial correlation function $G(r_{ij})$ for Al-O coordination.

annealing, but does not ascribe this to a large re-organizing of the Al coordination but to an increase in long range ordering [150]. Either way this suggests that some films could have a similar structure to those produced by the 1 Kps^{-1} cooling rate, after annealing, as they undergo transition from the amorphous to crystalline phase. However, overall the structures generated using the 10 Kps^{-1} cooling rate show the best and most consistent agreement with the experimental values for coordination number and the densities all fall within the experimental range. The following results presented were calculated using these structures.

The Al-O radial correlation function of the amorphous structures, shown in Fig. 4.4, agrees well with the x-ray and neutron diffraction studies performed by Lamparter [38], with the peak maxima within $0.05\AA$ of the experimental results, though there is a small difference variation in peak width. This is evidence that the generated structures, aside from having good agreement with experimental densities and coordination numbers, also recreate the correct short and medium range order

Authors	Growth technique	Substrate	Measuring technique	Density /gcm^{-3}
Groner et al. [33]	ALD(306 K)	n-type Si	XRR	2.46
	ALD(450 K)	n-type Si	XRR	3.06
Ilic et al. [148]	ALD	Si	NEMS	3.20
Ok et al. [24]	ALD	SiN$_x$	XRR	2.97-3.14
PBE0-TC-LRC				3.14

Table 4.5: Densities of a-Al_2O_3 measured using a variety of experimental techniques and compared to the average density calculated using DFT in this work.

of a-Al_2O_3.

4.3.3 The electronic structure of a-Al_2O_3

Having demonstrated that the tuned density functional gives good agreement with the experimental data for α-Al_2O_3 and that the generated structures of a-Al_2O_3 are representative of real films, the electronic structure of a-Al_2O_3 can now be considered. The average Kohn-Sham band gap is calculated to be 5.48 eV from the 10 a-Al_2O_3 structures, with a range of 5.21-5.89 eV. Experimentally the band gap has been measured to be 6.0-7.1 eV [35, 113–117], though often tails are observed in the spectra which are most likely due to localized states at band edges. In order to interpret the experimental results in comparison to the DFT calculations the nature of the band edges has to be carefully considered.

To visualize localized states the electronic structure of amorphous solids can be further characterized using the inverse participation ratio (IPR). This method takes advantage of the atom centered basis set used in CP2K to quantify the degree of localization of each eigenvector. It has often been used to characterize localization of vibrational and electronic states in amorphous solids [151–155]. The IPR is defined as:

$$IPR(\psi_n) = \frac{\sum_{i=1}^{N} a_{ni}^4}{(\sum_{i=1}^{N} a_{ni}^2)^2} \tag{4.8}$$

where

$$\psi_n = \sum_{i=1}^{N} a_{ni}\phi_i \tag{4.9}$$

is the *n*th Kohn-Sham eigenvector (MO), N is the number of atomic orbitals, ϕ_i is the *i*th atomic orbital and a_{ni} is the coefficient of MO n and atomic orbital i. The IPR is 1/N for completely delocalized MOs, and 1 for MOs that are localized on a single atomic basis orbital.

The IPR analysis of a-Al_2O_3, shown in Fig. 4.5b, demonstrates that there are many localized states at the top of the valence band, but the bottom of the conduction band is formed by delocalized states. Crucially, the states in the valence band only become completely delocalized approximately 1.0 eV below the HOMO, which can be attributed to the onset of the mobility edge. The mobility edge is usually defined as a transition between localized states, which do not contribute to the electrical conductivity of the system, and extended states, which can contribute to the electrical conductivity in disordered materials [156]. Using the IPR analysis, one can approximately define the mobility edge as the onset of states with an IPR corresponding to delocalized states [153, 155, 157].

The position of the mobility edge could explain the discrepancy between the calculated HOMO-LUMO gaps (the difference in energy between the HOMO and LUMO levels), which are approximately 5.5 eV, and the experimentally measured band gaps of 6.0-7.1 eV [35, 113–117]. The majority of the experimental band gaps are measured using electron energy loss spectroscopy (EELS) [111] or x-ray photoemission spectroscopy (XPS) [35, 114, 117], and it is likely that the localized band edge states will have different interaction cross sections than the delocalized states at the mobility edge, and could account for the tails observed in the spectra. For example a recent paper [111] reports a band gap of 7.1 eV from EELS measurements, but also shows a non-zero scattering intensity to below 6 eV, in agreement with the calculations presented in this chapter. The density of states is also larger at the mobility edge, which would increase the intensity of any interactions. If measured from the mobility edge, the average calculated band gap becomes 6.5 eV, which is within the range measured experimentally.

Unlike the valence band, the IPR analysis of the conduction band shows it to be composed of delocalized states (see Fig. 4.5b). The lack of electron localization

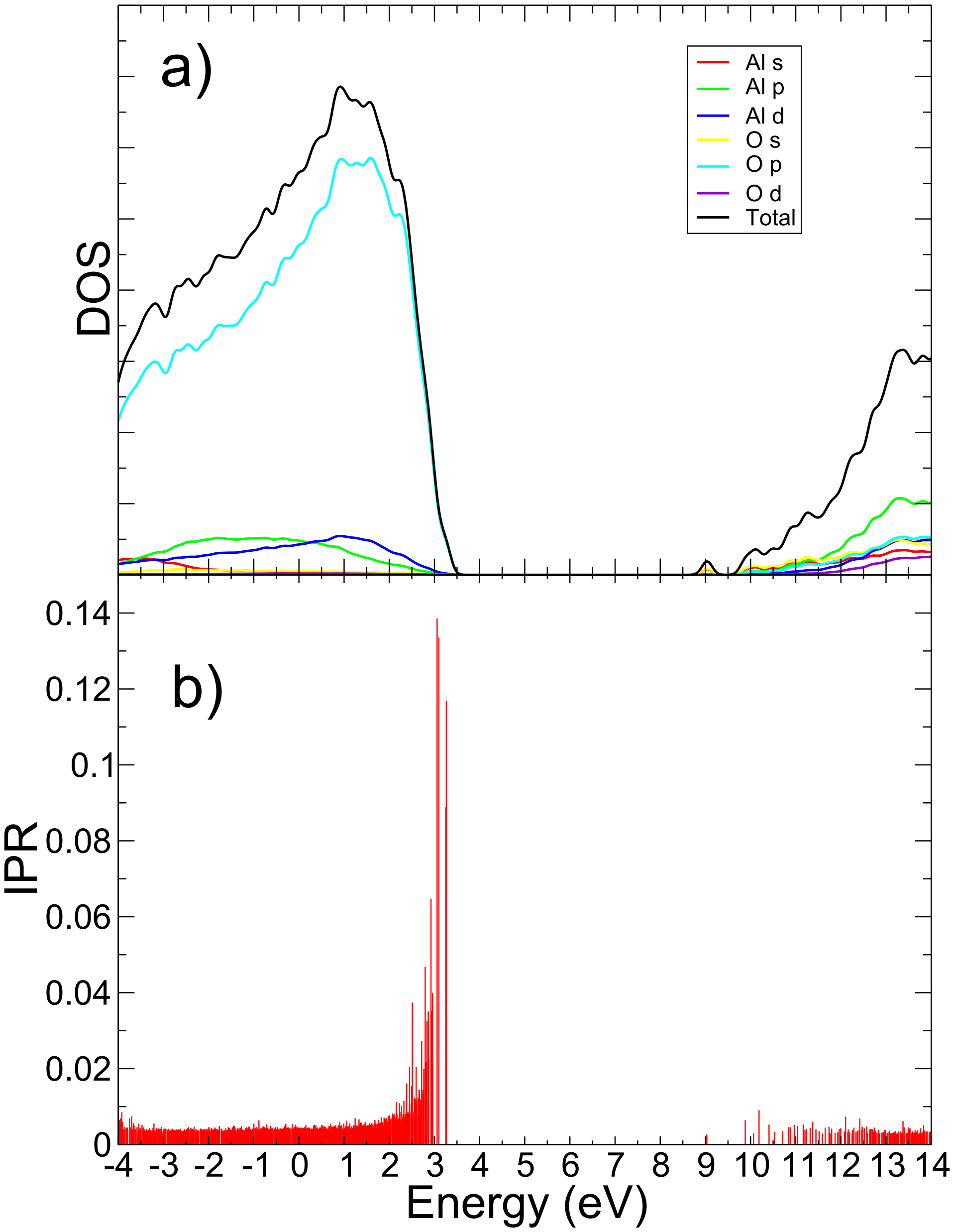

Figure 4.5: (a) The projected density of states (PDOS) and (b) inverse participation ratio (IPR) of one structure of a-Al_2O_3, showing strong localization of the top of the valence band.

at the conduction band edge when compared to the valence band is most likely due to their respective orbital character. As the density of states in Fig. 4.5a shows, the top of the valence band is composed of O $2p$ orbitals, whereas the bottom of the conduction band is composed predominantly of Al $3s$ orbitals. These states demonstrate a very high dispersion in crystalline corundum structures [158] which projects into the a-Al_2O_3 states in terms of band unfolding procedure [159]. High electron mobilities have been measured experimentally in amorphous Al_2O_3 [42], with electron effective masses of 0.4 m_0. The high electron mobility measured can be explained by the high dispersion of the conduction band, which results in the small IPR values and a lack of localization at the band edge.

That the band gap narrows between the α and amorphous phases of Al_2O_3 is not controversial, however, there is disagreement as to whether the valence or conduction band is most responsible for the shift. X-ray photoelectron spectroscopy (XPS) measurements [35] suggest that there is only a small shift of the valence band downwards (with respect to the vacuum level) of approximately 0.3 eV, though a tail possibly due to higher lying states can be observed. Instead the majority of the band gap change is due to a shift of the conduction band downwards by 2.14 eV between α and a-Al_2O_3, or 0.77 eV between γ and a-Al_2O_3. The shift in conduction band is accompanied by an increase in peaks associated with *p*-*p* transitions in the XPS spectra that would be symmetrically forbidden if the Al were all 6 coordinated octahedra, but can be explained by an increase in the number of Al centred tetrahedral units. Thus it is suggested [35] that the decrease in the conduction band is due to under coordinated Al structural units that allowing greater hybridization of the Al and O atomic orbitals.

The DFT calculations presented here support this interpretation. The density of states projected onto O and Al ions with different coordination, displayed in Fig. 4.6, shows that $^{[4]}$Al contribute the most to the bottom of the conduction band, with $^{[6]}$Al contributing the least. It can be observed from Fig. 4.6 that there is an increase in the contribution of the $^{[6]}$Al approximately 2 eV into the conduction band. There is mixing observed, but it is to be expected, especially as all the structural units

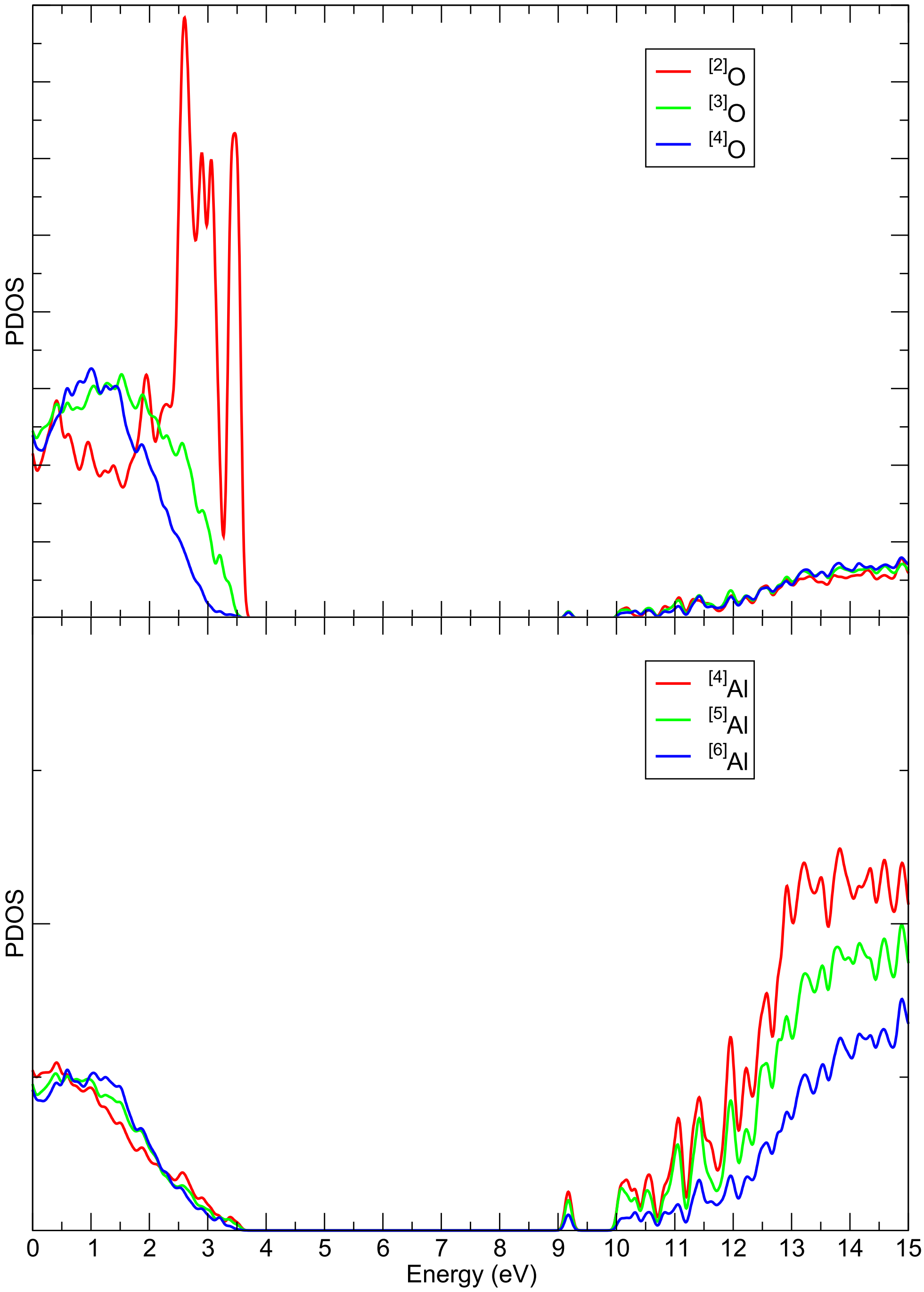

Figure 4.6: The projected density of states (PDOS) showing the contribution from each of the different coordinations of O and Al which has adjusted to account for their proportion within the sample.

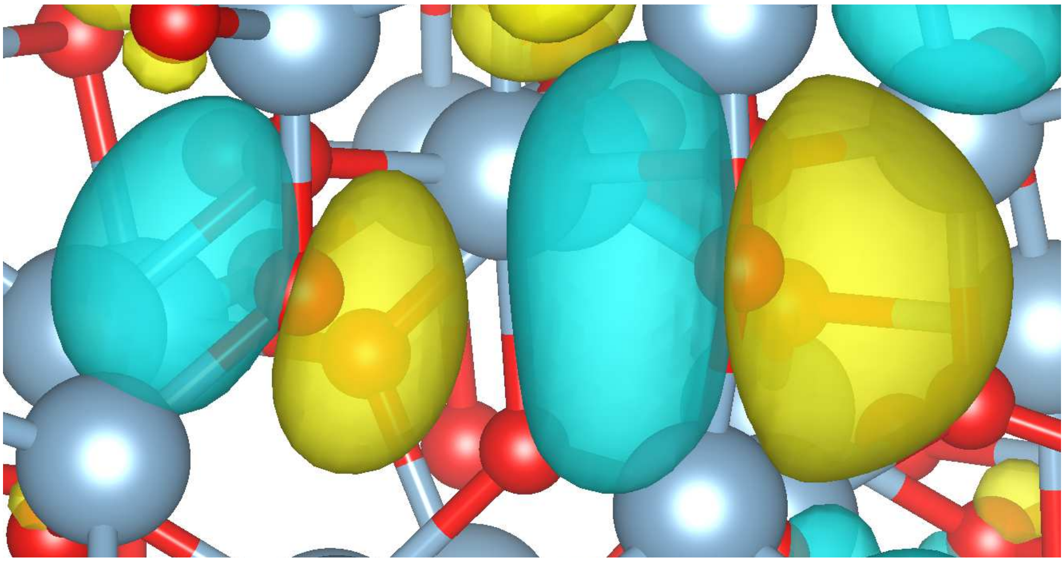

Figure 4.7: An example of the wavefunction of a molecular orbital from the top of the valence band in a-Al_2O_3 showing the σ^*_{2p} anti-bonding type orbitals formed between 2 nearest neighbour $^{[2]}$O.

will be distorted from perfect symmetry in the amorphous phase, but the evidence suggests that the increase in the number of Al tetrahedral sites lowers the conduction band. Unlike $^{[6]}$Al octahedra, the tetrahedral symmetry allows *sp* hybridization. That this occurs is backed up by an increase in the contribution of *p*- and *d*-type orbitals to the bottom of the conduction band, so that in the amorphous case it is only approximately 90% *s* character, reduced from 99% in the crystalline case.

Other experimental work [119] suggests it is a shift in the valence band rather than the conduction band that narrows the band gap. In [119] only the conduction band offset between Si and γ-Al_2O_3, and Si and a-Al_2O_3, are measured. The relative valence band shift is then estimated from previous measurements of the band gap. However, a band gap of 8.7 eV is used for γ-Al_2O_3, very close to the α-Al_2O_3 band gap of 8.8 eV, where other measurements report lower band gaps of 7.6 eV [35] for γ-Al_2O_3. In fact the conduction band shift of 0.5 eV [119] measured between a- and γ-Al_2O_3 is not much smaller than the 0.77 eV measured in [35]. If this is taken into account it would suggest that there would be a further increase in the conduction band offset if there was a phase change to α-Al_2O_3, and that it is the conduction band that lowers between the 2 phases.

The approximate 2 eV shift observed in the conduction band does not account for the 3.3 eV decrease in the DFT calculated band gap between crystalline and amorphous Al_2O_3. The reason why the HOMO-LUMO gap underestimates the band gap when compared to experiment has already been attributed to the onset of the mobility edge. It seems likely that the same 1-1.5 eV wide localized region at the edge of the valence band observed in the IPR spectra, and responsible for tails in EELS and optical spectra, is also responsible for the decrease in the DFT HOMO-LUMO gap. In Fig. 4.6 it can be clearly seen that states associated with 2 coordinated oxygen ions contribute strongly to the top of the valence band. The under coordinated $^{[2]}$O form σ^*_{2p} anti-bonding type orbitals (See Fig. 4.7) resulting in their higher energies than the rest of the valence band states, and an increase in localization. The data as a whole suggests there is a shift in the HOMO level upwards of approximately 1.5 eV due to these localized states, when compared to the position of the density of states of the 4 coordinated O, which are more similar to the O in crystalline Al_2O_3

It is important to see if the change in bonding character between Al and O as a result in the change of geometric structure also affects the electrostatic potential profile around the ions. Previous DFT calculations [118], using LDA functionals, suggest that the change in electrostatic potential at the maximum electron distribution radius (0.4 Å and 1.0 Å for O and Al respectively) shifts the position of the a-Al_2O_3 valence band down 1 eV from that of α-Al_2O_3, and the conduction band 3.5 eV down. They assume that that the change in potential directly lowers the KS levels at the Γ point and so accounts for the 2.5 eV lowering of the band gap they observe, and that the potential shift of O is responsible for the valence band shift and Al for the conduction band shift. However, it is difficult to directly compare absolute values of potentials between separate DFT calculations as there is no well defined vacuum or reference level.

To address this the electrostatic potentials presented here[1] have been spherically averaged around each ion and then, individually for both amorphous and crys-

---

[1] With thanks to Dr. Al-Moatasem El-Sayed who wrote the program to calculate potentials from CUBE files, and Rasmus Jakobsen for adapting it to analyze specific atoms.

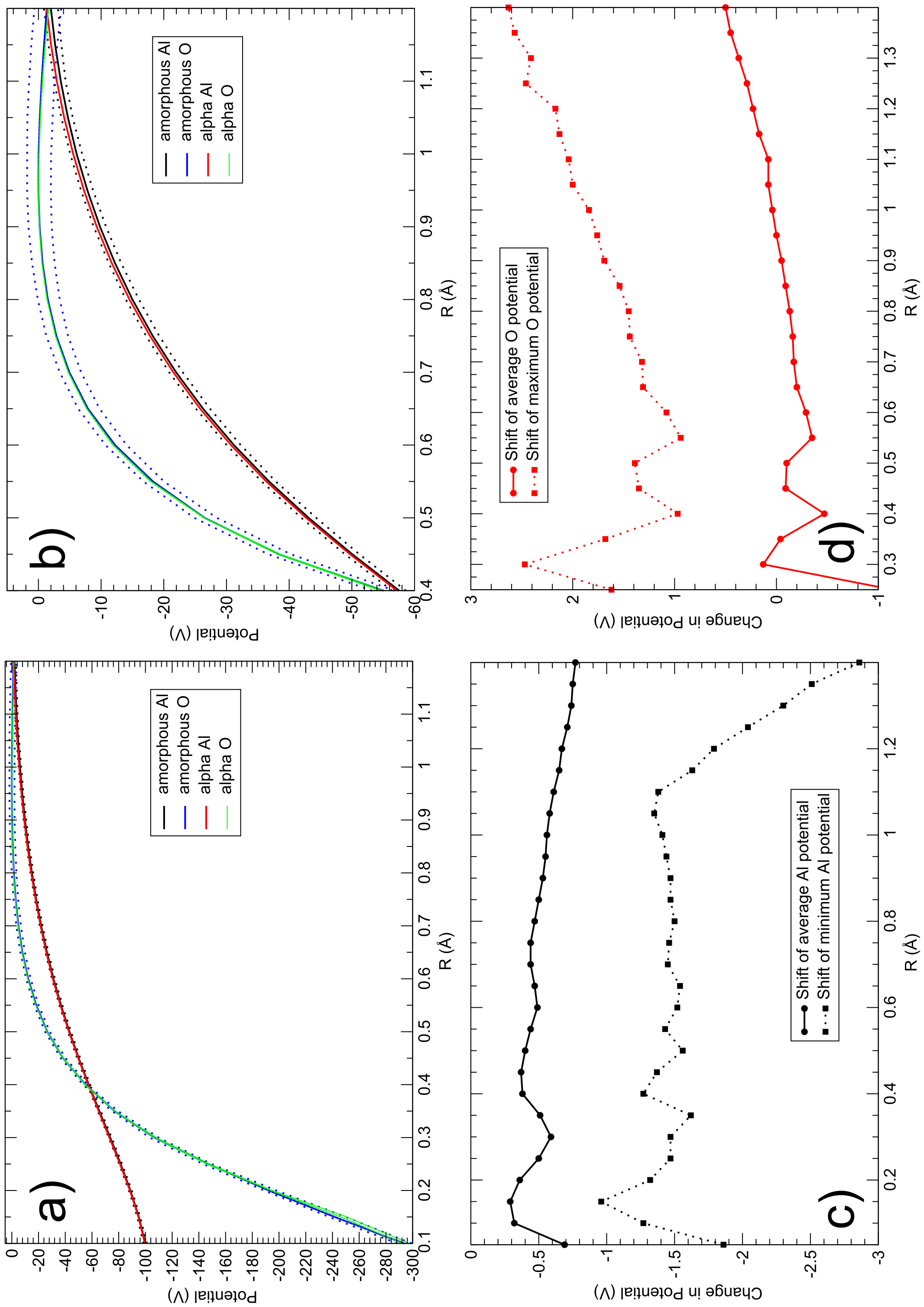

Figure 4.8: All graphs show properties of the spherically averaged electrostatic potentials of Al and O in a-Al$_2$O$_3$ and α-Al$_2$O$_3$, where for each phase the potentials have been zeroed with respect to the maximum value of the O potential which occurs at 0.95 Å. a) The electrostatic potential as a function of radial distance of Al and O in both phases, with dotted lines showing the maximum and minimum potentials. b) The same as in a) but with a scale so that the maximum and minimum can be distinguished. c) The average shift of the potential around Al, and the shift in the minimum potential at each radial distance, which affects the CBM. d) The average shift of the potential around O, and the shift in the maximum potential at each radial distance, as it will affect the VBM.

talline structures, shifted so that the maximum of the average electrostatic potential of O is at 0 V, which occurs for both structures at a radial distance of 0.95 Å, which will be referred to as 'zeroing'. This means that variations in potential between both phases, and the shifts between the O and Al potentials for each phase, can be compared. As can be seen in Fig. 4.8a and Fig. 4.8b the potential profiles between the amorphous and crystalline phase are very similar, with the O potential profile being much deeper and narrower as a result of its smaller ion size compared to Al, which has a shallower profile. An overall shift of less than 0.1 V is observed between the average crystalline and amorphous O potentials, meaning the average potentials after 'zeroing' have a very similar profile. However, the average Al potential of the amorphous system is 0.7 V (averaged over all radial positions) lower than that of the α-Al_2O_3 system after 'zeroing', which suggests the conduction band will shift downwards in energy. Keep in mind that the shift of the Al potential is effectively measured with respect to the O potential in each system and so the absolute shift will still change the band gap, even if the oxygen maximum is not a good reference point between the 2 systems.

However, as can also be seen in Fig.4.8a and Fig.4.8b, there is a much wider range of electrostatic potentials in the amorphous, rather than the crystalline, structures. The range of potentials at each radial point vary by less than 0.2 V in the α-Al_2O_3 system, but the variations of the potentials in the amorphous system are an order of magnitude greater. First, examining the Al potential, which is responsible for the position of the conduction band minimum, Fig. 4.8c shows that the minimum values of the electrostatic potentials lie, on average, 1.6 V lower in the amorphous systems than in the crystalline. This would suggest there is a lowering of the conduction band of approximately 1.6 V due to the change in the electrostatic potential environment as a result of the decrease in the Al coordination number. Fig. 4.8d shows a change of approximately 1-1.5 V in the highest O potential at the maximum electron distribution radius of O (at approximately 0.4 Å) between the amorphous and crystalline systems,which will shift the position of the valence band upwards. The maximum potentials correspond to the highly localized 2 coordinated sites responsible for the top of the valence band, and when combined with the Al potential shift downwards, explains the 3.3 eV reduction in the HOMO-LUMO gap. Thus the data suggests that the change in coordination and bonding character of Al and O also affects the electrostatic potential environment and causes the conduction band to shift down by approximately 1.6 eV and the valence band to shift upwards by 1.5 eV. However, experimentally the valence band shift is not as easily observed as the states are more highly localized at the VBM than at the CBM, which is due to the difference in localization between the O $2p$ orbitals and the Al $3s$ orbitals.

4.4 Conclusion

Using an MD melt and quench approach, amorphous alumina structures have been generated that reproduce experimental densities [24, 33, 148], NMR measurements of coordination numbers [39] and the radial distribution functions from X-ray diffraction experiments [38]. Producing credible geometric structures of a-Al_2O_3 is a crucial step to understanding its electronic structure, and, for later chapters, investigating intrinsic charge trapping and the role of defects in the material.

To accurately model the electronic structure the functional was tuned so as to minimize deviation from straight line error, important for calculating not only the correct band gap, but also for minimizing over delocalization when studying polarons and defects. The functional was shown to reproduce the electronic structure of α-Al_2O_3 accurately, calculating the band gap as 8.6 eV.

DFT calculations of the a-Al_2O_3 structures showed that the HOMO-LUMO gap decreases to an average of 5.48 eV, with IPR analysis showing the valence band edge is highly localized, with the mobility edge lying approximately 1 eV below the HOMO. Analysis of the electronic structure showed that the reduction in Al coordination, from 100% $^{[6]}$Al in α-Al_2O_3 to 55% $^{[4]}$Al in a-Al_2O_3, shifts the electrostatic potential of the Al ions down approximately 1.6 eV, leading to the observed decrease in the band gap. There is also a shift of 1-1.5 eV upwards observed in the O electrostatic potential, though the highest potentials correspond with the highly localized σ^*_{2p} states, which are not as easily observed experimentally. This chapter provides theoretical support for the findings in ref. [35] that a shift in the conduction band leads to the decrease in the band gap of a-Al_2O_3.

Chapter 5

Intrinsic charge trapping in crystalline and amorphous Al_2O_3

5.1 Introduction

As stated earlier, a-Al_2O_3 is an important high-*k* gate dielectric in a variety of transistor devices [22–24,109]. Performance of the dielectric in gate stacks is dependent on properties such as the band offset, which was covered in the previous chapter, and the trapping of charge. Trapped charges can affect device mobility or shift transistor threshold voltages [109]. Both positive [160] and negative [22] charging have been measured in a-Al_2O_3 films, though the exact nature of the charge traps remains unknown. Whilst charge trapping in dielectrics can be both advantageous and detrimental, either way it significantly affects the performance of devices and must be controlled. However, surprisingly little is still known about intrinsic electron and hole trapping in amorphous oxides, especially a-Al_2O_3. This chapter investigates whether intrinsic electron and hole polaron trapping is present in crystalline and amorphous alumina, and whether it is responsible for the observed charging.

Self-trapped hole (STH) polarons have already been theoretically predicted in crystalline α-Al_2O_3 using both intermediate neglect of differential overlap (INDO) [161] and DFT methods [162]. The hole polaron self-trapping energy (the energy difference between the fully delocalized and localized hole states) has been predicted using the hybrid functional HSE06 [60–62] at 0.13 eV [162]. Similarly small hole trapping energies have been predicted for many crystalline oxides, such as monoclinic ZrO_2 and HfO_2 [163, 164], $BaZrO_2$ [165] and several others (see e.g. [162,166]). Unfortunately experimental verification of these predictions is often challenging and there are no reliable experimental data demonstrating hole polaron formation in α-Al_2O_3.

However, experimental data [167, 168] and recent calculations suggest that structural disorder in amorphous oxides, such as a-SiO_2 [124, 131, 169] and a-HfO_2 [28], facilitates intrinsic electron and hole trapping in much deeper states than in the corresponding crystalline phases with trapping energies of about 1.0 eV. The wide applications of amorphous Al_2O_3 films prompted consideration of whether this is also the case in these films. They have a similar O $2p$ nature of the top of the valence band but a different character of disorder to the amorphous SiO_2 formed by a continuous random network of SiO_4 tetrahedra. Recent spectroscopic measurements of charge trapping in thin alumina films [111] have attributed states in the band gap to intrinsic hole polaron trapping and suggested that localized O $2p^5$ states are spread throughout the band gap rather than forming a relatively narrow band discussed in amorphous SiO_2 [131,169] and HfO_2 [28].

First, in order to test the DFT setup from the previous chapter, including the PBE0-TC-LRC [40] functional with the tuned cutoff, the properties of the Mg_{Al} defect in α-Al_2O_3 were calculated and compared to experiment. Then, using the geometries from the previous chapter, polarons and bipolarons were studied by introducing electrons and holes into both crystalline and amorphous alumina structures, and their properties calculated. These calculations demonstrate that there are no intrinsic electron traps in both crystalline and amorphous alumina. However, holes self-trap in crystalline α-alumina with trapping energies of 0.38 eV and trap at intrinsic precursor sites in amorphous alumina with an average trapping energy of about 1.3 eV. The energy barriers for hole hopping were calculated using the nudged elastic band (NEB) method. Finally, hole bipolarons are shown to trap in a-Al_2O_3, though their barriers for formation are over 1 eV in height.

5.2 Methodology

Intrinsic hole and electron trapping was investigated with the same 10 amorphous geometries that were used in chapter 4 for the analysis of the electronic structure of a-Al_2O_3. Electrons or holes were introduced to the crystalline and amorphous systems and then full geometry relaxations were performed using DFT. The DFT calculations were carried out using the same parameters as outlined in section 4.2.2, most crucially using the PBE0-TC-LRC [40] functional with a cutoff radius of 3.0 Å. As has already been discussed, tuning the functional so that DSLE is minimized also corrects for over or under delocalization and so better describes localized polaron states (section 4.2.2.1) . Calculations of the barriers for hole hopping and bipolaron formation were carried out using the nudged elastic band (NEB) method [68], whose theory is outlined in section 2.4.

5.3 Results

5.3.1 Properties of the Mg_{Al} defect

Due to low trapping energies, it is difficult to measure the properties of self-trapped hole polarons in α-Al_2O_3 experimentally. Instead the DFT setup and tuned functional can be benchmarked against the optical absorption [170] properties of the Mg_{Al} defect, and local structural information determined from EPR [171,172] measurements. Originally it was assumed that Mg acts as an acceptor [173], with the hole localizing on the nearest neighbour oxygen and becoming O^-, which makes it a good test system for hole trapping. However there is disagreement on the geometry of the defect, previous INDO calculations [161] suggested that the hole localizing over two O ions is more energetically favourable.

The calculations presented here show that the compensating hole localizes predominantly on one O ion (a spin of 0.76 from Mulliken analysis), as can be seen in Fig. 5.1. This localization is accompanied by a large elongation of the Mg-O bonds by 0.4 Å from the original perfect lattice positions. The three nearest neighbour Al ions that lie in the same plane as the O^- displace away from the O atom by less than 0.1 Å (see Table 5.1).

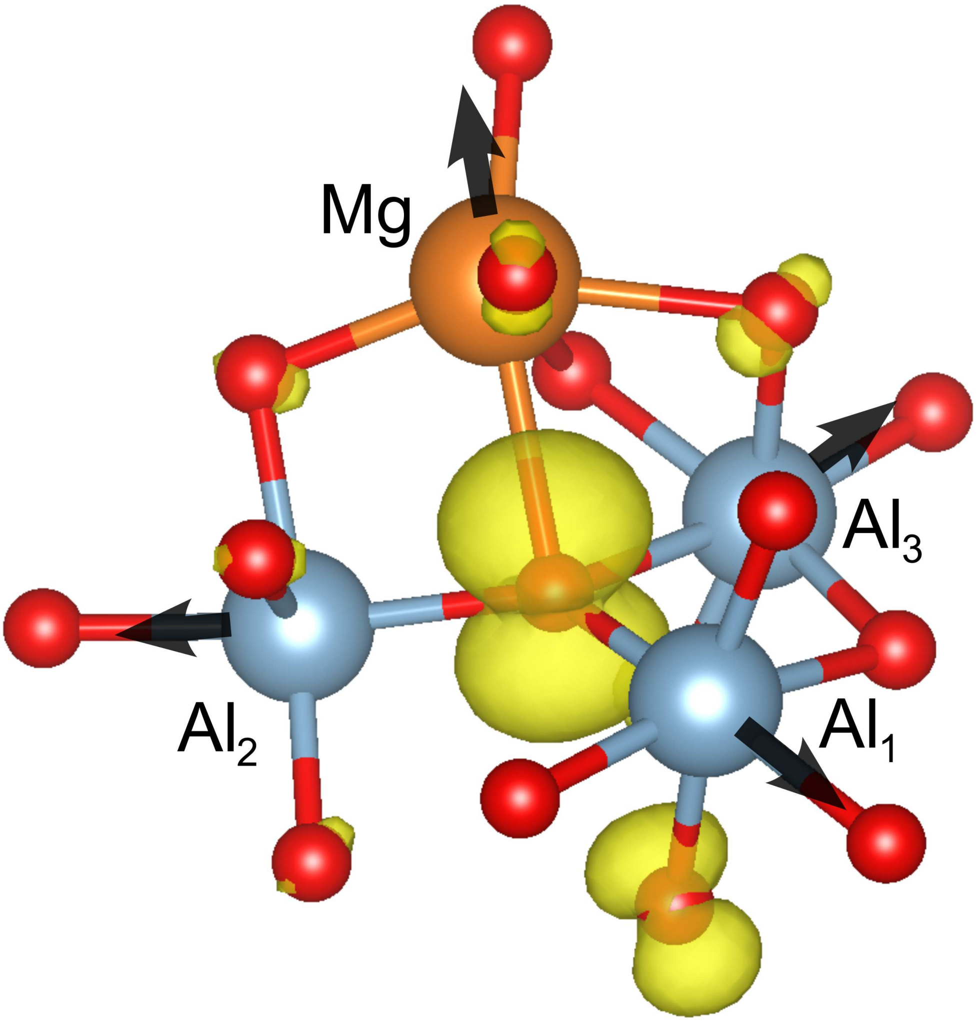

Figure 5.1: The spin density of the Mg_{Al} defect, where the hole is predominantly localized on one O ion. Mg is brown, O red and Al blue. The arrows show the direction of cation relaxation.

Using the relaxed geometry calculated with the PBE0-TC-LRC [40] functional, calculations of the hyperfine splitting are then used to confirm the defect geometry by comparison with EPR experiments [171, 172]. Calculation of the hyperfine splitting was performed using the PBE functional, due to convergence issues with PBE0-TC-LRC [40]. The PC-1 [174, 175] all electron basis set was used for the hyperfine calculations. These are also compared to hyperfine calculations performed using the HSE06 [60, 61] hybrid functional and the PCJ-0 [175–177]

Atom X	Isotropic hyperfine (MHz)			O-X distance (Å)	
	PBE	HSE06	Exp. [172]	Calc.	Ref. [173]
Al_1	15.27	18.91	19.03	1.888	1.834
Al_2	11.59	13.85	14.18	1.942	1.917
Al_3	4.31	9.12	7.29	2.062	2.104
Mg	1.21	2.06	-	2.353	-

Table 5.1: The calculated isotropic hyperfine parameters of the Mg_{Al} defect as well and the experimental ENDOR values [172]. It also shows the nearest neighbour distances to the oxygen where the hole localizes and compares them to the original predictions from theory [173]. The atom labels are from Fig. 5.1.

all electron basis sets[1]. The calculated isotropic hyperfine splitting for the nearest neighbour Al to the hole centre are shown in Table 5.1 and are compared to the experimental ENDOR measurements [172]. These results agree well with the experimental results, confirming the defect geometry and that a single O traps a hole when an Mg_{Al} defect is introduced, and that the PBE0-TC-LRC functional is able to accurately predict the structural relaxation of the site. The difference in the values of the calculated hyperfine splitting between PBE and HSE06 is most likely due to the over delocalization of the PBE functional, where the spin on the oxygen is only 0.54 (from Mulliken analysis). The EPR calculations also agree qualitatively with Adrian et al. [173] whose semi-empirical model of the defect predicts a strong dependence of the hyperfine constant on the O-Al distance.

The unoccupied K-S LUMO energy level of the Mg_{Al} defect, calculated using the tuned PBE0-TC-LRC functional, lies 2.15 eV above the VBM. Time-dependent DFT (TDDFT) calculations [178] of the optical absorption of this defect demonstrate a broad spectrum with the maximum at 2.4 eV as a result of transitions from the valence band states into the LUMO state. This can be compared with the optical absorption spectrum reported by Wang et al. [170] which has a maximum at 2.6 eV with a full width half maximum of 1.3 eV that they associate with the Mg_{Al}

---

[1] With thanks to Dr. Jonathon Cottom, who collaborated with me on the hyperfine calculations, and who performed the calculations using the HSE06 functional.

defect. The presence of the Mg_{Al} defect in the samples was confirmed by ESR measurements.

These results demonstrate that the tuned PBE0-TC-LRC functional performs well in predicting the correct geometries and defect levels for perfect crystalline alumina and also allows positive identification of the Mg_{Al} defect in α-Al_2O_3. This gives confidence when considering intrinsic polarons in crystalline and amorphous alumina.

5.3.2 The hole polaron in α-Al_2O_3

Intrinsic hole polarons in crystalline α-Al_2O_3 have been studied theoretically using classical and INDO methods [161]. Zhukovskii et al. [161] investigated whether self trapped hole (STH) polarons are more stable when localized on a single O or over two O ions, concluding that two-site holes are more stable. They calculated trapping energies to characterize the stability of the holes, however, the INDO method leads to a large over-estimation of these energies, in the order of 3-5 eV. The trapping energy, E_{trap}, is defined as

$$E_{\text{trap}} = E_{\text{neutral}}(N-1) - E_{\text{polaron}}(N-1) \tag{5.1}$$

where $E_{\text{neutral}}(N-1)$ is the total energy of the unrelaxed cell in the neutral geometry with a delocalized hole in the valence band and $E_{\text{polaron}}(N-1)$ is the total energy of the fully relaxed cell with a hole polaron. The definition of the trapping energy in equation 5.1 is directly comparable to the trapping energies calculated in previous papers [161, 162].

More recently, DFT calculations using HSE06 [60,61] have calculated the trapping energy of hole polarons to be 0.13 eV [162], with the majority of the spin density located on a single oxygen. This result is reproduced here using the HSE06 functional (see Table.4.3).

The tuned PBE0-TC-LRC functional predicts that the introduction of a hole to the system also results in self-trapping, with 0.8 of the spin (from Mulliken analysis) localized on a single O ion (see Fig. 5.2). The calculated trapping energy of

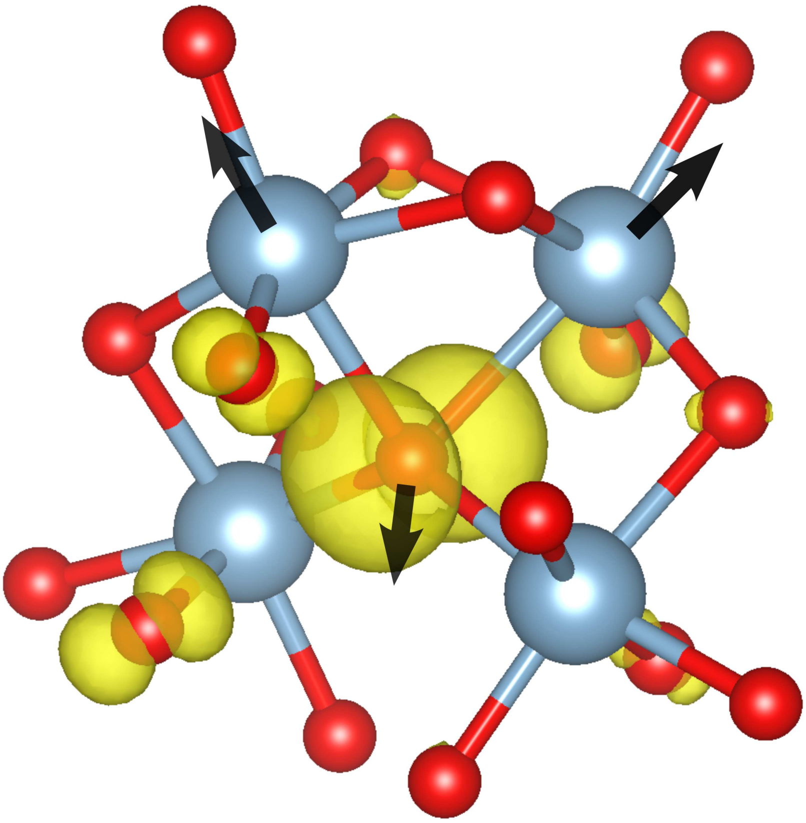

Figure 5.2: The spin density of the hole polaron in α-Al_2O_3, and the direction of relaxation of the ions. The Al ions are coloured blue and the O are red.

the hole polaron in α-Al_2O_3 is 0.38 eV. Hole localization is accompanied by displacements of the surrounding ions, with three of the four Al-O bonds elongating by approximately 0.1 Å, and the elongation of one Al-O bond by 0.3 Å. As the top of the valence band of α-Al_2O_3 is composed O $2p$ orbitals, the dispersion of the band is small, meaning that the increase in kinetic energy of the hole upon localization is smaller than the energy of the lattice relaxation, resulting in the high trapping energies. The calculated trapping energy is larger than that using HSE06 calculated both here and in previous papers [162], likely because the functional more strongly localizes the hole, and includes a larger contribution of exact exchange than HSE06. It can be seen from Table 4.3 that HSE06 does not perform as well as PBE0-TC-LRC in reproducing the correct band gap, which could be as a result of over delocalization.

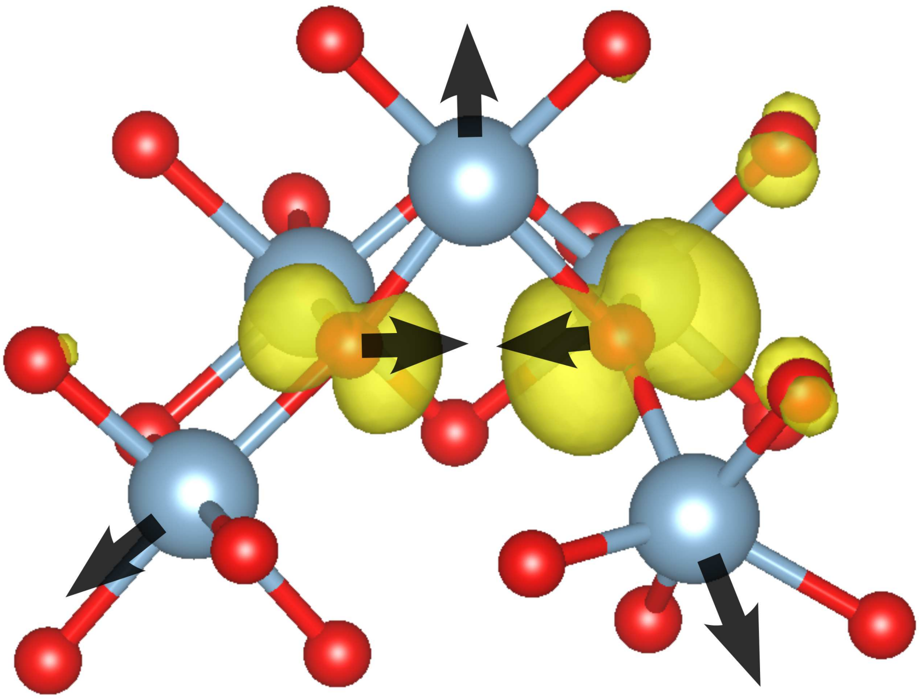

Figure 5.3: The spin density of the hole polaron in a-Al_2O_3, and the direction of relaxation of the ions. The Al ions are coloured blue and the O are red.

5.3.3 Hole polarons in a-Al_2O_3

The states with high localization at the top of the valence band (Fig. 4.5b) in the charge neutral systems correspond with local structural features that result in hole trapping, defined as ‘precursor sites’ for the purposes of this work. When a hole is introduced to the system it will spontaneously localize at one of the precursor sites predicted from the IPR. In all 10 amorphous structures of Al_2O_3 strong intrinsic hole trapping is observed, with an average trapping energy of 1.26 eV. The range of trapping energies is calculated to be 1.0-1.5 eV (see Table 5.2). The much larger trapping energies observed in the amorphous structures when compared to the crystalline is most likely due to the under-coordination of the O atoms, where over 80% are 3-coordinated with Al, rather than 4-coordinated as in α-Al_2O_3. Many of the precursor sites where the hole polarons are able to localize include a 2 coordinated O ion (see Table 5.2), which account for approximately 5% of oxygens in the amor-

Sample	Trapping energy (eV)	Unrelaxed O-O distance (Å)	Relaxed O-O distance (Å)	O coordination number
1	1.16	2.61	2.23	2
2	1.00	2.61	2.39	3
3	1.39	2.55	2.37	3
4	1.49	2.68	2.12	2
5	1.32	2.46	2.47	2
6	1.10	2.91	2.61	2
7	1.34	2.41	2.10	3
8	1.42	2.65	2.53	2
9	1.08	2.69	2.59	2
10	1.29	2.69	2.39	2

Table 5.2: The properties of different hole trapping sites in the 10 geometry samples of a-Al_2O_3, including the coordination number of the oxygen where the majority of the spin is localized.

phous structure, but whose σ_{2p}^{*} like states disproportionately contribute to the top of the valence band, as discussed in section 4.3.3. However not all precursor sites include a 2 coordinated oxygen, with the hole occasionally localizing on 3 coordinated O sites.

Although the precursor sites are most easily identified from the IPR data, there are stuctural similarities between the hole traps. Unlike in α-Al_2O_3 where the hole localizes on one O ion, in a-Al_2O_3 over 90% of the spin density localizes on 2 nearest neigbour O ions (see Fig. 5.3) with an average O-O separation of 2.6 Å before relaxation (see Table 5.2). This means the hole traps have a local structure involving multiple ions. The spin density is not, however, evenly distributed between the 2 oxygens, one normally accounts for 0.7 of the spin (from Mulliken analysis) with the other approximately 0.2. This is due to the filling of only one of the unoccupied σ_{2p}^{*} anti-bonding type orbitals with a hole, which results in an asymmetry of the wavefunction and unequal charge distribution between the 2 oxygens, as can be seen in Fig. 5.3. The asymmetry results in breaking the degeneracy of the σ_{2p}^{*} levels, with the hole state being pushed into the band gap. Between the 2 O ions, where the hole is localized, there is a large contraction of the O-O bond of 0.3-0.4 Å, much larger than the relaxation of the O-O bonds in the crystalline system which are less than 0.1 Å, and most likely due to the removal of an electron from an anti-bonding orbital and the decrease in Coulomb repulsion. The O-Al-O bond angle also decreases by an average of 10°. Accompanying this is also a small displacement of the Al ions, which move approximately 0.1 Å.

Due to the large distribution of bond angles and bond distances in a-Al_2O_3 there are multiple precursor sites where the local structural configuration of the ions allows for hole trapping. These precursor sites are identified using the IPR data, and hole polarons can be localized at different sites within the cell. In a-Al_2O_3 there are an average of 3-4 precursor sites per 360 atom cell where hole polarons are able to trap, with an average separation of 8 Å between sites. This leads to a maximum density of precursor sites of approximately 2.6×10^{20} cm^{-3}. The variation of trapping energies of the precursor sites within the cell is similar to that between different samples, with a typical variation of 0.3 eV.

To prove that there are a number of precursor sites within a single cell, predicted using IPR, that can also trap holes, one of the 360 atom geometries was selected at random, and the trapping energies of different precursor sites calculated. This was achieved by identifying the oxygen ions contributing to the majority of the IPR of the 4 highest energy molecular orbitals at the top of the valence band (see Fig. 5.4), and then fixing all the atoms in the cell but those surrounding the target O and allowing the atoms to relax. After the initial localization of the hole on the target ion, all atoms were then un-fixed and allowed to fully relax so the correct trapping energy could be calculated. Hole polarons were successfully trapped at each precursor site identified from the IPR, with trapping energies ranging from 1.00-1.32 eV, similar to the distribution of trapping energies seen across the 10 different samples. This demonstrates the effectiveness of using IPR analysis to identify precursor sites in amorphous materials, and increases the confidence with which we can predict the density of precursor sites.

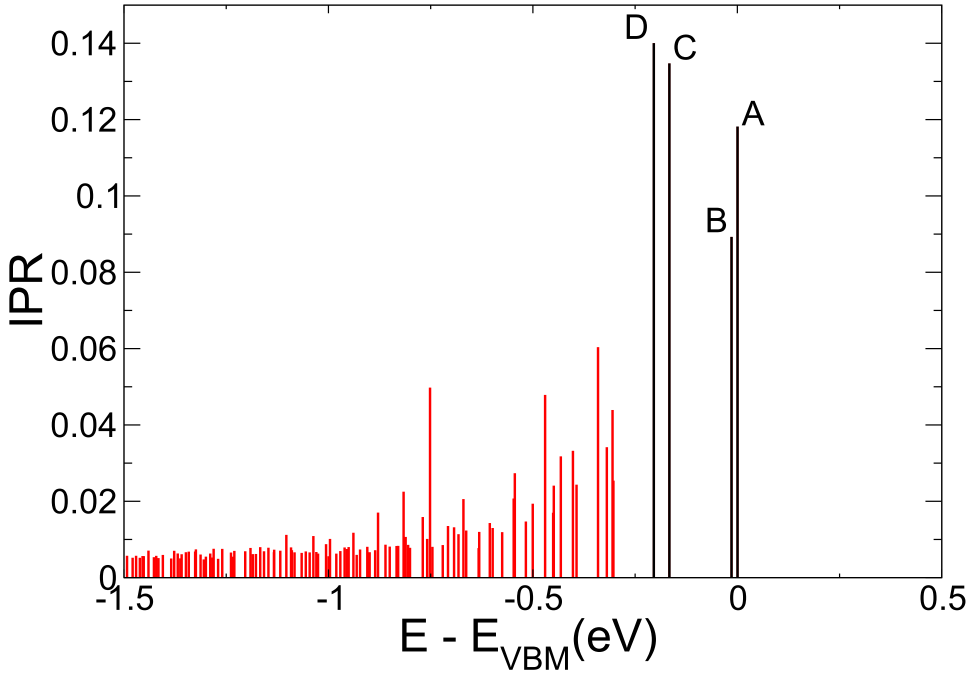

Figure 5.4: The IPR of the top of the valence band in a single amorphous geometry. The 4 highest energy molecular orbitals in the valence band have been labelled A, B, C and D. Hole polarons have been localized at each of the precursor sites identified from the molecular orbitals.

MO	Trapping energy (eV)	Unrelaxed O-O distance (Å)	Relaxed O-O distance (Å)	O coordination number
A	1.32	2.82	2.21	2
B	1.00	2.61	2.39	3
C	1.08	2.64	2.37	3
D	1.09	2.36	2.26	2

Table 5.3: The properties of 4 different hole trapping sites (labels correspond to MOs in Fig. 5.4) in the same geometry sample of a-Al_2O_3, including the coordination number of the oxygen where the majority of the spin is localized.

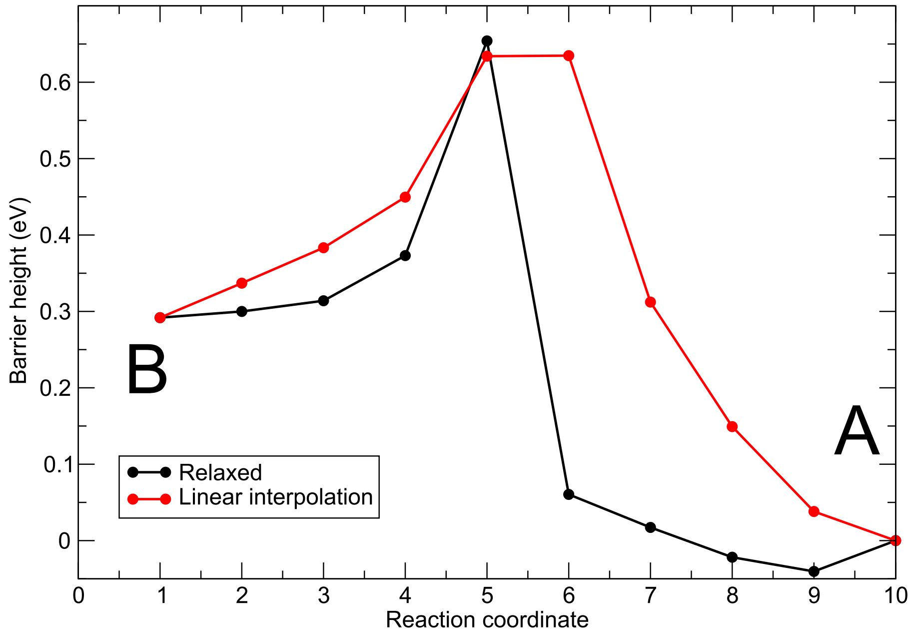

Figure 5.5: The energy barrier for a hole to hope from one precursor site to another, calculated using NEB.

5.3.3.1 The barrier to hole hopping

Having established that there are multiple hole trapping sites per cell, it is possible to investigate whether hole polarons in a-Al_2O_3 are mobile. Using a nudged elastic band calculation (NEB), with 10 images, the thermal barrier to a hole hopping between two hole trapping sites in the same cell can be calculated. The activation energy for hole hopping between sites A and B, defined in Fig. 5.4, was calculated to be 0.3-0.6 eV, as can be seen in Fig. 5.5. However, unlike in crystalline Al_2O_3 where adjacent hole trapping sites are equivalent, in the amorphous material precursor sites are separated by average distances of 8.0 Å, which would suggest that transport is more likely to be through a tunneling process. The activation energy for hole hopping is lower than the energy required to promote a hole into the delocalized region of the valence band past the mobility edge, suggesting there might be a transition from a hopping transport mechanism to conventional conduction at higher temperatures. The high trapping energies of hole polarons and barriers to hopping also suggest that there is likely to be stronger positive charging in a-Al_2O_3 than in the crystalline material, and that this charging could be due to intrinsic hole trapping rather than impurities in the material.

5.3.4 Electron trapping in Al_2O_3

Self trapped electron polarons in crystalline α-Al_2O_3 were not found to be stable. This is most likely, as stated earlier, due to the large dispersion of the conduction band at the Γ-point of α-Al_2O_3 [158], the small relaxation of the lattice cannot compensate for the large increase in kinetic energy of the electron as it is localized and so the polaron is not self trapped.

Although deep electron traps in a-Al_2O_3 have been observed experimentally [22], after examining 30 different geometric structures (20 of them 120 atom models) no significant evidence for intrinsic electron trapping was observed. Extra electrons are delocalized at the bottom of the conduction band. The IPR of a-Al_2O_3 in Fig. 4.5b suggests the reason for the much lower density of electron traps when compared to hole traps is there are no localized precursor sites at the bottom of the conduction band. In materials which show strong intrinsic electron trapping, the bottom of the conduction band generally has lower dispersion and is composed of orbitals that are more directional. In the case of HfO_2 [28], the CBM is composed of *d* orbitals and demonstrates electron trapping energies of 1.4 eV, and even the formation of electron bipolarons. In a-Se photodetectors [179] it is reported that an a-HfO_2 blocking layer is more effective at suppressing both electron and hole injection than an a-Al_2O_3 layer. The greater number of charge traps in HfO_2 could suggest that while pure alumina does trap charge, it only traps holes.

5.3.5 Hole bipolarons

Having established that single hole polarons have high trapping energies in a-Al_2O_3, it is interesting to consider whether 2 holes can trap at the same site and form a hole bipolaron. As there are a high density of hole precursor sites, the stability of a hole bipolaron has to be compared to the stability of 2 holes occupying separate sites in

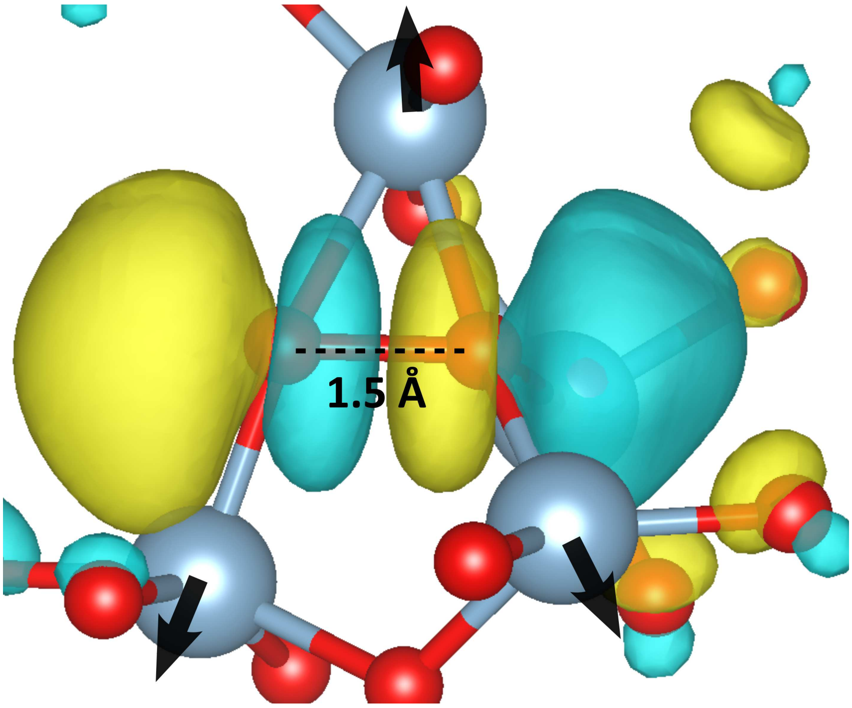

Figure 5.6: The local geometry of the bipolaron and the isosurface of the unoccupied molecular orbital associated with the bipolaron. The arrows display relaxation direction of the Al ions.

the system. The binding energy of the hole bipolaron, E_{B}, is therefore defined [180]

$$E_{\mathrm{Binding}} = 2E_{\mathrm{Polaron}}(N-1) - [E_{\mathrm{Bipolaron}}(N-2) + E_{\mathrm{Neutral}}(N)] \,, \tag{5.2}$$

where N is the number of electrons in the neutral system, $E_{\mathrm{Polaron}}(N-1)$ is the energy of the fully relaxed system with a single trapped hole polaron ($N-1$ electrons), $E_{\mathrm{Bipolaron}}(N-2)$ is the fully relaxed system with the hole bipolaron and $E_{\mathrm{Neutral}}(N)$ is the energy of the neutral system. The binding energy is therefore the difference in energy between a system with two infinitely separated hole polarons, and a system where the two holes have combined to form a bipolaron.

When 2 holes are introduced to the a-Al_2O_3 system they do not immediately localize on the same site, but instead occupy different hole precursor sites. This is a result of the energy barrier that must be overcome for hole bipolarons to form. Trapping 2 holes at the same site is achieved by decreasing the bond length between 2 oxygen ions at a hole precursor site to approximately 1.5 Å, and then allowing the

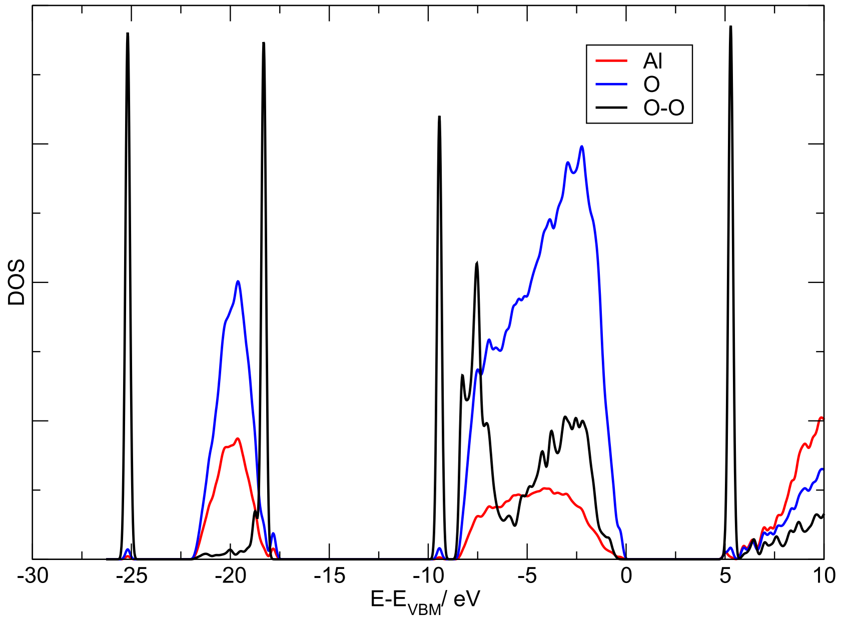

Figure 5.7: The projected density of states (PDOS) of the bipolaron in a-Al_2O_3, with the black peaks showing the states of the O-O dimer. The density of states projected onto the 2 nearest neighbour oxygen where the bipolaron localizes has been normalized to O density.

system to relax. The binding energy of hole bipolarons is not always positive, with binding energies ranging from -0.71 to 0.37 eV, with the average binding energy over 8 samples being negative. This means that having 2 holes occupying separate trapping sites is often a lower energy configuration than that of a bipolaron. This differs from amorphous HfO_2 where hole bipolarons form spontaneously [180] with no energy barrier to overcome, and have positive binding energies.

After the 2 nearest neighbour oxygen ions in the precursor site relax towards each other the bipolaron takes the form of an O-O dimer (see Fig. 5.6). The decrease in the bond length is significant, with the average O-O bond length contracting from 2.36 Å, for the single hole polaron, to 1.49 Å for the bipolaron. The hole bipolaron state, seen in Fig. 5.6, is similar to the unoccupied O σ_{2p}^{*} antibonding orbital of an O_2^{2-} molecule. As discussed in section 5.3.3, the single hole polaron has the majority of its spin density sitting on a single oxygen in the O-O dimer, breaking the degeneracy of the σ_{2p}^{*} unoccupied orbitals. The removal of another electron at the bipolaron site means both σ_{2p}^{*} orbitals are unoccupied, and the O-O bond distance contracts towards the bond length of an O_2^{2-} molecule. The density of states, shown in Fig. 5.7, show that the states of the O-O dimer are highly localized, and resemble the states of an O_2 molecule. The large relaxation of the O-O bond generally pushes the unoccupied bipolaron state into the conduction band, and there is very little mixing of the O σ^*_{2p} orbitals and the Al 3*s* orbitals that form the bottom of the conduction band. Sometimes however, the unoccupied bipolaron states sits in the band gap, just below the conduction band minimum. This differs from bipolarons in other metal oxides. In amorphous HfO_2 [180] some mixing of the σ^*_{2p} antibonding orbital and the Hf 5*d* orbitals at the conduction band minimum is observed, whilst in amorphous TiO_2 [181] almost complete hybridization of the bipolaron state with the Ti 3*d* orbitals occur so that no localization of the O-O antibonding state in the conduction band is observed. The hybridization of the O *p* type orbitals with the *d* orbitals of the transition metals that form the CBM means the bipolaron state is not as localized as it is in a-Al_2O_3, and therefore will never appear in the band gap.

5.3.5.1 The barrier for hole bipolaron formation

Using the nudged elastic band method, the energy barrier for bipolaron formation was calculated. A system with 2 hole polarons trapped at different precursor sites was used as the initial state, with the final state consisting of the 2 holes forming a bipolaron on one of the initial hole sites. The hole sites were chosen so that their individual trapping energies were within 0.1 eV of each other. 10 images were used in the calculation.

As can be seen in Fig. 5.8 the barrier height for bipolaron formation is 1.26 eV. The image corresponding to the transition state, at image 5, (see Fig. 5.9) clearly shows the hole occupying both the initial hole site and the bipolaron site, meaning that we can be confident that the maximum of the energy barrier is a good representation of the transition state. The 1.26 eV barrier for hole bipolaron formation is much higher than the 0.3-0.6 eV barrier height for hole hopping, meaning hole bipolarons are much more likely to form through a tunneling process. This is different to a-HfO_2 where bipolarons are likely to be a significant source of positive charge as there is no barrier to their formation [180].

That bipolaron formation has such a high energy barrier suggests that bipo-

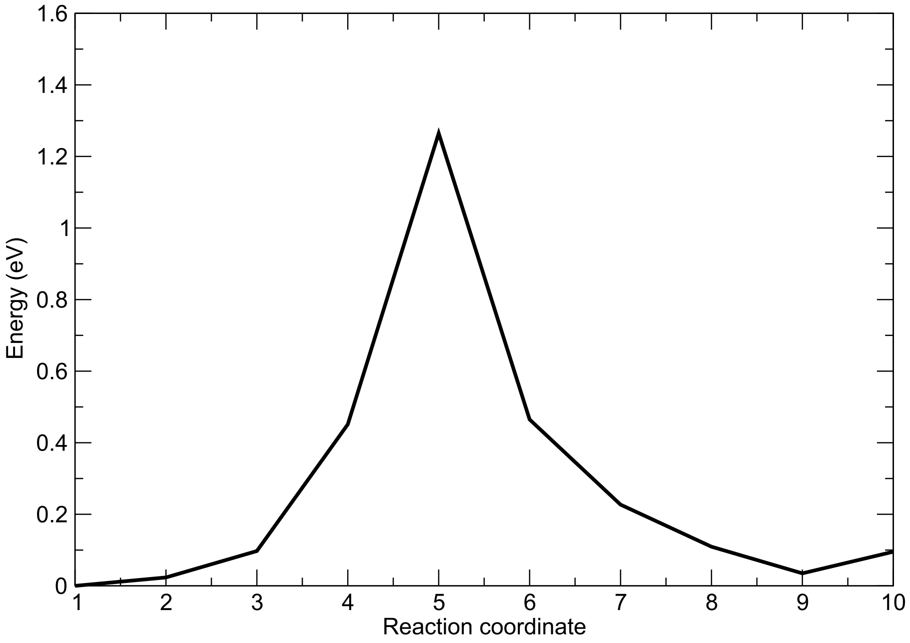

Figure 5.8: The energy barrier for a bipolaron to form from 2 separated hole polarons, where image 1 is the 2 separated hole polarons, and image 10 is the bipoalron.

larons are unlikely to significantly contribute to the positive charging of a-Al_2O_3, and that intrinsic single hole polarons are far more likely to be the cause of positive charging and hole trapping in the material.

5.4 Conclusions

Intrinsic charge trapping in amorphous alumina has been studied through the use of DFT simulations with the range-separated hybrid functional PBE0-TC-LRC. The truncation radius was tuned to provide the piece-wise linearity of the energy, as demonstrated in chapter 4. Satisfying this condition led to qualitatively correct predictions of electron and hole localization at impurities in other calculations [135, 138]. The performance of PBE0-TC-LRC with R=3.0 Å was tested by reproducing the spectroscopic properties of the Mg_{Al} defect in α-Al_2O_3. The substitution of Al by Mg in α-Al_2O_3 creates a local negative charge which is known to be compensated by a positive hole trapped on a nearby O ion. This defect has

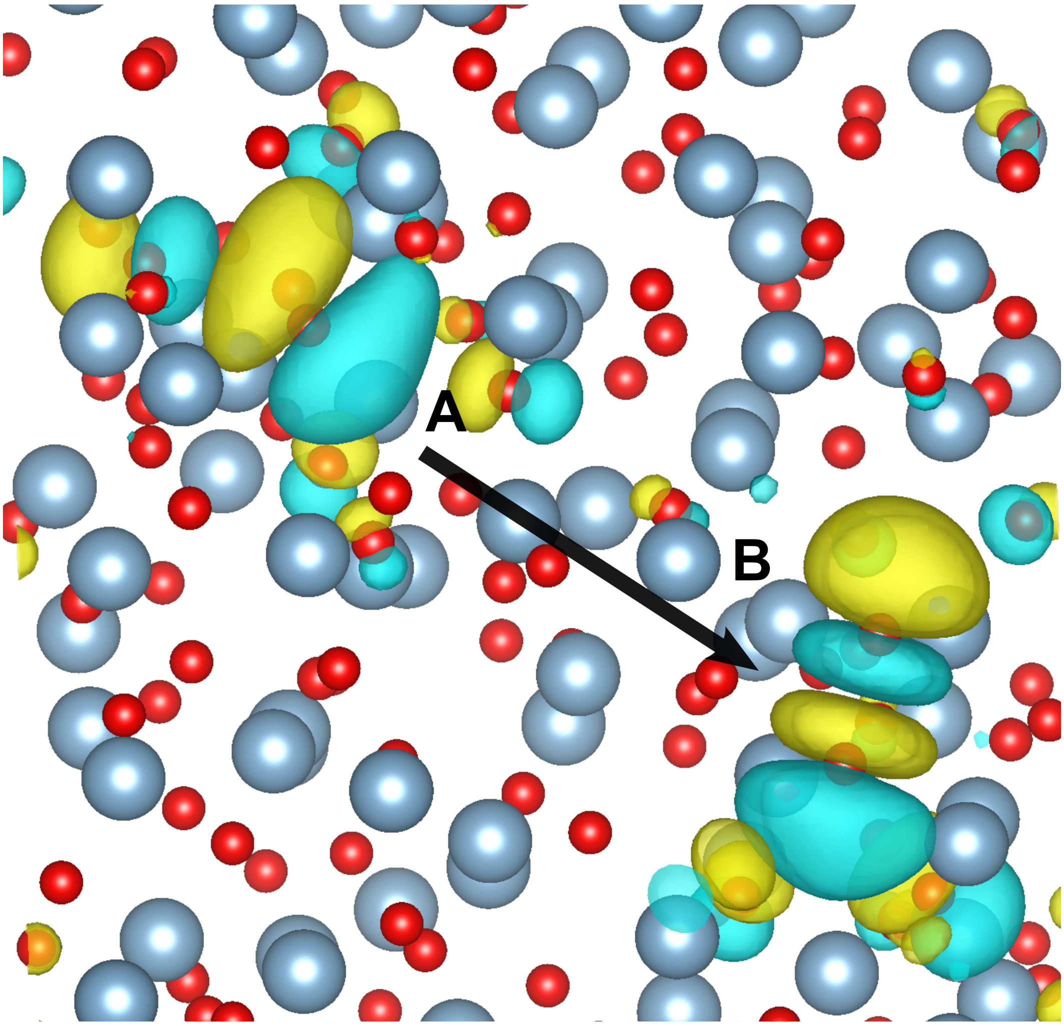

Figure 5.9: The molecular orbital isosurface of the hole in its transition state occupying both the single hole site (A) and the bipolaron site (B). This is from image 5 of the nudged elastic band calculation, the maximum of the energy barrier in Fig. 5.8.

been studied by EPR [171,172] and optical spectroscopy [170] and the calculations reproduce the spectroscopic properties of the Mg_{Al} defect in good agreement with experiment.

Using the tuned functional, it was shown that holes can trap spontaneously in amorphous alumina on two nearest neighbour oxygen sites, with an average trapping energy of 1.26 eV. It is also demonstrated that there is a high density of hole trapping precursor sites in a-Al_2O_3. These are typically low-coordinated O sites which are separated on average by about 8.0 Å. The binding energies of bipolarons were also calculated, and some bipolarons were shown to have positive binding energies. However, a nudged elastic band calculation predicted the activation barrier to formation to be greater than 1.2 eV, meaning they are unlikely to be a significant source of positive charging in a-Al_2O_3. Unlike in other oxides, such as SiO_2 and HfO_2, no electron trapping was observed in both crystalline and amorphous alumina. This is attributed to the orbital nature of the bands, with the CBM being composed of highly dispersed 3*s* states. This suggests that the nature of intrinsic trapping in metal oxides could be predicted by examining the fundamental orbital character of the ions in the system and the composition of the bands. These results predict that the trapping of positive charge can be much more severe and stable in amorphous alumina than in crystalline samples, and that they are more likely to be single hole polarons rather than bipolarons.

Chapter 6

Defects in a-Al_2O_3

6.1 Introduction

Significant negative charging of a-Al_2O_3 films is observed experimentally [22, 23, 41, 42], but, the defect, or defects, responsible have not yet been identified. In this chapter the characteristics of a variety of defects are investigated using DFT, in order to identify the defect responsible for electron trapping in amorphous Al_2O_3.

The experimental data [22, 23, 33, 41, 42, 182, 183] in conjunction with the computational results presented in this chapter will enable the positive identification of defects present in a-Al_2O_3. Measurements of the shifts in threshold voltage in a-IGZO thin film transistors estimate the density of defects that trap electrons to be $1\times10^{13}/\text{cm}^2$ in a 30 nm a-Al_2O_3 'charge trapping' layer [23] in the device.

Another detailed examination of electron trapping in Al_2O_3 thin films [22], measures the trap density at various depths within the film and the position of their energy levels below the conduction band minimum (CBM) using photodepopulation spectroscopy (PDS). PDS measures the energy levels of the defects by observing the current in the film after the photoexcitation of electrons into the Al_2O_3 conduction band. After significant charging of the alumina films by electron injection, PDS measurements show a broad range of electron trap energy levels 2.9-3.7 eV below the CBM (see Fig. 6.1), with a trap density of $1.3\times10^{19}/\text{cm}^3$, near the SiO_2/Al_2O_3 interface [22]. As can be seen in Fig. 6.1, before electron injection the film is uncharged and much lower PDS signal intensities are exhibited, suggesting a much

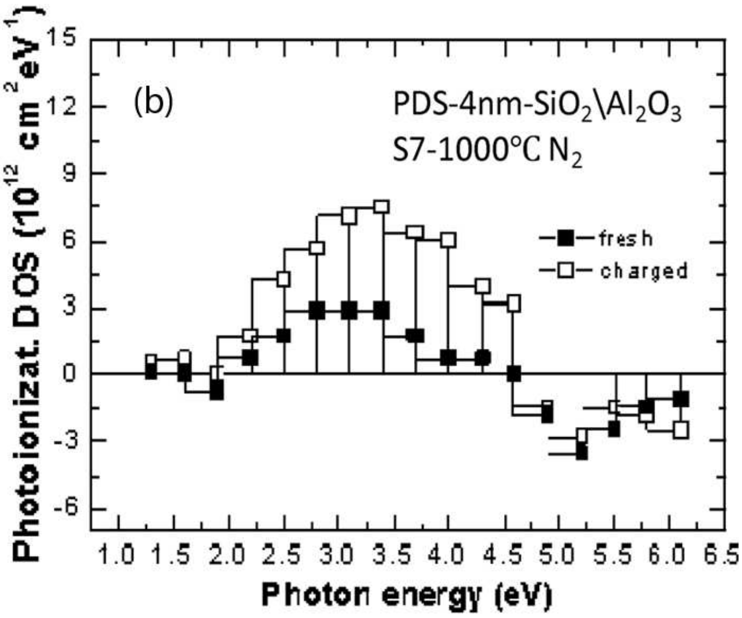

Figure 6.1: The energy distribution of the electron traps with respect to the conduction band minimum in an a-Al_2O_3 thin film, measured by PDS, for a charge neutral film before electron injection (black squares) and a negatively charged film after electron injection (white squares). ©2010 IEEE. Reprinted, with permission, from [22]

lower density of occupied gap states.

To identify these traps, as a first approximation of the photoexcitation energy, the energy difference between the Kohn-Sham energy levels of the defects and the conduction band can be compared to the PDS trap levels. TDDFT calculations have demonstrated that the excitation energies of transitions from localized defect states into delocalized band states in amorphous materials can be well approximated by the Kohn-Sham energy eigenvalue differences of the states [184]. In chapter 4 it is shown that the conduction band minimum of a-Al_2O_3 is a delocalized state, and does not exhibit the localization seen in other oxides [28]. High electron mobilities in a-Al_2O_3 have also been measured experimentally [42]. As PDS detects transitions by measuring a current, it is important that the energy reference is taken from the mobility edge, which in a-Al_2O_3 corresponds to the CBM [42].

The PDS measurements are confirmed by ‘gate side trap spectroscopy by charge injection and sensing’ (GS-TSCIS) measurements which show a peak defect density of $1.6 \times 10^{19}/\text{cm}^3$ at approximately 3.4 eV below the Al_2O_3 CBM, with a significant distribution of traps from 3.0 eV below the CBM [22]. A shallow band of traps is also identified at 1.6-1.8 eV below the CBM, with a trap density of approximately $1.6 \times 10^{19}/\text{cm}^3$ in the bulk of the Al_2O_3 films [22].

As discussed in chapter 5, intrinsic trapping of electron polarons through structural distortion of stoichiometric a-Al_2O_3 is not observed, and it is therefore unlikely to be responsible for the negative charging seen in experiment [22,23]. However, a-Al_2O_3 films also contain defects where the structure deviates from the stoichiometric 'pure' amorphous topology, analagous to intrinsic and extrinsic defects in crystalline Al_2O_3. The interest in alumina's potential as a gate dielectric means defects in the crystalline material have been widely studied computationally [185–189]. When building metal-oxide-semiconductor devices it is important to understand whether various defects will introduce in-gap states that can act as charge traps at the semiconductor interface, or as shallow donors which will contribute to leakage current.

In this chapter the structural and electronic properties of interstitial hydrogen (H_i), oxygen vacancies (V_O), oxygen interstitials (O_i), aluminium vacancies (V_{Al}) and aluminium interstitials (Al_i) in a-Al_2O_3 are discussed. Of particular interest are the charge transition levels and Kohn-Sham energy levels of the defects. This is to enable identification of the defects responsible for the negative charging of a-Al_2O_3 films by comparing the computational results with the experimental trap spectroscopy data [22].

6.2 Methodology

A range of defects in a-Al_2O_3 were investigated with the same 10 amorphous geometries used previously (see chapter 4). Defects were then created in the 360 atoms cells of both a-Al_2O_3 and α-Al_2O_3 by the addition or removal of an ion at a variety of sites, in order to sample the effect of different densities, band gaps and local atom coordination numbers. The structures were then allowed to undergo full geometry optimization and the electronic structure calculated using the DFT parameters described in section 4.2.2, most crucially using the PBE0-TC-LRC [40] functional with a cutoff radius of 3.0 Å.

6.2.1 Sampling defects in amorphous material

In all crystals there is a finite number of non-equivalent defect sites within the primitive unit cell. It is therefore possible to calculate all configurations of a single type of defect in crystalline systems. In amorphous structures the lack of periodicity means no sites are exactly equivalent, and so any defect properties will fall within a range of values, dependent on local geometric structure and the bulk properties of the specific amorphous cell.

Different methods have been employed to sample defects in amorphous materials. One method involves sampling a variety of defect sites within a single amorphous cell [190]. This allows defect sites with different nearest neighbour configurations and bond lengths to be investigated, without having to generate a large number of amorphous geometries. However, this does mean that the range of values of the defect properties are dependent on the geometry of one cell, which may not be representative of a true amorphous material. The coordination number distribution, density, average bond length and band gap can all vary between amorphous cells, which can affect the relaxation and stable charge states of defects.

The other approach is to calculate the properties of defects in a range of different cells [191, 192]. This allows a variety of local defect geometries to be sampled, which have different bond lengths and local coordination numbers, whilst also allowing for variation in bulk properties that can affect the stability of certain defect configurations and charge states. It is also less likely to be affected by anomalous cell geometries. This is the approach applied in this work, with a single defect studied in each of the 10 different amorphous geometries that were generated (see chapter 4). To create vacancies, atoms are removed at random, but so the distribution of the atom coordination numbers matches that of the distribution across the 10 cell geometries. Interstitial defects are created by adding an atom at a random position in the cell, with a consideration of minimum inter-atomic distances, and then performing a geometry relaxation.

This approach is still able to give a range of the defect charge transfer levels, Kohn-Sham levels and defect geometries, whilst also allowing any impact of the bulk properties to be investigated. Thus the general characteristics can be studied whilst also allowing the chance for less likely configurations to be discovered. Limited computational time means that only a finite number of configurations can be calculated, and so the properties observed are not a complete picture. However, even with 10 examples per defect, general patterns begin to appear and the distribution of properties observed.

6.2.2 Defect formation energies

The formation energies and charge transition levels of the defects investigated in this chapter were calculated using the method described in section 2.3. The chemical potential of hydrogen that is used in the calculation of the formation energies is given by the expression, $\mu_{\mathrm{H}} = E_{\mathrm{H}_2}/2$, where $\mathrm{E}_{\mathrm{H}_2}$ is the total energy of an H_2 molecule. The chemical potential of oxygen was taken to be $\mu_{\mathrm{O}} = E_{\mathrm{O}_2}/2$, where $\mathrm{E}_{\mathrm{O}_2}$ is the total energy of an O_2 molecule in the triplet state.

The aluminium chemical potential was calculated from a 256 atom cell of bulk Al in the cubic phase, after a full cell relaxation. The DFT calculation used the same functional and basis sets described in section 4.2.2.

Charge corrections to the energy, as a result of the interactions between point charges in periodic supercells [63, 65] (see section 2.3) were included in the calculations of the defect formation energies. The corrections led to small shifts in the positions of the charge transfer levels by no more than 0.4 eV, due to the high dielectric constant of amorphous Al_2O_3 (9.6 [193]) and the large size of the cells.

6.3 Results

6.3.1 Interstitial hydrogen

Due to its ubiquity and presence in almost every growth environment, hydrogen is a common impurity in most metal oxides and semiconductors, including Al_2O_3 [33, 182, 183]. Therefore it is not surprising that the negative charging observed experimentally [23, 183] in a-Al_2O_3 thin films has been attributed to interstitial hydrogen (H_i). An increase in tunneling conductivity via a mid-band gap state was observed to increase after an increase in the H content of alumina films [183]. DFT studies of H_i in crystalline Al_2O_3, using LDA [185], GGA [183] and hybrid [187–189] functionals, confirm that interstitial hydrogen has a mid-band gap energy level in alumina, close to its band offset with Si. Due to the lack of computational data on interstitial hydrogen in amorphous alumina, DFT studies of crystalline Al_2O_3 are used for comparison in this section.

To create the defects, neutral hydrogen atoms were positioned at random positions within the 10 amorphous Al_2O_3 geometries, while ensuring initial O-H distances were greater than 1.6 Å, and then allowed to relax. This allowed the H to be positioned close to O ions with a range of coordination numbers during relaxation. After calculating the properties of the H_i^0, the different charge states were investigated by the addition or removal of an electron to the system followed by a full geometry relaxation.

6.3.1.1 H_i^+

In crystalline alumina there 3 are possible charge states of interstitial hydrogen, each of which has different structural and bonding characteristics. Previous DFT calculations predict that H_i^+ forms an OH bond with a nearest neighbour oxygen in α-Al_2O_3 [187–189] and θ-Al_2O_3 [189], with O-H bond lengths of approximately 1.0 and 1.1 Å respectively. As can be seen in Fig 6.2a, the H_i^+ defect demonstrates similar behaviour in a-Al_2O_3 , with the proton forming an OH bond with a nearest neighbour oxygen. The average O-H bond length over the 10 amorphous samples is 1.00 Å, with a range of 0.96-1.07 Å.

Out of the 10 H_i^+ configurations in a-Al_2O_3, 7 formed an OH bond with a 2-coordinated O ion ($^{[2]}$O), and 3 with a 3-coordinated O ($^{[3]}$O). The under-coordination of the O ions means no Al-O bonds have to be broken to form the lowest energy configurations of the defect. This can be compared to hybrid functional calculations of α-Al_2O_3 [189], where 2 of the 4 oxygen ion's Al-O bonds are broken to form the OH configuration, whilst in θ-Al_2O_3 the proton bonds with a 3-coordinated O and no O-Al bonds are broken. The H_i^+ defects in a-Al_2O_3 where the OH bond includes a $^{[2]}$O have an average formation energy that is 0.9 eV lower

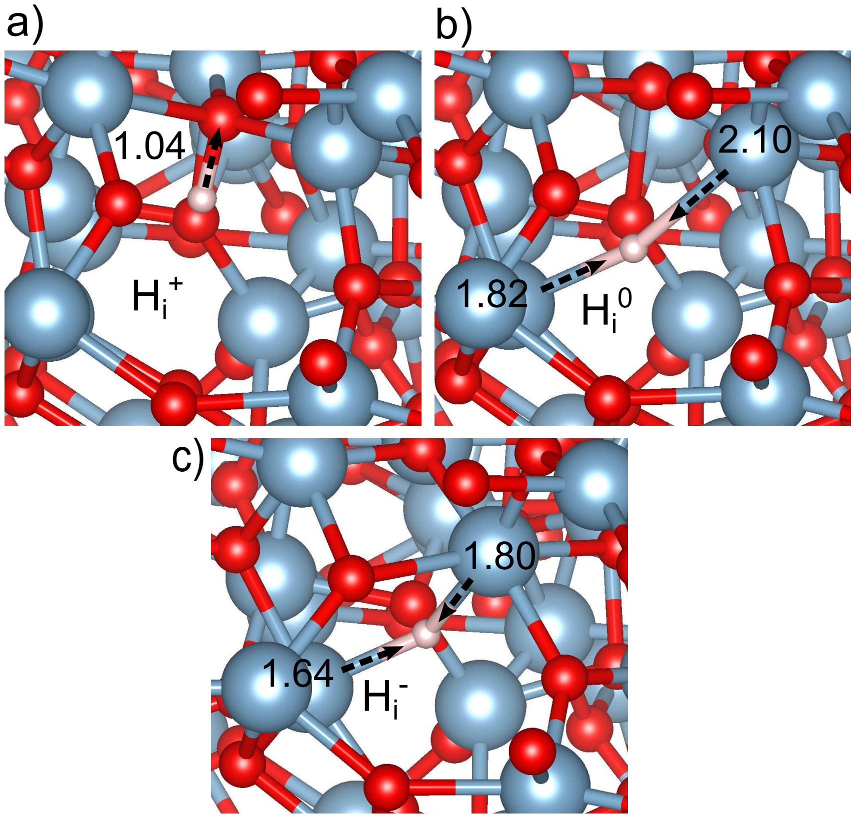

Figure 6.2: The structural configurations of the 3 H_i charge states, similar to those seen in crystalline Al_2O_3, with Al coloured grey, O red and H white. The arrows show the direction of relaxation, with the labels showing the length of the bond. a) the H_i^+ defect which forms an OH bond. b) H_i^0 which lies between 2 Al ions as atomic hydrogen. c) H_i^- also sits between 2 Al ions, though they relax towards the negatively charged ion.

than those with a $^{[3]}$O. This could be due to the addition of the proton significantly lowering the energy of the localized O σ_{2p}^* type orbitals observed at the top of the valence band in bulk a-Al_2O_3 (see section 4.3.3), which are a direct result of the O under-coordination.

6.3.1.2 H_i^0 and the $[H_i^+ + e_{CBM}]$ defect

The neutral hydrogen interstitial, H_i^0, behaves like an isolated hydrogen atom in crystalline Al_2O_3 and is 2 coordinated with Al [189]. It causes minimal relaxation of the surrounding lattice due to the charge neutrality [189]. The H_i^0 defect can display similar characteristics in a-Al_2O_3, where the OH bond of the H_i^+ is broken and the electron localizes on the proton, forming an isolated hydrogen atom (see Fig 6.2b).

However, the neutral hydrogen interstitial defect in amorphous Al_2O_3 can differ significantly from that in the crystalline material. In a-Al_2O_3 there are 2 possible configurations of the H_i^0 and, occasionally, the H_i^- defects. When an H atom or H^- ion is introduced into amorphous Al_2O_3, it is possible for it to donate its electrons into the conduction band whilst forming an OH bond with a nearest neighbour oxygen (similar to the configuration seen in Fig 6.2a). This can be considered as an $[H_i^+ + e_{CBM}]$ or an $[H_i^+ + 2e_{CBM}]$ defect, where e_{CBM} denotes a delocalized electron in the conduction band. DFT calculations using LDA functionals observed that for some oxides the H(+/-) charge transition level lies above the CBM [194]. This is attributed to a pinning of the H_i^0 energy level at approximately 4.5 eV below the vacuum level [194], meaning in oxides with a larger electron affinity, the energy needed to break the OH bond is greater than that required to place an electron in the conduction band.

In a review of hydrogen and muonium data [195], and their role as shallow or deep donors and acceptors, it is predicted that H_i^0 in materials with electron affinities greater than 4 eV will auto-ionize and donate an electron into the conduction band, which is confirmed by ESR data [195]. Later studies, using HSE06, demonstrate that crystalline TiO_2 and SnO_2 show similar behaviour [189], both of which have electron affinities greater than 4 eV [195] and band gaps smaller than 5 eV [189]. Amorphous HfO_2 also has a $[H_i^+ + e_{CBM}]$ like defect, though the donated electron localizes at an intrinsic trap site, rather than delocalizing in the conduction band minimum. This lowers its formation energy and allows it to become energetically favourable [191]. The trapping energy of an electron polaron in a-HfO_2 is approximately 1 eV, and so this compensates for the higher band gap of approximately 6.0 eV [191] (and a lower electron affinity of approximately 3 eV [195]).

The $[H_i^+ + e_{CBM}]$ defect is most likely observed in a-Al_2O_3 due to the lowering of the conduction band in a-Al_2O_3 (see section 4.3.3) when compared to α-Al_2O_3. The lowering of the conduction band corresponds to an increase in the electron affinity towards the 4 eV suggested as the H_i^0 pinning level, and when the local structural relaxation lowers the energy surrounding the defect sufficiently, $[H_i^+ + e_{CBM}]$ can be more energetically stable than H_i^0 in the amorphous material. The $[H_i^+ + e_{CBM}]$ defect can be considered a meta-stable state in a-Al_2O_3, which is not observed in the crystalline material where the conduction band is higher, and the energy gained from structural relaxations is smaller.

6.3.1.3 H_i^-

In 7 out of the 10 interstitial hydrogen defects calculated, the negatively charged hydrogen interstitial forms an isolated H^- ion, as shown in Fig. 6.2c. This is similar to the structural geometry of the defect observed in α-Al_2O_3 and θ-Al_2O_3 [189]. In the other 3 configurations an $[H_i^+ + 2e_{CBM}]$ defect is formed.

In the formation of the H_i^- defect, the electron that is introduced to the system localizes on the hydrogen, giving the ion an average Bader charge of -0.9$|e|$. The negative charge of the hydrogen ion causes significant relaxation of the 2 nearest neighbour Al ions, which are attracted to the interstitial hydrogen due to their formal +3 positive charge. An example of this relaxation can be seen in Fig. 6.2. During this relaxation the Al-H bond contracts by 0.19 to 0.36 Å, when compared to the bond lengths in the neutral charge state. Similar relaxation of the 2 nearest neighbour Al towards the H_i^- defect is observed in crystalline Al_2O_3 [188, 189], with the hydrogen sitting equidistant between the aluminium ions with a bond length of 1.67 Å. Relaxation of multiple cations towards the defect also occurs in amorphous HfO_2 [191], and crystalline MgO and La_2O_3 [189]. This differs from the relaxation observed in more covalent oxides, like amorphous SiO_2 [196] and crystalline SiO_2 and GeO_2 [189], where the negatively charged hydrogen bonds to a single cation, causing large relaxation of the surrounding oxygens. This would suggest that the ionicity of the material strongly affects the configuration and bonding character of the H_i^- defect.

6.3.1.4 The charge transfer level and energy levels of H_i

It is widely accepted that interstitial hydrogen in crystalline Al_2O_3 exhibits 'negative-U' behaviour, meaning its +1 (H_i^+) or -1 (H_i^-) charge states are more

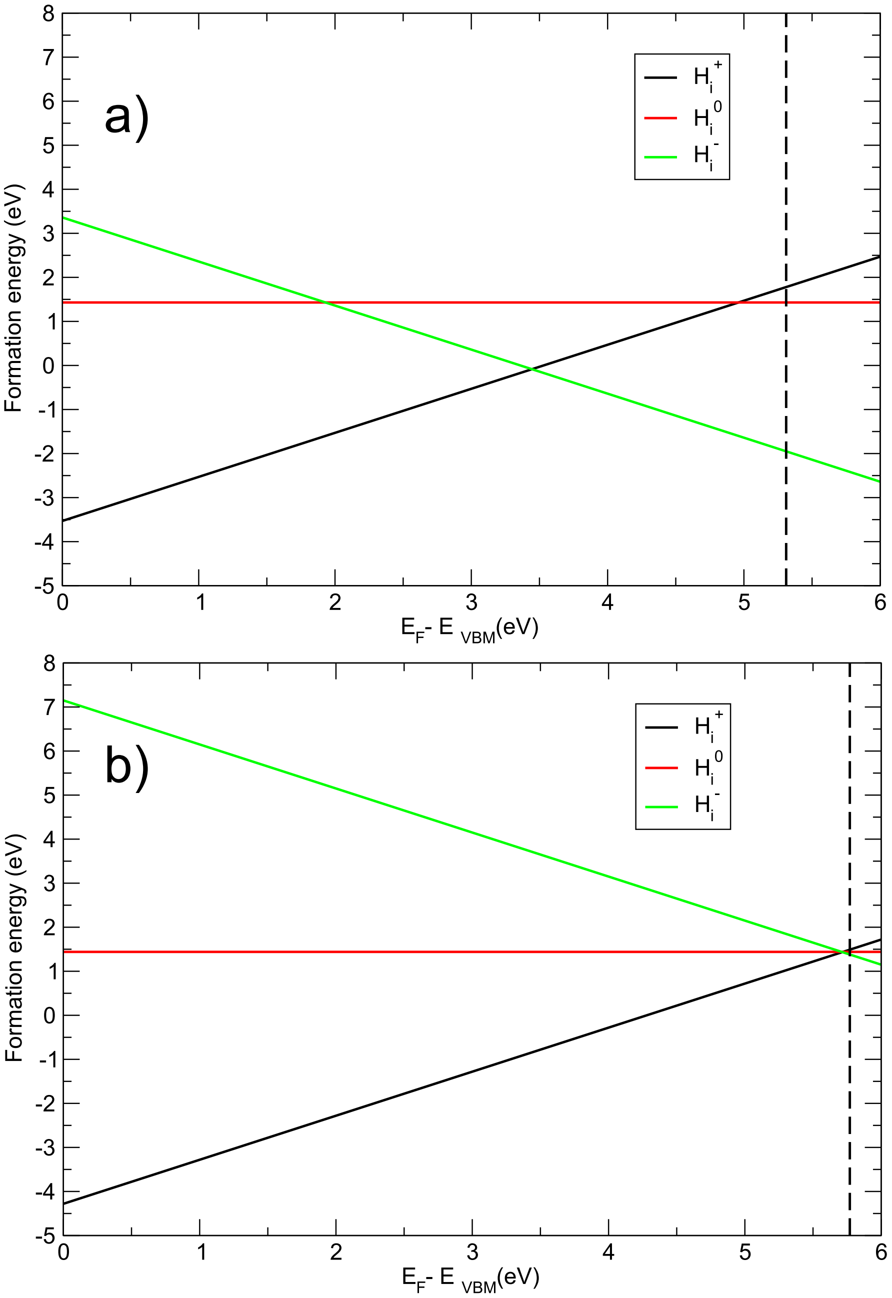

Figure 6.3: The formation energy of the different charge states of interstitial hydrogen against the Fermi energy with respect to the valence band. The dashed vertical line shows the position of the CBM. a) The formation energy of the H_i^+, H_i^0 and H_i^- where the OH bond is broken in the neutral and negative charge state, as seen in Fig. 6.2b and Fig. 6.2c. b) The formation energy of H_i^+, $[H_i^+ + e_{CBM}]$ and $[H_i^+ + 2e_{CBM}]$, here the (+/-) charge transfer level is at the CBM.

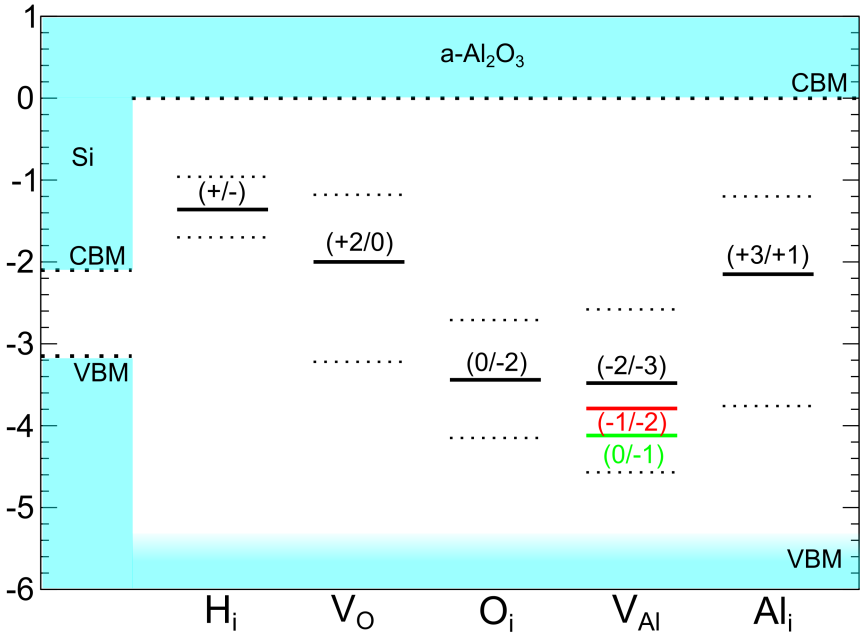

Figure 6.4: The average (solid line) charge transfer levels of H_i, V_O, O_i, V_{Al} and Al_i with respect to the a-Al_2O_3 CBM, with the y axis the energy in units of eV. The dashed lines represent the calculated range of the levels in the different samples. The Si/a-Al_2O_3 conduction band offset is taken from internal electron photoemission measurements [113].

thermodynamically stable than its neutral state (H_i^0) for all values of the Fermi energy [185, 187–189]. The calculations presented here show that this holds true for interstitial hydrogen in a-Al_2O_3. As can be seen from Fig. 6.3, there is only a (+/-) charge transition level for the H_i^- defect, and the $[H_i^+ + 2e_{CBM}]$ defect necessarily has the charge transition level when the Fermi energy is aligned with the CBM. The formation energy of the neutral defect is never lower than that of H_i^+ or H_i^- at any value of the Fermi energy.

When only including the 7 H_i^- configurations which have a charge transition level in the band gap, the average (+/-) charge transition level lies 1.43 eV below the CBM, as can be seen in Fig. 6.4. The charge transition levels are shown with respect to the CBM in order to compare with experimentally measured conduction band offsets of a-Al_2O_3 with Si [119].

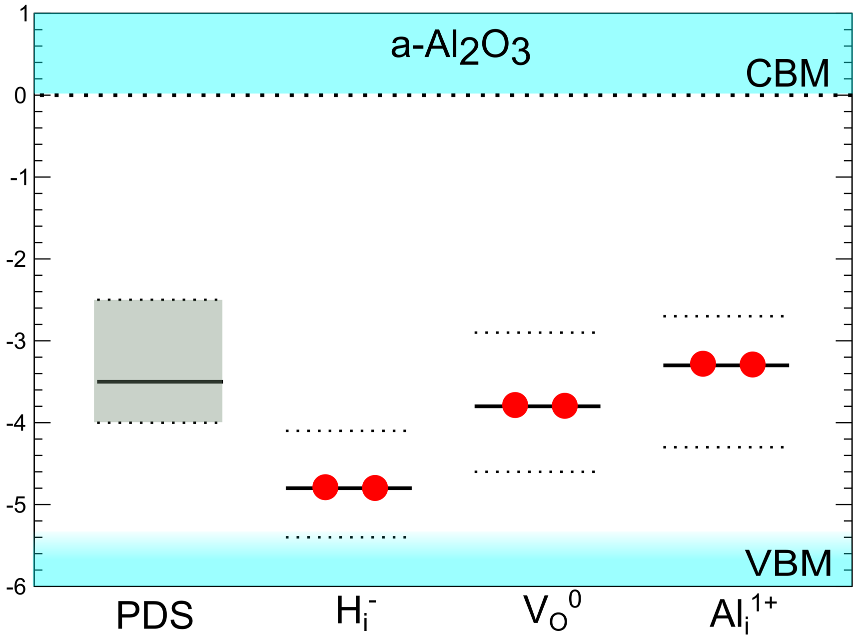

Figure 6.5: The average (solid black line) and range (dotted lines) of the Kohn-Sham energy levels of the Al_i, V_O or H_i defects with respect to the a-Al_2O_3 conduction band, compared to the experimental PDS trap energy level range [22]. For the PDS data the solid black line shows the energy of at the maximum density of states seen in Fig. 6.1.

In Fig. 6.4 it can be seen that the (+/-) charge transition level lies above the Si conduction band, but only by an average of 0.6 eV, with the lowest (+/-) level within 0.2 eV of the Si CBM. The voltage applied across the gate dielectric during transistor device operation would lower these levels with respect to the Si conduction band, which could lead to electron trapping via a tunneling mechanism.

In [22], the negative charge traps in a-Al_2O_3 can be populated via the same tunneling mechanism. By varying the charging potential, traps at a range of energy levels in the alumina gap can be populated when they are aligned with the injection level. Therefore H_i^- could be responsible for the negative charging observed [22]. However, the Kohn-Sham energy levels of H_i^- lie an average of 4.8 eV below the CBM, approximately 1 eV lower than the extreme range of the trap levels measured by photodepopulation spectroscopy [22]. So whilst it is possible for interstitial

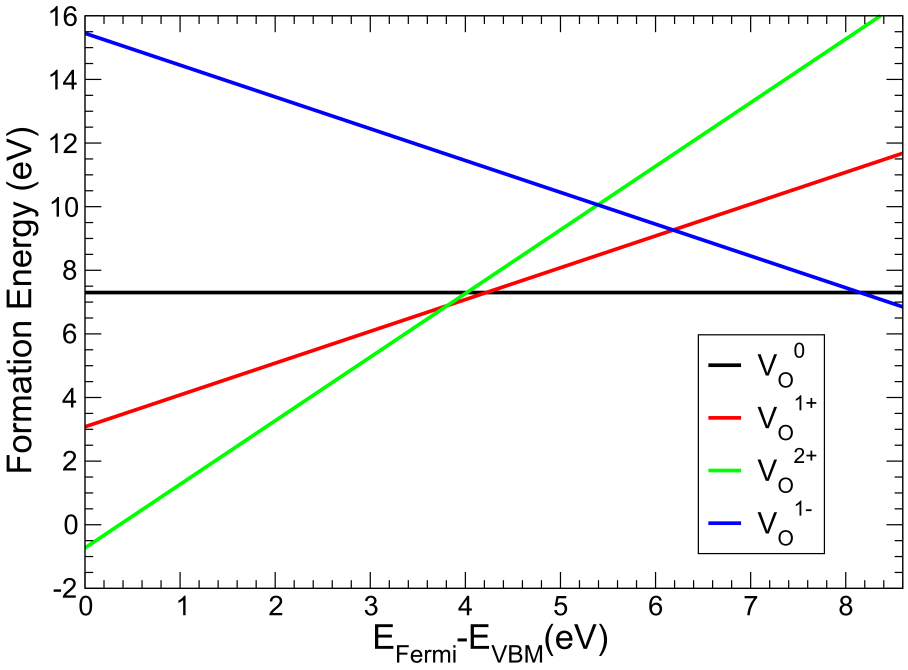

Figure 6.6: The formation energy of the different charge states of oxygen vacancies in α-Al_2O_3 against the Fermi energy with respect to the valence band.

hydrogen to trap electrons in a-Al_2O_3 [22, 23, 41], it is unlikely to be responsible for the defects observed by the spectroscopic measurements [22].

6.3.2 Oxygen vacancies

6.3.2.1 V_O in α-Al_2O_3

There is a large body of existing literature on oxygen vacancies in crystalline Al_2O_3, both computational [146, 186, 197] and experimental [198, 199]. This allows calculations of V_O in α-Al_2O_3 to be used to benchmark the DFT setup and hybrid functional parameters with respect to existing studies, and to act as a point of comparison to the amorphous system.

Fig. 6.6 shows the formation energy of various charge states of oxygen vacancies in α-Al_2O_3. It shows that oxygen vacancies have a (+2/+1) charge transition level at 3.8 eV above the VBM, with the (+1/0) level at 4.0 eV above the VBM, meaning that for most Fermi energies in the band gap the V_O^{2+} and V_O^0 are the most

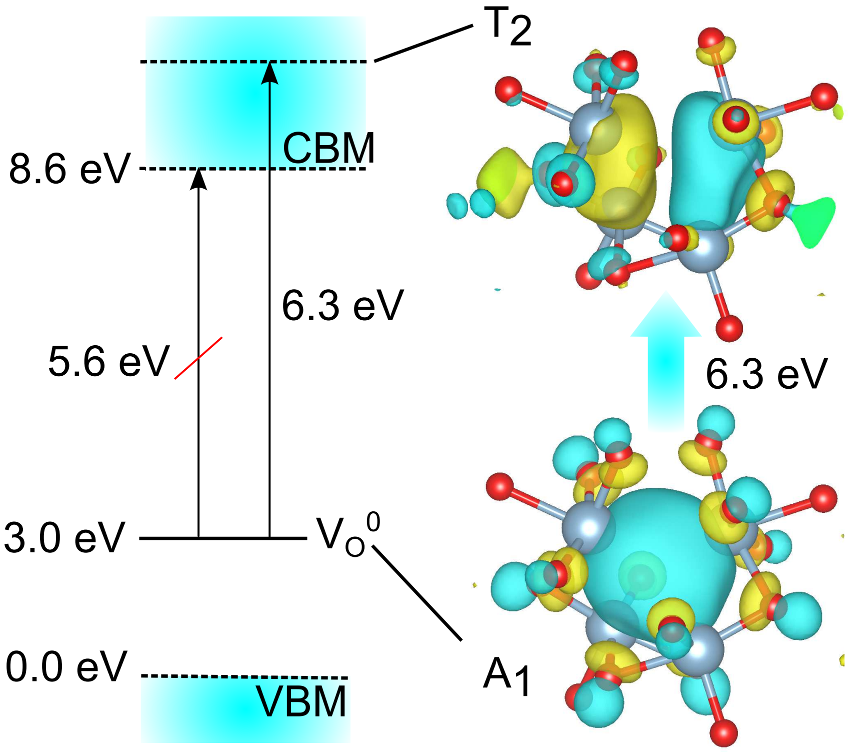

Figure 6.7: An energy level diagram for V_O^0 in α-Al_2O_3 showing the symmetry forbidden and allowed transitions, and the molecular orbitals of the A_1 and T_2 states involved in the symmetry allowed excitations.

thermodynamically stable charge states of the oxygen vacancy. During the geometry relaxation of the neutrally charged oxygen vacancy, the 4 nearest neighbour Al move 0.01-0.10 Å towards the defect site with respect to the perfect lattice. For V_O^{2+} they relax 0.19-0.30 Å away from the vacancy site with respect to the perfect lattice. These relaxation distances are in good agreement with Choi et al. [197]. However, whilst the nearest neighbour relaxations are similar, they calculate the (+2/+1) charge transition level to be 3.2 eV above the VBM, with the (+1/0) level at 4.1 eV [197]. This difference is likely due to the smaller cell size used in their paper (160 atoms), which would constrain the relaxation of the next nearest neighbour ions, increasing the energy of the V_O^{2+} defect. Over estimation of the V_O^{2+} formation energy is also observed in other calculations using smaller cell sizes [146].

Luminescence spectra measurements [199] of α-Al_2O_3 assign an absorption peak at 6.4 eV to the neutral oxygen vacancy. This is greater than the 5.6 eV energy difference calculated between the V_O^0 Kohn-Sham energy level and the conduction

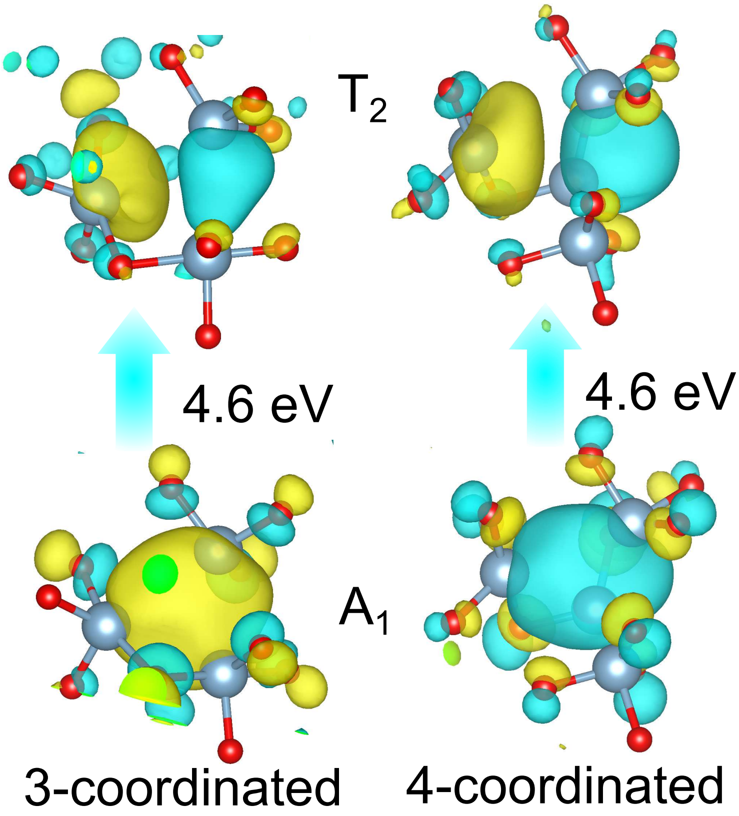

Figure 6.8: The molecular orbitals of the A_1 and T_2 like states of 3 and 4 coordinated V_O^0 in a-Al_2O_3, and difference in energy between their Kohn-Sham levels.

band minimum. However, as oxygen in α-Al_2O_3 is 4 coordinated and has tetrahedral like symmetry with point group T_d, the A_1 like character of the neutral state (see Fig. 6.7) has minimal wavefunction overlap with the delocalized CBM in α-Al_2O_3 as it is composed of Al 3*s* orbitals. Instead, as can be seen in Fig. 6.7, the defect causes a localized state in the conduction band with T_2 like character. A_1 to T_2 excitations are symmetry allowed dipole transitions and are most likely responsible for the sharp peak observed experimentally [199]. The T_2 like state (see Fig. 6.7) lies 6.3 eV above the neutral vacancy level, and although the energy difference between Kohn-Sham levels is only a first approximation for excitation energies, the calculated transition energy is in very good agreement with the experimental results.

6.3.2.2 V_O in a-Al_2O_3

Oxygen vacancies in amorphous Al_2O_3 have also been investigated using DFT methods [190,200]. However, these studies only model vacancies in a single cell of

80 [200] and 160 [190] atoms respectively, which may not capture the full range of properties of V_O. In order to improve understanding of these defects in a-Al_2O_3, the properties of oxygen vacancies at 11 defect sites in 10 geometry samples have been calculated and are presented here. The distribution of the O coordination numbers has been taken into consideration, with 7 $^{[3]}$O, 2 $^{[2]}$O and 2 $^{[4]}$O being removed in order to create the oxygen vacancies.

In amorphous Al_2O_3 only the +2 or neutral charge states of the oxygen vacancy are thermodynamically stable. The same behaviour is observed by Guo et al. [190]. The (+2/0) charge transition level lies, on average, 3.5 eV above the VBM and 2.0 eV below the CBM (see Fig. 6.4). In the neutral charge state 2 electrons localize on the vacancy site, forming an F-centre, similar to the defect in the crystalline system. As V_O^0 has a doubly occupied state in the band gap it could be responsible for the transitions seen experimentally [22], after charge injection. The high (+2/0) charge transition level suggests that before charge injection, whilst the Fermi level lies at the VBM, V_O^{2+} is the most stable configuration, which has no occupied states in the band gap. In a-Al_2O_3 there is no stable V_O^{1-} state and so it cannot be responsible for the negative charging observed in amorphous alumina films, unless it acts to compensate the negative charge of another defect.

The calculated V_O^0 Kohn-Sham energy levels lie an average of 4.0 eV below the CBM (see Fig. 6.5). The defects in the amorphous material create similar states to those observed in α-Al_2O_3. The 3 and 4-coordinated vacancy sites cause a localized state, similar to the A_1 state, to form in the band gap, and T_2 like states to appear within the conduction band (see Fig. 6.8). The further distortion of the tetrahedral symmetry means there is greater mixing of the states, and in 3 coordinated sites, there is significant relaxation from the next nearest neighbour Al ions, but the presence of the T_2 like state suggests there could be high oscillator strength transitions at larger excitation energies. On average the energy levels of the T_2 like states lie 4.8 eV above the energy level of V_O^0. Whilst this level lies deep into the band gap, close to the valence band in a-Al_2O_3, this is still significantly lower than the 6.5 eV excitation assigned to the neutral oxygen vacancy measured using electron

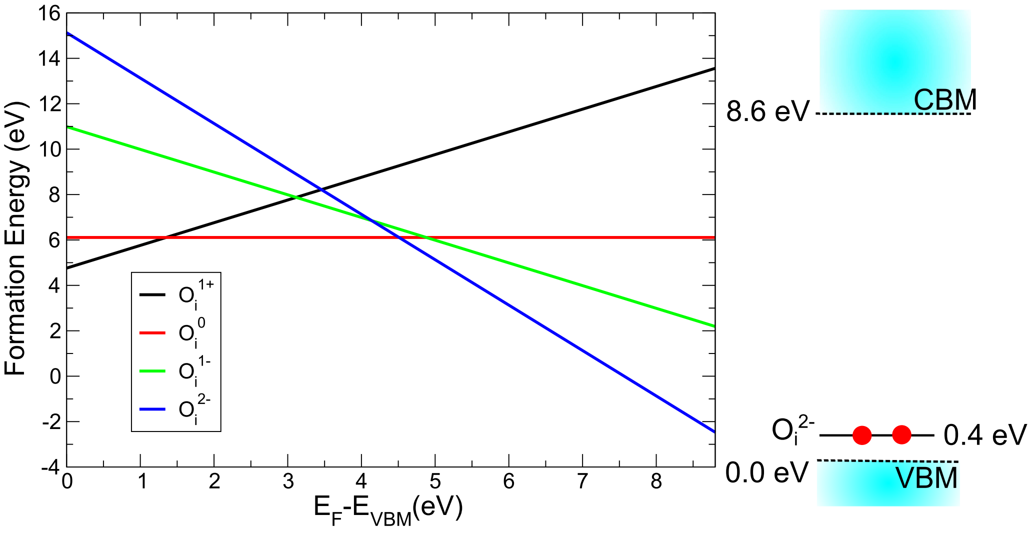

Figure 6.9: The formation energy of the different charge states of interstitial oxygen in α-Al_2O_3 against the Fermi energy with respect to the valence band, and the Kohn-Sham energy level position of the doubly occupied O_i^{2-} defect.

energy loss spectroscopy (EELS) [201]. However, it is not clear that the excitation observed is not instead the onset of inter band transitions [201]. Due to the shift in band gap of a-Al_2O_3, the neutral vacancy will not have the same excitation energy in α and a-Al_2O_3, especially when the amorphous alumina band gap has been measured to be 6.2 eV [113].

6.3.3 Interstitial oxygen

6.3.3.1 O_i in α-Al_2O_3

Neutrally charged oxygen interstitials in α-Al_2O_3 form an O-O dimer at the defect site, centred on the original lattice position of the O ion. In this configuration both oxygens are 3 coordinated with Al, and the O-O bond length is 1.44 Å. It has 3 thermodynamically stable charge states, as can be seen from the formation energy diagram in Fig. 6.9. Importantly, it traps electrons and becomes O_i^{2-} when the Fermi energy is 4.5 eV above the VBM. This is close to the 4.7 eV (0/-2) charge transition level calculated by Choi et al. [197], using the HSE06 functional.

When the oxygen interstitial captures 2 electrons to become O_i^{2-}, the O-O bond length increases to 2.15 Å. This large displacement results in both O ions becoming 4 coordinated with Al, forming tetrahedral configurations. Due to this relaxation the Kohn-Sham energy level of O_i^{2-} lies only 0.4 eV above the valence band (see Fig. 6.9), as both O are fully coordinated. Its role as a deep acceptor is in good agreement with previous calculations [202].

6.3.3.2 O_i in a-Al_2O_3

To model the oxygen interstitial in the amorphous structure, single oxygen atoms were added to the 10 different geometry samples and placed within 1.6 Å of an O ion, with 4 near $^{[3]}$O, 3 near $^{[2]}$O and 3 next to $^{[4]}$O. Similar to the crystalline case, oxygen interstitials in a-Al_2O_3 have a deep (0/-2) charge transfer level. The average charge transfer energy lies 3.4 eV below the CBM, and 2.1 eV above the VBM. Guo et al. [190] calculate the average charge transfer level to be 2.5 eV above the VBM and similarly show there is no Fermi Energy where the O_i^- charge state is thermodynamically stable.

When the neutral charge state of the oxygen interstitial is relaxed it forms an O-O peroxy bond with the nearest neighbour oxygen. The average O-O bond length of the 10 defect configurations is 1.46 Å for the neutral charge state. When 2 electrons are added to the system, forming O_i^{2-}, the O-O bond length relaxes to an average of 2.40 Å. This large relaxation significantly lowers the energy of the defect induced σ_{2p}^* like orbitals in the conduction band, down towards the valence band. These states become occupied meaning the O_i^{2-} Kohn-Sham energy levels lie within the valence band, with no states existing in the band gap. This can be compared to the formation of hole bipolarons in reverse. In the case of bipolaron formation, the contraction of an O-O bond to approximately 1.5 Å, after the removal of 2 electrons, pushes the now unoccupied σ_{2p}^* orbitals that form the top of the valence band (see section 5.3.5) into the conduction band.

The low lying charge transition level of interstitial oxygen means it is likely to be a source of electron trapping in a-Al_2O_3, but, the lack of states in the band gap mean it cannot explain the trap spectroscopy data [22]. Instead, it is possible that it can act as a store of negative charge which compensates for positively charged de-

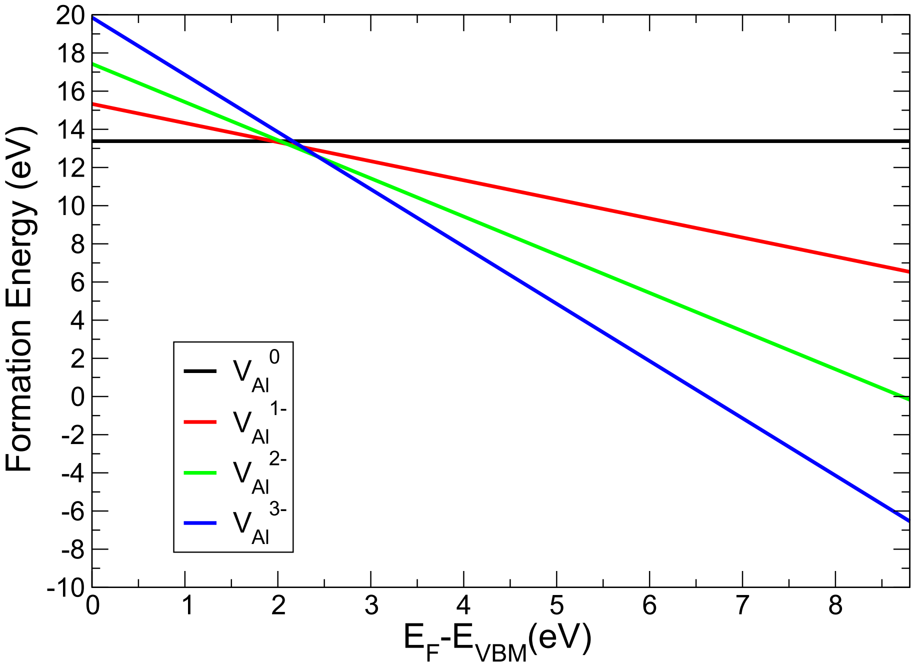

Figure 6.10: The formation energy of the different charge states of aluminium vacancies in α-Al_2O_3 plotted against the Fermi energy with respect to the valence band.

fects with unoccupied states in the gap. This could explain why experimentally the system is observed to be charge neutral before electron injection, with no transitions observed from gap states into the conduction band [22]. The transitions seen after electron injection (with the Fermi energy raised to the alumina conduction band) would then be due to the trapping of electrons in the unoccupied gap states, and the overall charging observed due to the mismatch between the number of positively and negatively charged defects [22]. Thus, whilst oxygen vacancies cannot trap negative charge in isolation, and oxygen interstitials don't have states in the gap, an oxygen Frenkel pair, for example $O_i^{2-}+V_O^0$, can have an overall negative charge and states lying in the band gap.

6.3.4 Aluminium vacancies

6.3.4.1 V_{Al} in α-Al_2O_3

The formation energy diagram for V_{Al} in α-Al_2O_3 (see Fig. 6.10) shows that the -3 charge state of the vacancy becomes stable at 2.4 eV above the VBM. This means the aluminium vacancy (0/-3) charge transition level lies even lower in the band gap than the interstitial oxygen (0/-2) level, and is therefore a likely source of fixed negative charge in amorphous alumina. This agrees with previous studies that show aluminium vacancies in α-Al_2O_3 [197] and κ-Al_2O_3 [186, 197] are very deep acceptors, with charge transition levels close to the valence band.

The formation energies presented here are calculated using an Al chemical potential derived from DFT calculations of pure Al metal. This is equivalent to an Al-rich environment, which explains the high formation energies of the neutral vacancy, and of the charged vacancies at Fermi energies close to the valence band (see Fig. 6.10). However, the low formation energies at Fermi levels nearer to the conduction band suggest that it will be the dominant negatively charged defect in crystalline alumina, even in Al-rich conditions.

6.3.4.2 V_{Al} in a-Al_2O_3

As can be seen in Fig 6.4, the -3 charge state of aluminium vacancies in a-Al_2O_3 becomes stable when Fermi energies are on average 3.5 eV below the conduction band (2.0 eV above the valence band), which is the lowest lying charge transition level of all the defects presented in this chapter, though is very close to the O_i (0/-2) level. 10 vacancy sites were examined with 4 $^{[4]}$Al, 3 $^{[4]}$Al and 3 $^{[4]}$Al removed to create the defects. However, little dependence on coordination was observed, with a deviation in the average (-2/-3) charge transfer level of less than 0.3 eV.

It is likely that aluminium vacancies will acts as deep electron traps in a-Al_2O_3, but, the highest occupied Kohn-Sham energy level of V_{Al}^{3-} (across all the samples) lies 4.7 eV below the CBM, with most of the defect states lying within the valence band. This suggests it is unlikely to be the charge trap measured by Zahid et al. [22]. It is more likely to act as a source of negative charge that compensates for positively

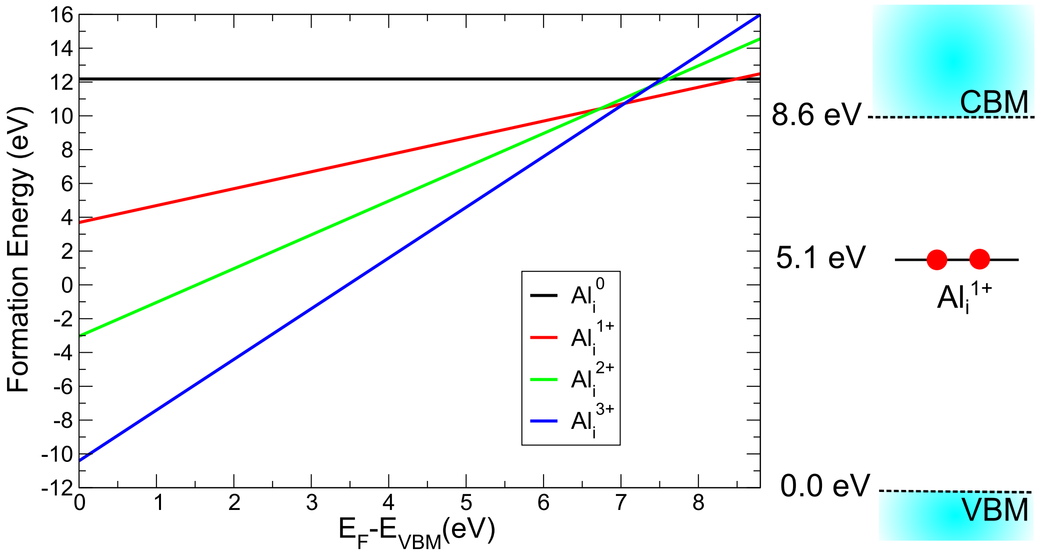

Figure 6.11: The formation energy of interstitial aluminium and its various charge states in α-Al_2O_3, plotted against the Fermi energy with respect to the valence band.

charged defects before electron injection, similar to the mechanism described in section 6.3.3.2.

6.3.5 Interstitial aluminium

6.3.5.1 Al_i in α-Al_2O_3

On a first examination of aluminium interstitials in α-Al_2O_3, they do not appear to be a good candidate for the negative charging observed experimentally. The formal charge of Al in Al_2O_3 is 3+, and Bader analysis shows the system is highly ionic. Thus, the addition of an Al atom donates 3 electrons into the system without introducing any unoccupied states in the predominantly O $2p$ valence band, meaning the defect is most likely to act as a donor in α-Al_2O_3. This is demonstrated by the formation energy diagram shown in Fig. 6.11 where the (+3/+1) level is only 1.6 eV below the CBM. Al_i^{3+} has the lowest formation energy for a wide range of the Fermi energy, and no occupied states in the band gap available for excitations into the conduction band. There are no thermodynamically stable negative charge states of Al_i observed at any Fermi energy, to act as independent electron traps.

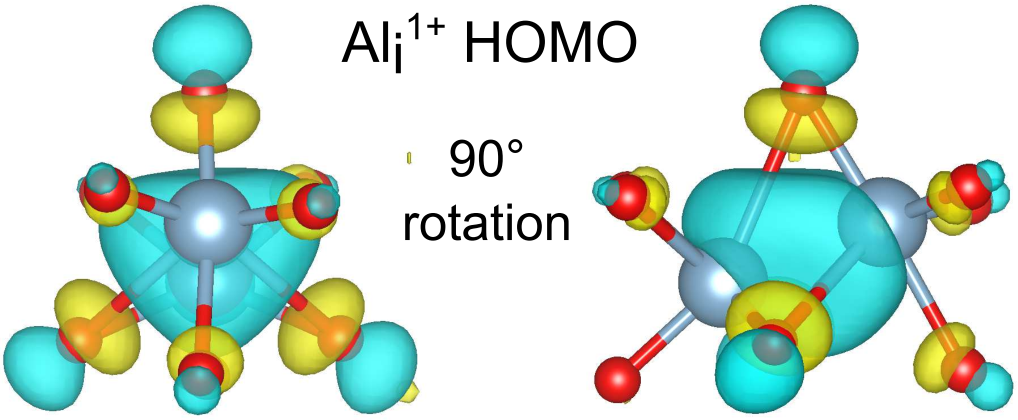

Figure 6.12: The isosurface of the Al_i^{1+} HOMO, in 2 orientations so as to see the D_{3h} point symmetry. The interstitial Al and its nearest neighbour Al are both 6 coordinated with O, though some Al-O bonds are extended to 2.6 Å.

However, Al_i^{1+} has a doubly occupied Kohn-Sham energy level in the middle of the band gap, 3.5 eV below the CBM (see Fig. 6.10). Optical absorption spectra measurements on sapphire attribute a peak at 4.1 eV to aluminium interstitial defects, and while there is a discrepancy of 0.6 eV, this gives some justification for the positive identification of this defect [198].

The D_{3h} like point symmetry of the Al_i^{1+} highest occupied molecular orbital (HOMO), can be seen in Fig. 6.12. The symmetry is a result of the triangle of oxygen ions whose atomic orbitals point into the defect centre between the 2 Al ions. The electrons localize between the 2 positively charged Al ions which lowers its energy. This symmetry means that an excitation into the conduction band minimum is a dipole allowed transition (A_1 to E). Thus, at least for the crystalline system, there exists a mid gap state in the same energy range as the levels seen experimentally [22], and, unlike the oxygen vacancy, the defect state perturbs the CBM state and an occupying electron can be excited straight into the bottom of the conduction band.

6.3.5.2 Al_i in a-Al_2O_3

In a-Al_2O_3 the average Kohn-Sham energy level of Al_i^{1+} lies 3.3 eV below the conduction band, with a range of 2.7-3.8 eV (see Fig. 6.5), in very good agreement with both the PDS and GS-TSCIS measurements [22]. The average (+3/+1) charge transfer level is 2.1 eV below the CBM (see Fig. 6.4). This means that for a large range of the Fermi energy interstitial aluminium is most stable in the 3+ charge state, which has no occupied states in the gap. However, after electron injection, the unoccupied states of the $\mathrm{Al}_\mathrm{i}^{3+}$ will trap electrons and become $\mathrm{Al}_\mathrm{i}^{1+}$. $\mathrm{Al}_\mathrm{i}^{1+}$ has a doubly occupied state in the gap, meaning the now filled gap states can then be excited into the conduction band and detected.

6.3.6 Matching the spectroscopy data

The findings in this chapter suggest that O_i and V_Al will be the dominant electron traps in a-$\mathrm{Al}_2\mathrm{O}_3$. Both defects become negatively charged when the Fermi energy is approximately in the middle of the band gap, and, as can be seen in Fig. 6.4, their average charge transfer levels lie below the Si VBM. This means that they are likely to be in their negative charge state for most values of the Fermi energy, but, their lack of occupied levels in the band gap mean they cannot be responsible for the traps seen by Zahid et al. [22].

The mechanism proposed here is that pairs of compensating defects are responsible for the behaviour seen experimentally, and that no single defect can be used to explain the spectroscopic data [22]. This explains why, before electron injection, no states are observed in the gap (see Fig. 6.1) and the charge is measured as neutral [22]. Negatively charged O_i or V_Al are compensated by positively charged Al_i, V_O or H_i defects, leaving the system charge neutral with no states in the gap. Then, when the Fermi level is raised to the a-$\mathrm{Al}_2\mathrm{O}_3$ conduction band, electrons can occupy the Al_i, V_O or H_i states in the gap, which can then be observed spectroscopically (see Fig. 6.1) after excitation into the conduction band. This filling of states also leads to an overall negative charge being observed.

As was discussed in section 6.1, in a-$\mathrm{Al}_2\mathrm{O}_3$ the difference in Kohn-Sham energies between the defect state and the CBM can be taken as a good approximation for transition energies calculated by TDDFT [184], due to the delocalized nature of the CBM [42] and the lack of localized states near the band edge (see chapter 4). With this in mind, the Kohn-Sham energy levels of Al_i, V_O or H_i, with respect to the CBM, are shown in Fig. 6.5, all have levels within the range measured experimentally [22]. This means more than one type of defect could be responsible for the trap states. However, experimental measurements could determine the defect type more confidently by adjusting the growth conditions of alumina thin films so as to control the oxygen and aluminium chemical potentials.

6.4 Conclusion

In order to understand the source of negative charging in a-Al_2O_3 films [22, 23, 41, 42], the electronic properties of the defects H_i, V_O, O_i, V_{Al} and Al_i were calculated using DFT.

O_i and V_{Al} were both found to have deep acceptor levels, with the average O_i (0/-2) charge transfer level lying 3.4 eV below the a-Al_2O_3 CBM, and the average V_{Al} (-2/-3) charge transfer level lying 3.5 eV below the CBM. However, their lack of occupied energy levels in the band gap means that they are not responsible for the transitions seen in the PDS and GS-TSCIS measurements [22].

To explain the transitions seen experimentally [22] (see Fig. 6.1) a mechanism is proposed whereby the negatively charged O_i and V_{Al} defects are compensated by the positively charged H_i, V_O and Al_i defects when the system has zero overall charge. Following electron injection, the states of Al_i, V_O or H_i in the band gap become occupied and transitions are observed into the conduction band. The Kohn-Sham energy levels of these defects, with respect to the conduction band (see Fig 6.5), overlap with the PDS and GS-TSCIS measurements [22].

Chapter 7

General Conclusions

7.1 Summary

Through the use of electronic structure methods, defects and charge trapping have been modeled in both $LaAlO_3$ and amorphous Al_2O_3. The results have offered new theoretical insights into the behaviour of defects and polarons in these materials, confirmed experimental results, and given predictions that can be tested in lab grown thin films. These findings will hopefully contribute to the development of new nanoelectronic devices.

In chapter 3 the absorption spectra of V_O^0 and V_O^+ in $LaAlO_3$ were presented and compared to experiment, along with the ESR parameters predicted for the paramagnetic defect, V_O^+. The structural and electronic properties of cubic and rhombohedral $LaAlO_3$ were also calculated with DFT using both periodic and embedded cluster methods, and hybrid density functionals.

TDDFT calculations of V_O^+ in rhombohedral $LaAlO_3$ predicted the intensity maximum of the photoexcitation energies to be at 3.6 eV, with the single peak extending from 3.2 eV to 4.0 eV. These predictions agreed well with the measurements of Kawabe et al. [84], who see an absorption tail at 3.5-4.1 eV, which they attribute to oxygen deficiency. The isotropic g-value of V_O^+ in rhombohedral $LaAlO_3$ was calculated to be 2.004026. The hyperfine calculations predict a 3.0 mT broadening of the ESR signal due to hyperfine splitting of the vacancy's nearest neighbour Al. These match reported ESR experimental results [43,86], and, with the TDDFT data, explain the absorption peaks that appear with an increase of the V_O^+ ESR signal [43].

The next chapter discussed the bulk properties of amorphous Al_2O_3, and the cause of its band gap reduction that is observed experimentally [35,113–117]. Using a molecular dynamics melt and quench method, a-Al_2O_3 structures were generated that reproduced not only experimental densities [24, 33, 148], but also NMR measurements of ion coordination numbers [39] and radial distribution functions from X-ray diffraction experiments [38]. To accurately model the electronic structure of a-Al_2O_3 the PBE0-TC-LRC [40] functional was tuned to obey Koopmans' condition. This ensured that DFT calculations would predict the correct band gap for a-Al_2O_3 and minimize the over and under delocalization of holes and electrons when modeling polarons and defects. The tuned functional was benchmarked against the properties of crystalline α-Al_2O_3, reproducing its electronic structure and the experimental band gap of 8.6 eV [112].

DFT calculations of 10 geometry samples, using the tuned hybrid functional, predicted the average HOMO-LUMO gap of a-Al_2O_3 to be 5.48 eV. Inverse participation ratio (IPR) analysis showed the edge of the valence band to be highly localized, with the mobility edge lying approximately 1 eV below the valence band maximum. The localization at the edge of the band is attributed to 2 coordinated O σ_{2p}^* states, a result of the under coordination of O ions in the amorphous phase. IPR analysis of the conduction band showed it to be delocalized. The electrostatic potential of Al ions was observed to shift downwards 1.6 V relative to the crystalline phase, as a result of the reduction in Al-O coordination number and thus change in the bonding character. This causes the conduction band, which is predominantly composed of Al 3s states, to shift downwards, providing a theoretical explanation for the conduction band shift observed experimentally [35].

The localized states at the valence band maximum were shown to result in the spontaneous trapping of hole polarons in a-Al_2O_3, which have an average trapping energy of 1.26 eV. This is higher than the 0.38 eV hole trapping energy calculated in α-Al_2O_3. The holes preferentially localized on 2 nearest-neighbour oxygen ions, associated with the σ_{2p}^* states at the top valence band, described as 'precursor sites'.

The locations of these sites were able to be predicted using IPR analysis, which also gives an estimate of the density of precursors to be 2.6×10^{20} cm^{-3}. Hole bipolarons were also modeled, though nudged elastic band calculations showed they had very high barriers to formation of approximately 1.6 eV. Electrons were shown not to localize in either α-Al_2O_3 or a-Al_2O_3, which is attributed to the delocalized nature of the conduction band minimum and its high dispersion.

In the final chapter H_i, V_O, O_i, V_{Al} and Al_i defects were investigated in order to find the source of negative charging observed experimentally in a-Al_2O_3 thin films [22, 23, 41, 42]. Understanding the cause of this electron trapping is important for the development of non-volatile charge trap flash memory devices [22, 23], a-IGZO (amorphous indium gallium zinc oxide) thin film transistors [24], and solar cells [25–27]. In order to explain the charge trap spectroscopy measurements performed by Zahid et al. [22] a mechanism is proposed whereby O_i and V_{Al} defects, which have deep acceptor levels, compensate the positively charged H_i, V_O and Al_i defects before the film becomes charged. Then, after electron injection, empty states of H_i, V_O and Al_i in the band gap become occupied, causing the overall charge to become negative. The Kohn-Sham levels of these defects match the position of the levels measured by PDS and GS-TSCIS measurements [22], with Al_i matching the distribution most closely, with its average level 3.3 ev below the conduction band minimum. This suggests it could be possible to control charging in the thin films via adjustment of growth temperatures and oxygen partial pressures, which would be able to determine whether oxygen or aluminium defects were the dominant cause of electron trapping.

7.2 Future work

Defects and charge trapping in $LaAlO_3$ and amorphous Al_2O_3 have been extensively characterized in this thesis, but the results themselves open up opportunities for future investigation. There is also interest in novel device applications for amorphous alumina films, and improvements in computing power and added functionality of codes means new and more complex phenomena can be investigated.

Although not suitable as the active layer in resistive RAM (ReRAM) technology, thin layers of Al_2O_3 are used as a blocking layer in HfO_2 and other metal oxide ReRAM devices [203–205]. The thin amorphous Al_2O_3 layer is assumed to act as an oxygen diffusion barrier, and so, prevents the depletion of oxygen in the HfO_2 layer and lateral migration of oxygen away from the conducting filament [205]. Building on the results discussed in chapter 6, nudged elastic band calculations of oxygen vacancies and oxygen interstitials could be performed to predict the activation barriers for oxygen diffusion through alumina, and so improve understanding of ReRAM device operation.

There is also growing interest in the use of amorphous Al_2O_3 in neuromorphic memristor devices [206, 207], which have multiple switching states designed to mimic neurons in the brain. Development of these devices would require modeling of charge trapping at a-Al_2O_3/metal oxide interfaces and similar calculations of the oxygen diffusion barriers that were suggested for ReRAM devices.

Amorphous Al_2O_3 will continue to be a material of great interest in the field of nanoelectronics. The work presented in this thesis has developed our theoretical understanding of defects and charge trapping on the atomic scale and will hopefully contribute to future applications using $LaAlO_3$ and Al_2O_3.

Bibliography

[1] J. Robertson, “High dielectric constant oxides,” *The European Physical Journal Applied Physics*, vol. 28, no. 3, pp. 265–291, 2004.

[2] J. Woodyard, “Nonlinear circuit device utilizing germanium,” 1950. US Patent 2,530,110.

[3] H. L. Tuller and S. R. Bishop, “Point Defects in Oxides: Tailoring Materials Through Defect Engineering,” *Annual Review of Materials Research*, vol. 41, no. 1, pp. 369–398, 2011.

[4] Z. K. Yuan, S. Chen, H. Xiang, X. G. Gong, A. Walsh, J. S. Park, I. Repins, and S. H. Wei, “Engineering Solar Cell Absorbers by Exploring the Band Alignment and Defect Disparity: The Case of Cu- and Ag-Based Kesterite Compounds,” *Advanced Functional Materials*, vol. 25, no. 43, pp. 6733–6743, 2015.

[5] S. Kim, J.-S. Park, and A. Walsh, “Identification of Killer Defects in Kesterite Thin-Film Solar Cells,” *ACS Energy Letters*, pp. 496–500, 2018.

[6] Y.-M. Kim, J. He, M. D. Biegalski, H. Ambaye, V. Lauter, H. M. Christen, S. T. Pantelides, S. J. Pennycook, S. V. Kalinin, and A. Y. Borisevich, “Probing oxygen vacancy concentration and homogeneity in solid-oxide fuel-cell cathode materials on the subunit-cell level,” *Nature Materials*, vol. 11, no. 10, pp. 888–894, 2012.

[7] B. Mohammad, M. A. Jaoude, V. Kumar, D. M. Al Homouz, H. A. Nahla, M. Al-Qutayri, and N. Christoforou, "State of the art of metal oxide memristor devices," *Nanotechnology Reviews*, vol. 5, no. 3, pp. 311–329, 2016.

[8] N. C. Bristowe, P. B. Littlewood, and E. Artacho, "Surface defects and conduction in polar oxide heterostructures," *Physical Review B*, vol. 83, no. 20, p. 205405, 2011.

[9] N. C. Bristowe, P. Ghosez, P. B. Littlewood, and E. Artacho, "The origin of two-dinemsional electron gases at oxide interfaces: insights from theory," *Journal of Physics: Condensed Matter*, vol. 26, p. 143201, 2014.

[10] S. A. Chambers, M. H. Engelhard, V. Shutthanandan, Z. Zhu, T. C. Droubay, L. Qiao, P. V. Sushko, T. Feng, H. D. Lee, T. Gustafsson, E. Garfunkel, A. B. Shah, J.-M. Zuo, and Q. M. Ramasse, "Instability, intermixing and electronic structure at the epitaxial $LaAlO_3/SrTiO_3(001)$ heterojunction," *Surface Science Reports*, vol. 65, pp. 317–352, 2010.

[11] L. Qiao, T. C. Droubay, V. Shutthanandan, Z. Zhu, P. V. Sushko, and S. A. Chambers, "Thermodynamic instability at the stoichiometric $LaAlO_3/SrTiO_3(001)$ interface," *Journal of Physics: Condensed Matter*, vol. 22, p. 312201, 2010.

[12] A. Ohtomo and H. Y. Hwang, "A high-mobility electron gas at the $LaAlO_3/SrTiO_3$ heterointerface," *Nature*, vol. 427, pp. 423–6, 2004.

[13] N. Nakagawa, H. Y. Hwang, and D. A. Muller, "Why some interfaces cannot be sharp," *Nature Materials*, vol. 5, pp. 204–209, 2006.

[14] Z. S. Popovic, S. Satpathy, and R. M. Martin, "Origin of the two-dimensional electron gas carrier density at the $LaAlO_3$ on $SrTiO_3$ interface," *Physical Review Letters*, vol. 101, p. 256801, 2008.

[15] R. Pentcheva and W. E. Pickett, “Ionic relaxation contribution to the electronic reconstruction at the n-type $LaAlO_3/SrTiO_3$ interface,” *Physical Review B*, vol. 78, p. 205106, 2008.

[16] P. R. Willmott, S. A. Pauli, R. Herger, C. M. Schlepütz, D. Martoccia, B. D. Patterson, B. Delley, R. Clarke, D. Kumah, C. Cionca, and Y. Yacoby, “Structural basis for the conducting interface between $LaAlO_3$ and $SrTiO_3$,” *Physical Review Letters*, vol. 99, p. 155502, 2007.

[17] L. Qiao, T. C. Droubay, T. C. Kaspar, P. V. Sushko, and S. A. Chambers, “Cation mixing, band offsets and electric fields at the $LaAlO_3/SrTiO_3(001)$ heterojunctions with variable La:Al atom ratio,” *Surface Science*, vol. 605, pp. 1381–1387, 2011.

[18] M. P. Warusawithana, C. Richter, J. A. Mundy, P. Roy, J. Ludwig, S. Paetel, T. Heeg, A. A. Pawlicki, L. F. Kourkoutis, M. Zheng, M. Lee, B. Mulcahy, W. Zander, Y. Zhu, J. Schubert, J. N. Eckstein, D. A. Muller, C. S. Hellberg, J. Mannhart, and D. G. Schlom, “$LaAlO_3$ stoichiometry is key to electron liquid formation at $LaAlO_3/SrTiO_3$ interfaces,” *Nature Communications*, vol. 4, p. 2351, 2013.

[19] L. Yu and A. Zunger, “A polarity-induced defect mechanism for conductivity and magnetism at polarnonpolar oxide interfaces,” *Nature Communications*, vol. 5, p. 5118, 2014.

[20] M. Huijben, G. Koster, M. K. Kruize, S. Wenderich, J. Verbeeck, S. Bals, E. Slooten, B. Shi, H. J. A. Molegraaf, J. E. Kleibeuker, S. van Aert, J. B. Goedkoop, A. Brinkman, D. H. A. Blank, M. S. Golden, G. van Tendeloo, H. Hilgenkamp, and G. Rijnders, “Defect Engineering in Oxide Heterostructures by Enhanced Oxygen Surface Exchange,” *Advanced Functional Materials*, vol. 23, no. 42, pp. 5240–5248, 2013.

[21] W. Siemons, G. Koster, H. Yamamoto, W. Harrison, G. Lucovsky, T. Geballe, D. Blank, and M. Beasley, “Origin of Charge Density at $LaAlO_3$ on $SrTiO_3$

Heterointerfaces: Possibility of Intrinsic Doping," *Physical Review Letters*, vol. 98, p. 196802, 2007.

[22] M. B. Zahid, D. R. Aguado, R. Degraeve, W. C. Wang, B. Govoreanu, M. Toledano-Luque, V. V. Afanasev, and J. Van Houdt, "Applying Complementary Trap Characterization Technique to Crystalline gamma-phase-Al_2O_3 for Improved Understanding of Nonvolatile Memory Operation and Reliability," *IEEE Transactions on Electron Devices*, vol. 57, no. 11, pp. 2907–2916, 2010.

[23] Ya Li, Yanli Pei, Ruiqin Hu, Zimin Chen, Yiqiang Ni, Jiayong Lin, Yiting Chen, Xiaoke Zhang, Zhen Shen, Jun Liang, Bingfeng Fan, Gang Wang, and He Duan, "Charge Trapping Memory Characteristics of Amorphous-Indium-Gallium-Zinc-Oxide Thin-Film Transistors With Defect-Engineered Alumina Dielectric," *IEEE Transactions on Electron Devices*, vol. 62, no. 4, pp. 1184–1188, 2015.

[24] K.-C. Ok, S. Oh, H.-J. Jeong, J. U. Bae, and J.-S. Park, "Effect of Alumina Buffers on the Stability of Top-Gate Amorphous InGaZnO Thin-Film Transistors on Flexible Substrates," *IEEE Electron Device Letters*, vol. 36, no. 9, pp. 917–919, 2015.

[25] M. M. Lee, J. Teuscher, T. Miyasaka, T. N. Murakami, and H. J. Snaith, "Efficient Hybrid Solar Cells Based on Meso-Superstructured Organometal Halide Perovskites," *Science*, vol. 338, no. 6107, pp. 643–647, 2012.

[26] J. M. Ball, M. M. Lee, A. Hey, and H. J. Snaith, "Low-temperature processed meso-superstructured to thin-film perovskite solar cells," *Energy & Environmental Science*, vol. 6, p. 1739, 2013.

[27] A. J. Pearson, G. E. Eperon, P. E. Hopkinson, S. N. Habisreutinger, J. T. W. Wang, H. J. Snaith, and N. C. Greenham, "Oxygen Degradation in Mesoporous $Al_2O_3/CH_3NH_3PbI_3$-xClx Perovskite Solar Cells: Kinetics and Mechanisms," *Advanced Energy Materials*, vol. 6, p. 1600014, 2016.

[28] M. Kaviani, J. Strand, V. V. Afanas'Ev, and A. L. Shluger, "Deep electron and hole polarons and bipolarons in amorphous oxide," *Physical Review B*, vol. 94, no. 2, p. 020103, 2016.

[29] D. Ceresoli and D. Vanderbilt, "Structural and dielectric properties of amorphous ZrO_2 and HfO_2," *Physical Review B*, vol. 74, no. 12, p. 125108, 2006.

[30] M. Landmann, T. Köhler, S. Köppen, E. Rauls, T. Frauenheim, and W. Schmidt, "Fingerprints of order and disorder in the electronic and optical properties of crystalline and amorphous TiO_2," *Physical Review B*, vol. 86, no. 6, p. 064201, 2012.

[31] K. K. Ghuman and C. V. Singh, "Effect of doping on electronic structure and photocatalytic behavior of amorphous TiO_2," *Journal of Physics: Condensed Matter*, vol. 25, no. 47, p. 475501, 2013.

[32] J. Zhu and Z. Liu, "Structure and dielectric properties of ultra-thin ZrO_2 films for high-k gate dielectric application prepared by pulsed laser deposition," *Applied Physics A: Materials Science & Processing*, vol. 78, no. 5, pp. 741–744, 2004.

[33] M. D. Groner, F. H. Fabreguette, J. W. Elam, and S. M. George, "Low-Temperature Al_2O_3 Atomic Layer Deposition," *Chemistry of Materials*, vol. 16, no. 4, pp. 639–645, 2004.

[34] M. M. Frank, G. D. Wilk, D. Starodub, T. Gustafsson, E. Garfunkel, Y. J. Chabal, J. Grazul, and D. A. Muller, "HfO_2 and Al_2O_3 gate dielectrics on GaAs grown by atomic layer deposition," *Applied Physics Letters*, vol. 86, no. 15, p. 152904, 2005.

[35] E. O. Filatova and A. S. Konashuk, "Interpretation of the Changing the Band Gap of Al_2O_3 Depending on Its Crystalline Form: Connection with Different Local Symmetries," *Journal of Physical Chemistry C*, vol. 119, no. 35, pp. 20755–20761, 2015.

[36] H. Qin, P. Sutter, and G. Zhou, “The Crystallization of Amorphous Aluminum Oxide Thin Films Grown on NiAl(100),” *Journal of the American Ceramic Society*, vol. 97, no. 9, pp. 2762–2769, 2014.

[37] C. Freysoldt, B. Grabowski, T. Hickel, J. Neugebauer, G. Kresse, A. Janotti, and C. G. Van De Walle, “First-principles calculations for point defects in solids,” *Reviews of Modern Physics*, vol. 86, no. 1, pp. 253–305, 2014.

[38] P. Lamparter and R. Kniep, “Structure of amorphous Al_20_3,” *Physica B*, vol. 236, pp. 405–406, 1997.

[39] S. Lee, S. Park, Y. Yi, and C. Ahn, “Structure of Amorphous Aluminum Oxide,” *Physical Review Letters*, vol. 103, no. 9, p. 095501, 2009.

[40] M. Guidon, J. Hutter, and J. VandeVondele, “Robust periodic Hartree-Fock exchange for large-scale simulations using Gaussian basis sets,” *Journal of Chemical Theory and Computation*, vol. 5, pp. 3010–3021, 2009.

[41] B. Govoreanu, D. Wellekens, L. Haspeslagh, J. De Vos, and J. Van Houdt, “Investigation of the low-field leakage through high-k interpoly dielectric stacks and its impact on nonvolatile memory data retention,” *Technical Digest - International Electron Devices Meeting, IEDM*, 2006.

[42] Y. N. Novikov, V. A. Gritsenko, and K. A. Nasyrov, “Charge transport mechanism in amorphous alumina,” *Applied Physics Letters*, vol. 94, no. 22, p. 222904, 2009.

[43] D. Yamasaka, K. Tamagawa, and Y. Ohki, “Effects of ultraviolet photon irradiation on the transition metal impurities in $LaAlO_3$,” *Journal of Applied Physics*, vol. 110, no. 7, p. 074103, 2011.

[44] J. VandeVondele, M. Krack, F. Mohamed, M. Parrinello, T. Chassaing, and J. Hutter, “Quickstep: Fast and accurate density functional calculations using a mixed Gaussian and plane waves approach,” *Computer Physics Communication*, vol. 167, no. 2, pp. 103–128, 2005.

[45] L. Bläckberg, E. Metsanurk, A. Tamm, A. Aabloo, and M. Klintenberg, “Molecular dynamics study of xenon on an amorphous Al_2O_3 surface,” *Nuclear Instruments and Methods in Physics Research Section A: Accelerators, Spectrometers, Detectors and Associated Equipment*, vol. 759, pp. 10–15, 2014.

[46] G. Gutiérrez and B. Johansson, “Molecular dynamics study of structural properties of amorphous Al_2O_3,” *Physical Review B*, vol. 65, no. 10, p. 104202, 2002.

[47] P. P. Ewald, “Die berechnung optischer und elektrostatischer gitterpotentiale,” *Annalen der Physik*, vol. 369, no. 3, pp. 253–287, 1921.

[48] L. Verlet, “Computer “Experiments” on Classical Fluids. I. Thermodynamical Properties of Lennard-Jones Molecules,” *Physical Review*, vol. 159, no. 1, pp. 98–103, 1967.

[49] P. Hohenberg and W. Kohn, “Inhomogeneous Electron Gas,” *Physical Review*, vol. 136, no. 3B, pp. B864–B871, 1964.

[50] W. Kohn and L. J. Sham, “Self-Consistent Equations Including Exchange and Correlation Effects,” *Physical Review*, vol. 140, pp. A1133–A1138, 1965.

[51] K. Burke and L. O. Wagner, “DFT in a nutshell,” *International Journal of Quantum Chemistry*, vol. 113, pp. 96–101, 2013.

[52] K. Burke, “Perspective on density functional theory,” *The Journal of Chemical Physics*, vol. 136, p. 150901, 2012.

[53] J. D. Pack and H. J. Monkhorst, “”Special points for Brillouin-zone integrations”a reply,” *Physical Review B*, vol. 16, no. 4, pp. 1748–1749, 1977.

[54] B. G. Lippert, J. H. Parrinello, and Michele, “A hybrid Gaussian and plane wave density functional scheme,” *Molecular Physics*, vol. 92, no. 3, pp. 477–488, 1997.

[55] S. Goedecker, M. Teter, and J. Hutter, “Separable dual-space Gaussian pseudopotentials,” *Physical Review B*, vol. 54, no. 3, pp. 1703–1710, 1996.

[56] C. Hartwigsen, S. Goedecker, and J. Hutter, “Relativistic separable dual-space Gaussian pseudopotentials from H to Rn,” *Physical Review B*, vol. 58, no. 7, pp. 3641–3662, 1998.

[57] J. P. Perdew, M. Ernzerhof, and K. Burke, “Rationale for mixing exact exchange with density functional approximations,” *Journal of Chemical Physics*, vol. 105, no. 1996, p. 9982, 1996.

[58] M. Ernzerhof, J. P. Perdew, and K. Burke, “Coupling-constant dependence of atomization energies,” *International Journal of Quantum Chemistry*, vol. 64, no. 3, pp. 285–295, 1997.

[59] J. Spencer and A. Alavi, “Efficient calculation of the exact exchange energy in periodic systems using a truncated Coulomb potential,” *Physical Review B*, vol. 77, no. 19, p. 193110, 2008.

[60] J. Heyd, G. E. Scuseria, and M. Ernzerhof, “Hybrid functionals based on a screened Coulomb potential,” *The Journal of Chemical Physics*, vol. 118, no. 18, p. 8207, 2003.

[61] J. Heyd, G. E. Scuseria, and M. Ernzerhof, “Hybrid functionals based on a screened Coulomb potential,” *The Journal of Chemical Physics*, vol. 118, no. 18, p. 8207, 2003.

[62] A. V. Krukau, O. A. Vydrov, A. F. Izmaylov, and G. E. Scuseria, “Influence of the exchange screening parameter on the performance of screened hybrid functionals,” *Journal of Chemical Physics*, vol. 125, no. 22, 2006.

[63] S. Lany and A. Zunger, “Assessment of correction methods for the band-gap problem and for finite-size effects in supercell defect calculations: Case studies for ZnO and GaAs,” *Physical Review B*, vol. 78, no. 23, p. 235104, 2008.

[64] S. Lany and A. Zunger, "Accurate prediction of defect properties in density functional supercell calculations," *Modelling and Simulation in Materials Science and Engineering*, vol. 17, p. 084002, 2009.

[65] H.-P. Komsa, T. T. Rantala, and A. Pasquarello, "Finite-size supercell correction schemes for charged defect calculations," *Physical Review B*, vol. 86, no. 4, p. 045112, 2012.

[66] R. W. Grimes, C. R. A. Catlow, and A. M. Stoneham, "A comparison of defect energies in MgO using Mott-Littleton and quantum mechanical procedures," *Journal of Physics: Condensed Matter*, vol. 1, no. 40, pp. 7367–7384, 1989.

[67] N. F. Mott and M. J. Littleton, "Conduction in polar crystals. I. Electrolytic conduction in solid salts," *Transactions of the Faraday Society*, vol. 34, p. 485, 1938.

[68] G. Henkelman and H. Jónsson, "Improved tangent estimate in the nudged elastic band method for finding minimum energy paths and saddle points," *Journal of Chemical Physics*, vol. 113, no. 22, pp. 9978–9985, 2000.

[69] E. Runge and E. K. U. Gross, "Density-Functional Theory for Time-Dependent Systems," *Physical Review Letters*, vol. 52, no. 12, pp. 997–1000, 1984.

[70] M. A. L. Marques and E. K. U. Gross, "Time-dependent density functional theory," *Annual Review of Physical Chemistry*, vol. 55, pp. 427–455, 2004.

[71] M. E. Casida, "Journal of Molecular Structure : THEOCHEM Time-dependent density-functional theory for molecules and molecular solids," *Journal of Molecular Structure: THEOCHEM*, vol. 914, no. 1-3, pp. 3–18, 2009.

[72] S. Hirata and M. Head-Gordon, "Time-dependent density functional theory within the Tamm-Dancoff approximation," *Chemical Physics Letters*, vol. 314, no. 3,4, pp. 291–299, 1999.

[73] S. Gariglio, A. Fête, and J.-M. Triscone, "Electron confinement at the $LaAlO_3/SrTiO_3$ interface," *Journal of Physics: Condensed Matter*, vol. 27, no. 28, p. 283201, 2015.

[74] S.-G. Lim, S. Kriventsov, T. N. Jackson, J. H. Haeni, D. G. Schlom, A. M. Balbashov, R. Uecker, P. Reiche, J. L. Freeouf, and G. Lucovsky, "Dielectric functions and optical bandgaps of high-K dielectrics for metal-oxide-semiconductor field-effect transistors by far ultraviolet spectroscopic ellipsometry," *Journal of Applied Physics*, vol. 91, no. 7, p. 4500, 2002.

[75] E. Cicerrella, J. L. Freeouf, L. F. Edge, D. G. Schlom, T. Heeg, J. Schubert, and S. A. Chambers, "Optical properties of La-based high-K dielectric films," *Journal of Vacuum Science & Technology A: Vacuum, Surfaces, and Films*, vol. 23, p. 1676, 2005.

[76] M. Suzuki, T. Yamaguchi, N. Fukushima, and M. Koyama, "$LaAlO_3$ gate dielectric with ultrathin equivalent oxide thickness and ultralow leakage current directly deposited on Si substrate," *Journal of Applied Physics*, vol. 103, p. 034118, 2008.

[77] Y. Y. Mi, Z. Yu, S. J. Wang, P. C. Lim, Y. L. Foo, A. C. H. Huan, and C. K. Ong, "Epitaxial $LaAlO_3$ thin film on silicon: Structure and electronic properties," *Applied Physics Letters*, vol. 90, p. 181925, 2007.

[78] Z. Q. Liu, L. Sun, Z. Huang, C. J. Li, S. W. Zeng, K. Han, W. M. Lü, and T. Venkatesan, "Dominant role of oxygen vacancies in electrical properties of unannealed $LaAlO_3/SrTiO_3$ interfaces," *Journal of Applied Physics*, vol. 115, p. 054303, 2014.

[79] C. J. Howard, B. J. Kennedy, and B. C. Chakoumakos, "Neutron powder diffraction study of rhombohedral rare-earth aluminates and the rhombo-

hedral to cubic phase transition," *Journal of Physics: Condensed Matter*, vol. 12, pp. 349–365, 2000.

[80] J. Wang, N. Ishizawa, and X. Ye, "Phase transition and thermal expansion of the LaAlO3 single crystal at high temperatures," *Journal of Alloys and Compounds*, vol. 594, pp. 23–26, 2014.

[81] R. L. Johnson-Wilke, D. Marincel, S. Zhu, M. P. Warusawithana, A. Hatt, J. Sayre, K. T. Delaney, R. Engel-Herbert, C. M. Schlepütz, J.-W. Kim, V. Gopalan, N. A. Spaldin, D. G. Schlom, P. J. Ryan, and S. Trolier-McKinstry, "Quantification of octahedral rotations in strained $LaAlO_3$ films via synchrotron x-ray diffraction," *Physical Review B*, vol. 88, p. 174101, 2013.

[82] J. Park, Y.-A. Soh, G. Aeppli, A. David, W. Lin, and T. Wu, "Influence of oxygen pressure and aging on $LaAlO_3$ films grown by pulsed laser deposition on $SrTiO_3$ substrates," *Applied Physics Letters*, vol. 104, p. 081604, 2014.

[83] A. N. Meza-Rocha, E. Zaleta-Alejandre, J. G. Cabanas-Moreno, S. Gallardo-Hernandez, Z. Rivera-Alvarez, M. Aguilar-Frutis, and C. Falcony, "Characterization of Lanthanum-Aluminum Oxide Thin Films Deposited by Spray Pyrolysis," *ECS Journal of Solid State Science and Technology*, vol. 3, no. 2, pp. N1–N6, 2014.

[84] Y. Kawabe, A. Yamanaka, E. Hanamura, T. Kimura, Y. Takiguchi, H. Kan, and Y. Tokura, "Photoluminescence of perovskite lanthanum aluminate single crystals," *Journal of Applied Physics*, vol. 88, no. 2, p. 1175, 2000.

[85] J. Q. Chen, X. Wang, Y. H. Lu, A. Roy Barman, G. J. You, G. C. Xing, T. C. Sum, S. Dhar, Y. P. Feng, Q.-H. Xu, and T. Venkatesan, "Defect dynamics and spectral observation of twinning in single crystalline $LaAlO_3$ under sub bandgap excitation," *Applied Physics Letters*, vol. 98, no. 4, p. 041904, 2011.

[86] V. Singh, S. Watanabe, T. G. Rao, J. Chubaci, and H.-Y. Kwak, "Characterization, photoluminescence, thermally stimulated luminescence and electron

spin resonance studies of Eu^{3+} doped $LaAlO_3$ phosphor," *Solid State Sciences*, vol. 13, pp. 66–71, 2011.

[87] K. Xiong, J. Robertson, and S. J. Clark, "Defect states in the high-dielectric-constant gate oxide $LaAlO_3$," *Applied Physics Letters*, vol. 89, p. 022907, 2006.

[88] X. Luo, B. Wang, and Y. Zheng, "First-principles study on energetics of intrinsic point defects in $LaAlO_3$," *Physical Review B*, vol. 80, p. 104115, 2009.

[89] C. Mitra, C. Lin, J. Robertson, and A. Demkov, "Electronic structure of oxygen vacancies in $SrTiO_3$ and $LaAlO_3$," *Physical Review B*, vol. 86, p. 155105, 2012.

[90] F. El-Mellouhi, E. Brothers, M. Lucero, and G. Scuseria, "Role of screened exact exchange in accurately describing properties of transition metal oxides: Modeling defects in LaAlO3," *Physical Review B*, vol. 88, p. 214102, 2013.

[91] M. Choi, A. Janotti, and C. G. Van de Walle, "Native point defects in $LaAlO_3$: A hybrid functional study," *Physical Review B*, vol. 88, p. 214117, 2013.

[92] M. J. Frisch, G. W. Trucks, H. B. Schlegel, G. E. Scuseria, M. A. Robb, J. R. Cheeseman, G. Scalmani, V. Barone, B. Mennucci, G. A. Petersson, H. Nakatsuji, M. Caricato, X. Li, H. P. Hratchian, A. F. Izmaylov, J. Bloino, G. Zheng, J. L. Sonnenberg, M. Hada, M. Ehara, K. Toyota, R. Fukuda, J. Hasegawa, M. Ishida, T. Nakajima, Y. Honda, O. Kitao, H. Nakai, T. Vreven, J. A. Montgomery, Jr., J. E. Peralta, F. Ogliaro, M. Bearpark, J. J. Heyd, E. Brothers, K. N. Kudin, V. N. Staroverov, R. Kobayashi, J. Normand, K. Raghavachari, A. Rendell, J. C. Burant, S. S. Iyengar, J. Tomasi, M. Cossi, N. Rega, J. M. Millam, M. Klene, J. E. Knox, J. B. Cross, V. Bakken, C. Adamo, J. Jaramillo, R. Gomperts, R. E. Stratmann, O. Yazyev, A. J. Austin, R. Cammi, C. Pomelli, J. W. Ochterski, R. L. Martin, K. Morokuma, V. G. Zakrzewski, G. A. Voth, P. Salvador, J. J. Dannenberg, S. Dapprich,

A. D. Daniels, O. Farkas, J. B. Foresman, J. V. Ortiz, J. Cioslowski, and D. J. Fox, "Gaussian09 revision a.02." Gaussian Inc. Wallingford CT 2009.

[93] D. Muñoz Ramo, P. V. Sushko, J. L. Gavartin, and A. L. Shluger, "Oxygen vacancies in cubic ZrO_2 nanocrystals studied by an ab initio embedded cluster method," *Physical Review B*, vol. 78, p. 235432, 2008.

[94] I. V. Abarenkov, "Unit cell for a lattice electrostatic potential," *Physical Review B*, vol. 76, p. 165127, 2007.

[95] P. V. Sushko and I. V. Abarenkov, "General purpose electrostatic embedding potential," *Journal of Chemical Theory and Computation*, vol. 6, pp. 1323–1333, 2010.

[96] J. M. Vail, A. H. Harker, J. H. Harding, and P. Saul, "Calculations for electronic point defects with self-consistent lattice polarisation: the F + centre in MgO," *Journal of Physics C: Solid State Physics*, vol. 17, no. 19, pp. 3401–3414, 1984.

[97] R. Krishnan, J. S. Binkley, R. Seeger, and J. A. Pople, "Self-consistent molecular orbital methods. XX. A basis set for correlated wave functions," *The Journal of Chemical Physics*, vol. 72, no. 1, p. 650, 1980.

[98] A. D. McLean and G. S. Chandler, "Contracted Gaussian basis sets for molecular calculations. I. Second row atoms, Z=11-18," *The Journal of Chemical Physics*, vol. 72, no. 10, p. 5639, 1980.

[99] P. J. Hay and W. R. Wadt, "Ab initio effective core potentials for molecular calculations. Potentials for K to Au including the outermost core orbitals," *The Journal of Chemical Physics*, vol. 82, no. 1, 1985.

[100] P. J. Hay and W. R. Wadt, "Ab initio effective core potentials for molecular calculations. Potentials for the transition metal atoms Sc to Hg," *The Journal of Chemical Physics*, vol. 82, no. 1, 1985.

[101] K. L. Schuchardt, B. T. Didier, T. Elsethagen, L. Sun, V. Gurumoorthi, J. Chase, J. Li, and T. L. Windus, “Basis set exchange: a community database for computational sciences,” *Journal of Chemical Information and Modeling*, vol. 47, no. 3, pp. 1045–1052, 2007.

[102] J. Heyd, G. E. Scuseria, and M. Ernzerhof, “Erratum: Hybrid functionals based on a screened Coulomb potential [J. Chem. Phys. 118, 8207 (2003)],” *The Journal of Chemical Physics*, vol. 124, p. 219906, 2006.

[103] J. VandeVondele and J. Hutter, “Gaussian basis sets for accurate calculations on molecular systems in gas and condensed phases,” *The Journal of Chemical Physics*, vol. 127, no. 11, p. 114105, 2007.

[104] A. Popov, E. Kotomin, and J. Maier, “Basic properties of the F-type centers in halides, oxides and perovskites,” *Nuclear Instruments and Methods in Physics Research Section B: Beam Interactions with Materials and Atoms*, vol. 268, no. 19, pp. 3084–3089, 2010.

[105] Y. Zhukovskii, E. Kotomin, S. Piskunov, and D. Ellis, “A comparative ab initio study of bulk and surface oxygen vacancies in $PbTiO_3$, $PbZrO_3$ and $SrTiO_3$ perovskites,” *Solid State Communications*, vol. 149, no. 33-34, pp. 1359–1362, 2009.

[106] A. Stoneham, J. Gavartin, A. Shluger, A. Kimmel, D. Muñoz Ramo, H. M. Rønnow, G. Aeppli, and C. Renner, “Trapping, self-trapping and the polaron family,” *Journal of Physics: Condensed Matter*, vol. 19, no. 25, p. 255208, 2007.

[107] A. S. Foster, F. L. Gejo, A. L. Shluger, and R. M. Nieminen, “Vacancy and interstitial defects in hafnia,” *Physical Review B*, vol. 65, p. 174117, 2002.

[108] A. S. Foster, V. B. Sulimov, F. L. Gejo, A. L. Shluger, and R. M. Nieminen, “Structure and electrical levels of point defects in monoclinic zirconia,” *Physical Review B*, vol. 64, no. 22, p. 224108, 2001.

[109] S. Swaminathan, Y. Sun, P. Pianetta, and P. C. McIntyre, "Ultrathin ALD-Al_2O_3 layers for Ge(001) gate stacks: Local composition evolution and dielectric properties," *Journal of Applied Physics*, vol. 110, no. 9, p. 094105, 2011.

[110] L. Jeurgens, W. Sloof, F. Tichelaar, and E. Mittemeijer, "Thermodynamic stability of amorphous oxide films on metals: Application to aluminum oxide films on aluminum substrates," *Physical Review B*, vol. 62, no. 7, pp. 4707–4719, 2000.

[111] K. Henkel, M. Kot, and D. Schmeißer, "Localized defect states and charge trapping in atomic layer deposited-Al_2O_3 films," *Journal of Vacuum Science & Technology A: Vacuum, Surfaces, and Films*, vol. 35, no. 1, p. 01B125, 2017.

[112] R. H. French, "Electronic Band Structure of Al_2O_3, with Comparison to Alon and AIN," *Journal of the American Ceramic Society*, vol. 73, pp. 477–489, 1990.

[113] V. V. Afanas'ev, A. Stesmans, and W. Tsai, "Determination of interface energy band diagram between (100)Si and mixed Al-Hf oxides using internal electron photoemission," *Applied Physics Letters*, vol. 82, no. 2, pp. 245–247, 2003.

[114] M. L. Huang, Y. C. Chang, C. H. Chang, T. D. Lin, J. Kwo, T. B. Wu, and M. Hong, "Energy-band parameters of atomic-layer-deposition Al_2O_3/InGaAs heterostructure," *Applied Physics Letters*, vol. 89, no. 1, p. 012903, 2006.

[115] N. V. Nguyen, O. A. Kirillov, W. Jiang, W. Wang, J. S. Suehle, P. D. Ye, Y. Xuan, N. Goel, K.-W. Choi, W. Tsai, and S. Sayan, "Band offsets of atomic-layer-deposited Al_2O_3 on GaAs and the effects of surface treatment," *Applied Physics Letters*, vol. 93, no. 8, p. 082105, 2008.

[116] J. Ahn, I. Geppert, M. Gunji, M. Holland, I. Thayne, M. Eizenberg, and P. C. McIntyre, “Titania/alumina bilayer gate insulators for InGaAs metal-oxide-semiconductor devices,” *Applied Physics Letters*, vol. 99, no. 23, p. 232902, 2011.

[117] I. Krylov, D. Ritter, and M. Eizenberg, “The physical origin of dispersion in accumulation in InGaAs based metal oxide semiconductor gate stacks,” *Journal of Applied Physics*, vol. 117, no. 17, p. 174501, 2015.

[118] H. Momida, T. Hamada, Y. Takagi, T. Yamamoto, T. Uda, and T. Ohno, “Theoretical study on dielectric response of amorphous alumina,” *Physical Review B*, vol. 73, no. 5, p. 054108, 2006.

[119] V. V. Afanas’Ev, M. Houssa, A. Stesmans, C. Merckling, T. Schram, and J. A. Kittl, “Influence of Al_2O_3 crystallization on band offsets at interfaces with Si and TiN_x,” *Applied Physics Letters*, vol. 99, no. 7, p. 072103, 2011.

[120] J. Laegsgaard and K. Stokbro, “Hole Trapping at Al impurities in Silica: A Challenge for Density Functional Theories,” *Physical Review Letters*, vol. 86, no. 13, pp. 2834–2837, 2001.

[121] G. Pacchioni, F. Frigoli, and D. Ricci, “Theoretical description of hole localization in a quartz Al center: The importance of exact electron exchange,” *Physical Review B*, vol. 63, no. 5, p. 054102, 2000.

[122] J. Gavartin, P. Sushko, and A. Shluger, “Modeling charge self-trapping in wide-gap dielectrics: Localization problem in local density functionals,” *Physical Review B*, vol. 67, p. 035108, 2003.

[123] A. J. Cohen, P. Mori-Sanchez, and W. Yang, “Challenges for Density Functional Theory,” *Chemical Reviews*, vol. 112, no. 1, pp. 289–320, 2012.

[124] A.-M. El-Sayed, M. B. Watkins, V. V. Afanas’ev, and A. L. Shluger, “Nature of intrinsic and extrinsic electron trapping in SiO_2,” *Physical Review B*, vol. 89, no. 12, p. 125201, 2014.

[125] S. Plimpton, "Fast parallel algorithms for short-range molecular-dynamics," *Journal of Computational Physics*, vol. 117, no. 1, pp. 1–19, 1995.

[126] M. Guidon, J. Hutter, and J. VandeVondele, "Auxiliary Density Matrix Methods for HartreeFock Exchange Calculations," *Journal of Chemical Theory and Computation*, vol. 6, no. 8, pp. 2348–2364, 2010.

[127] A. L. Shluger, V. E. Puchin, T. Suzuki, K. Tanimura, and N. Itoh, "Optical transitions of the H centers in alkali halides," *Physical Review B*, vol. 52, no. 6, pp. 4017–4028, 1995.

[128] A. J. Fisher, W. Hayes, and A. M. Stoneham, "Theory of the structure of the self-trapped exciton in quartz," *Journal of Physics: Condensed Matter*, vol. 2, no. 32, pp. 6707–6720, 1990.

[129] A. L. Shluger, E. A. Kotomin, and L. N. Kantorovich, "Quantum-chemical simulation of impurity-induced trapping of a hole: (Li) 0 centre in MgO," *Journal of Physics C: Solid State Physics*, vol. 19, no. 22, pp. 4183–4199, 1986.

[130] A. L. Shluger, E. N. Heifets, J. D. Gale, and C. R. A. Catlow, "Theoretical simulation of localized holes in MgO," *Journal of Physics: Condensed Matter*, vol. 4, no. 26, pp. 5711–5722, 1992.

[131] A. V. Kimmel, P. V. Sushko, and A. L. Shluger, "Structure and spectroscopic properties of trapped holes in silica," *Journal of Non-Crystalline Solids*, vol. 353, pp. 599–604, 2007.

[132] S. Sicolo, G. Palma, C. Di Valentin, and G. Pacchioni, "Structure and ESR properties of self-trapped holes in pure silica from first-principles density functional calculations," *Physical Review B*, vol. 76, no. 7, p. 075121, 2007.

[133] T. Maxisch, F. Zhou, and G. Ceder, "Ab initio study of the migration of small polarons in olivine Li_xFePO_4 and their association with lithium ions and vacancies," *Physical Review B*, vol. 73, no. 10, p. 104301, 2006.

[134] N. A. Deskins and M. Dupuis, “Electron transport via polaron hopping in bulk TiO_2: A density functional theory characterization,” *Physical Review B*, vol. 75, no. 19, p. 195212, 2007.

[135] S. Lany and A. Zunger, “Polaronic hole localization and multiple hole binding of acceptors in oxide wide-gap semiconductors,” *Physical Review B*, vol. 80, no. 8, p. 085202, 2009.

[136] P. Erhart, A. Klein, D. Åberg, and B. Sadigh, “Efficacy of the DFT formalism for modeling hole polarons in perovskite oxides,” *Physical Review B*, vol. 90, no. 3, p. 035204, 2014.

[137] J. P. Perdew, A. Ruzsinszky, L. A. Constantin, J. Sun, and G. I. Csonka, “Some Fundamental Issues in Ground-State Density Functional Theory: A Guide for the Perplexed,” *Journal of Chemical Theory and Computation*, vol. 5, no. 4, pp. 902–908, 2009.

[138] V. Atalla, I. Y. Zhang, O. T. Hofmann, X. Ren, P. Rinke, and M. Scheffler, “Enforcing the linear behavior of the total energy with hybrid functionals: Implications for charge transfer, interaction energies, and the random-phase approximation,” *Physical Review B*, vol. 94, no. 3, p. 035140, 2016.

[139] A. Karolewski, L. Kronik, and S. Kümmel, “Using optimally tuned range separated hybrid functionals in ground-state calculations: Consequences and caveats,” *Journal of Chemical Physics*, vol. 138, no. 20, 2013.

[140] J. Autschbach and M. Srebro, “Delocalization Error and “Functional Tuning” in Kohn-Sham Calculations of Molecular Properties,” *Accounts of Chemical Research*, vol. 47, no. 8, pp. 2592–2602, 2014.

[141] J. P. Perdew, R. G. Parr, M. Levy, and J. L. Balduz, “Density-functional theory for fractional particle number: Derivative discontinuities of the energy,” *Physical Review Letters*, vol. 49, no. 23, pp. 1691–1694, 1982.

[142] L. Kronik, T. Stein, S. Refaely-Abramson, and R. Baer, “Excitation Gaps of Finite-Sized Systems from Optimally Tuned Range-Separated Hybrid Functionals,” *Journal of Chemical Theory and Computation*, vol. 8, no. 5, pp. 1515–1531, 2012.

[143] V. Vlček, H. R. Eisenberg, G. Steinle-Neumann, L. Kronik, and R. Baer, “Deviations from piecewise linearity in the solid-state limit with approximate density functionals,” *Journal of Chemical Physics*, vol. 142, no. 3, 2015.

[144] L. Lutterotti and P. Scardi, “Simultaneous structure and sizestrain refinement by the Rietveld method,” *Journal of Applied Crystallography*, vol. 23, no. 4, pp. 246–252, 1990.

[145] T. J. Godin and J. P. Lafemina, “Atomic and electronic structure of the corundum (α-alumina) (0001) surface,” *Physical Review B*, vol. 49, no. 11, pp. 7691–7696, 1994.

[146] D. Liu, S. Clark, and J. Robertson, “Oxygen vacancy levels and electron transport in Al_2O_3,” *Applied Physics Letters*, vol. 96, p. 032905, 2010.

[147] C.-K. Lee, E. Cho, H.-S. Lee, K. S. Seol, and S. Han, “Comparative study of electronic structures and dielectric properties of alumina polymorphs by first-principles methods,” *Physical Review B*, vol. 76, no. 24, p. 245110, 2007.

[148] B. Ilic, S. Krylov, and H. G. Craighead, “Young’s modulus and density measurements of thin atomic layer deposited films using resonant nanomechanics,” *Journal of Applied Physics*, vol. 108, no. 4, p. 044317, 2010.

[149] V. V. Afanas’Ev, A. Stesmans, B. J. Mrstik, and C. Zhao, “Impact of annealing-induced compaction on electronic properties of atomic-layer-deposited Al_2O_3,” *Applied Physics Letters*, vol. 81, no. 9, pp. 1678–1680, 2002.

[150] P. C. Snijders, L. P. H. Jeurgens, and W. G. Sloof, “Structural ordering of ultra-thin, amorphous aluminium-oxide films,” *Surface Science*, vol. 589, no. 1-3, pp. 98–105, 2005.

[151] R. Bell and P. Dean, “Atomic vibrations in vitreous silica,” *Discussions of the Faraday Society*, no. 50, p. 55, 1971.

[152] T. M. Chang, J. D. Bauer, and J. L. Skinner, “Critical exponents for Anderson localization,” *The Journal of Chemical Physics*, vol. 93, no. 12, pp. 8973–8982, 1990.

[153] J. Dong and D. Drabold, “Band-tail states and the localized-to-extended transition in amorphous diamond,” *Physical Review B*, vol. 54, no. 15, pp. 10284–10287, 1996.

[154] M. Unge and T. Christen, “Electron and hole mobility edges in polyethylene from material simulations,” *Chemical Physics Letters*, vol. 613, pp. 15–18, oct 2014.

[155] Y. Youn, Y. Kang, and S. Han, “An efficient method to generate amorphous structures based on local geometry,” *Computational Materials Science*, vol. 95, pp. 256–262, 2014.

[156] N. Mott, “The mobility edge since 1967,” *Journal of Physics C: Solid State Physics*, vol. 3075, no. 21, pp. 3075–3102, 1987.

[157] J. Dong and D. Drabold, “Atomistic Structure of Band-Tail States in Amorphous Silicon,” *Physical Review Letters*, vol. 80, no. 9, pp. 1928–1931, 1998.

[158] F. P. Sabino, R. Besse, L. N. Oliveira, S.-H. Wei, and J. L. F. Da Silva, “Origin of and tuning the optical and fundamental band gaps in transparent conducting oxides: The case of M_2O_3 (M = Al,Ga,In),” *Physical Review B*, vol. 92, no. 20, p. 205308, 2015.

[159] T. B. Boykin, N. Kharche, G. Klimeck, and M. Korkusinski, “Approximate bandstructures of semiconductor alloys from tight-binding supercell calculations,” *Journal of Physics: Condensed Matter*, vol. 19, no. 3, p. 036203, 2007.

[160] V. V. Afanas’ev and A. Stesmans, “Hole trapping in ultrathin Al_2O_3 and ZrO_2 insulators on silicon,” *Applied Physics Letters*, vol. 80, no. 7, pp. 1261–1263, 2002.

[161] Y. F. Zhukovskii, E. A. Kotomin, R. M. Nieminen, and A. Stashans, “Quantum-chemical simulations of free and bound hole polarons in corundum crystal,” *Computational Materials Science*, vol. 7, no. 3, pp. 285–294, 1997.

[162] J. B. Varley, A. Janotti, C. Franchini, and C. G. Van de Walle, “Role of self-trapping in luminescence and p-type conductivity of wide-band-gap oxides,” *Physical Review B*, vol. 85, no. 8, p. 081109, 2012.

[163] D. Muñoz Ramo, A. L. Shluger, J. L. Gavartin, and G. Bersuker, “Theoretical prediction of intrinsic self-trapping of electrons and holes in monoclinic HfO_2,” *Physical Review Letters*, vol. 99, p. 155504, 2007.

[164] K. P. McKenna, M. J. Wolf, A. L. Shluger, S. Lany, and A. Zunger, “Two-Dimensional Polaronic Behavior in the Binary Oxides m-$HfO_2$and m-ZrO_2,” *Physical Review Letters*, vol. 108, no. 11, p. 116403, 2012.

[165] A. Lindman, P. Erhart, and G. Wahnström, “Polaronic contributions to oxidation and hole conductivity in acceptor-doped $BaZrO_3$,” *Physical Review B*, vol. 94, no. 7, p. 075204, 2016.

[166] A. J. E. Rettie, W. D. Chemelewski, D. Emin, and C. B. Mullins, “Unravelling small-polaron transport in metal oxide photoelectrodes,” *The Journal of Physical Chemistry Letters*, vol. 7, no. 3, pp. 471–479, 2016.

[167] D. L. Griscom, "Self-trapped holes in pure-silica glass: A history of their discovery and characterization and an example of their critical significance to industry," *Journal of Non-Crystalline Solids*, vol. 352, no. 23-25, pp. 2601–2617, 2006.

[168] F. Cerbu, O. Madia, D. V. Andreev, S. Fadida, M. Eizenberg, L. Breuil, J. G. Lisoni, J. A. Kittl, J. Strand, A. L. Shluger, V. V. Afanas'Ev, M. Houssa, and A. Stesmans, "Intrinsic electron traps in atomic-layer deposited HfO_2 insulators," *Applied Physics Letters*, vol. 108, no. 22, p. 222901, 2016.

[169] M. Farnesi Camellone, T. D. Kühne, and D. Passerone, "Density functional theory study of self-trapped holes in disordered SiO_2," *Physical Review B*, vol. 80, no. 3, p. 033203, 2009.

[170] H. Wang, C. Lee, and F. Kröger, "Point defects in Al_2O_3: Mg studied by electrical conductivity optical absorption and ESR," *Physical Review B*, vol. 27, no. 6, pp. 3821–3841, 1983.

[171] R. Cox, "Electron spin resonance studies of holes trapped at Mg^{2+}, Li^{+} and cation vacancies in Al_2O_3," *Solid State Communications*, vol. 9, no. 22, pp. 1989–1992, 1971.

[172] R. C. Duvarney, J. R. Niklas, and J.-M. Spaeth, "Electron Nuclear Double Resonance of the Trapped Hole Center in α-Al_2O_3:Mg^{2+}," *Physica Status Solidi (b)*, vol. 128, pp. 673–681, 1985.

[173] F. J. Adrian, A. N. Jette, and J. M. Spaeth, "Theory of indirect hyperfine interactions of oxygen-aluminum defects in ionic crystals," *Physical Review B*, vol. 31, no. 6, pp. 3923–3931, 1985.

[174] F. Jensen, "Polarization consistent basis sets. IV. The basis set convergence of equilibrium geometries, harmonic vibrational frequencies, and intensities," *The Journal of Chemical Physics*, vol. 118, no. 6, p. 2459, 2003.

[175] F. Jensen, "Polarization Consistent Basis Sets. 4: The Elements He, Li, Be, B, Ne, Na, Mg, Al, and Ar ," *The Journal of Physical Chemistry A*, vol. 111, no. 44, pp. 11198–11204, 2007.

[176] F. Jensen, "The Basis Set Convergence of SpinSpin Coupling Constants Calculated by Density Functional Methods," *Journal of Chemical Theory and Computation*, vol. 2, no. 5, pp. 1360–1369, 2006.

[177] F. Jensen, "Basis Set Convergence of Nuclear Magnetic Shielding Constants Calculated by Density Functional Methods," *Journal of Chemical Theory and Computation*, vol. 4, no. 5, pp. 719–727, 2008.

[178] M. Iannuzzi, T. Chassaing, T. Wallman, and J. Hutter, "Ground and excited state density functional calculations with the gaussian and augmented-plane-wave method," *CHIMIA International Journal for Chemistry*, vol. 59, no. 7-8, 2005.

[179] C.-Y. Chang, F.-M. Pan, J.-S. Lin, T.-Y. Yu, Y.-M. Li, and C.-Y. Chen, "Lateral amorphous selenium metal-insulator-semiconductor-insulator-metal photodetectors using ultrathin dielectric blocking layers for dark current suppression," *Journal of Applied Physics*, vol. 120, no. 23, p. 234501, 2016.

[180] J. Strand, O. A. Dicks, M. Kaviani, and A. L. Shluger, "Hole trapping in amorphous HfO_2 and Al_2O_3 as a source of positive charging," *Microelectronic Engineering*, vol. 178, pp. 235–239, 2017.

[181] S. Chen and L. W. Wang, "Double-hole-induced oxygen dimerization in transition metal oxides," *Physical Review B*, vol. 89, no. 1, p. 014109, 2014.

[182] M. M. El-Aiat and F. A. Kröger, "Hydrogen donors in α-Al_2O_3," *Journal of Applied Physics*, vol. 53, no. 5, pp. 3658–3667, 1982.

[183] D. R. Jennison, P. A. Schultz, and J. P. Sullivan, "Evidence for interstitial hydrogen as the dominant electronic defect in nanometer alumina films," *Physical Review B*, vol. 69, no. 4, p. 041405, 2004.

[184] J. Strand, M. Kaviani, V. V. Afanasev, J. G. Lisoni, and A. L. Shluger, "Intrinsic Electron Trapping in Amorphous Oxides," *Physical Review Materials*, submitted.

[185] P. W. Peacock and J. Robertson, "Behavior of hydrogen in high dielectric constant oxide gate insulators," *Applied Physics Letters*, vol. 83, no. 10, pp. 2025–2027, 2003.

[186] J. R. Weber, A. Janotti, and C. G. Van de Walle, "Native defects in Al_2O_3 and their impact on III-V/Al_2O_3 metal-oxide-semiconductor-based devices," *Journal of Applied Physics*, vol. 109, no. 2011, p. 033715, 2011.

[187] A. M. Holder, K. D. Osborn, C. J. Lobb, and C. B. Musgrave, "Bulk and surface tunneling hydrogen defects in alumina," *Physical Review Letters*, vol. 111, p. 065901, 2013.

[188] L. Gordon, H. Abu-Farsakh, A. Janotti, and C. G. Van de Walle, "Hydrogen bonds in Al_2O_3 as dissipative two-level systems in superconducting qubits," *Scientific Reports*, vol. 4, p. 7590, 2014.

[189] H. Li and J. Robertson, "Behaviour of hydrogen in wide band gap oxides," *Journal of Applied Physics*, vol. 115, no. 20, p. 203708, 2014.

[190] Z. Guo, F. Ambrosio, and A. Pasquarello, "Oxygen defects in amorphous Al_2O_3: A hybrid functional study," *Applied Physics Letters*, vol. 109, no. 6, p. 062903, 2016.

[191] M. Kaviani, V. V. Afanas'ev, and A. L. Shluger, "Interactions of hydrogen with amorphous hafnium oxide," *Physical Review B*, vol. 95, no. 7, p. 075117, 2017.

[192] A.-M. El-Sayed, M. B. Watkins, T. Grasser, V. V. Afanas'ev, and A. L. Shluger, "Hydrogen-Induced Rupture of Strained SiO Bonds in Amorphous Silicon Dioxide," *Physical Review Letters*, vol. 114, no. 11, p. 115503, 2015.

[193] K. Shamala, L. Murthy, and K. Narasimha Rao, "Studies on optical and dielectric properties of Al_2O_3 thin films prepared by electron beam evaporation and spray pyrolysis method," *Materials Science and Engineering B*, vol. 106, pp. 269–274, 2004.

[194] C. G. Van De Walle, "Universal alignment of hydrogen levels in semiconductors and insulators," *Physica B: Condensed Matter*, vol. 423, p. 626, 2006.

[195] S. F. J. Cox, "The shallow-to-deep instability of hydrogen and muonium in II-VI and III-V semiconductors," *Journal of Physics: Condensed Matter*, vol. 15, no. 46, pp. R1727–R1780, 2003.

[196] A. M. El-Sayed, Y. Wimmer, W. Goes, T. Grasser, V. V. Afanas'Ev, and A. L. Shluger, "Theoretical models of hydrogen-induced defects in amorphous silicon dioxide," *Physical Review B*, vol. 92, no. 1, p. 014107, 2015.

[197] M. Choi, A. Janotti, and C. G. Van De Walle, "Native point defects and dangling bonds in α-Al_2O_3," *Journal of Applied Physics*, vol. 113, p. 044501, 2013.

[198] M. J. Springis and J. A. Valbis, "Visible Luminescence of Colour Centres in Sapphire," *Physica Status Solidi (b)*, vol. 123, no. 1, pp. 335–343, 1984.

[199] V. A. Pustovarov, V. S. Aliev, T. V. Perevalov, V. A. Gritsenko, and A. P. Eliseev, "Electronic structure of an oxygen vacancy in Al_2O_3 from the results of Ab Initio quantum-chemical calculations and photoluminescence experiments," *Journal of Experimental and Theoretical Physics*, vol. 111, no. 6, pp. 989–995, 2010.

[200] D. Liu, Y. Guo, L. Lin, and J. Robertson, "First-principles calculations of the electronic structure and defects of Al_2O_3," *Journal of Applied Physics*, vol. 114, no. 2013, p. 083704, 2013.

[201] T. V. Perevalov, O. E. Tereshenko, V. A. Gritsenko, V. A. Pustovarov, A. P. Yelisseyev, C. Park, J. H. Han, and C. Lee, "Oxygen deficiency defects in amorphous Al_2O_3," *Journal of Applied Physics*, vol. 108, p. 013501, 2010.

[202] L. R. C. Fonseca, D. Liu, and J. Robertson, "p-type Fermi level pinning at a Si:Al_2O_3 model interface," *Applied Physics Letters*, vol. 93, no. 12, p. 122905, 2008.

[203] W. Kim, "Effect of Inserting Al_2O_3 Layer and Device Structure in HfO_2-Based ReRAM for Low Power Operation," in *2012 4th IEEE International Memory Workshop*, pp. 1–4, IEEE, 2012.

[204] K. Kamiya, M. Y. Yang, B. Magyari-Kope, M. Niwa, Y. Nishi, and K. Shiraishi, "Vacancy Cohesion-Isolation Phase Transition Upon Charge Injection and Removal in Binary Oxide-Based RRAM Filamentary-Type Switching," *IEEE Transactions on Electron Devices*, vol. 60, no. 10, pp. 3400–3406, 2013.

[205] X. Huang, H. Wu, Bin Gao, D. C. Sekar, L. Dai, M. Kellam, G. Bronner, N. Deng, and H. Qian, "HfO_2/Al_2O_3 multilayer for RRAM arrays: a technique to improve tail-bit retention," *Nanotechnology*, vol. 27, no. 39, p. 395201, 2016.

[206] M.-S. Lee, J.-W. Lee, C.-H. Kim, B.-G. Park, and J.-H. Lee, "Implementation of Short-Term Plasticity and Long-Term Potentiation in a Synapse Using Si-Based Type of Charge-Trap Memory," *IEEE Transactions on Electron Devices*, vol. 62, no. 2, pp. 569–573, 2015.

[207] W. Banerjee, Q. Liu, H. Lv, S. Long, and M. Liu, "Electronic imitation of behavioral and psychological synaptic activities using TiO_x /Al_2O_3 based memristor devices," *Nanoscale*, vol. 9, no. 38, pp. 14442–14450, 2017.